JPL Publication 92-32, Vol. I

An Improved Approach for Flight Readiness Certification— Probabilistic Models for Flaw Propagation and Turbine Blade Failure

Volume I: Methodology and Applications

N. R. Moore
D. H. Ebbeler
L. E. Newlin
S. Sutharshana
M. Creager

December 30, 1992

National Aeronautics and
Space Administration

Jet Propulsion Laboratory
California Institute of Technology
Pasadena, California

The research described in this publication was carried out by the Jet Propulsion Laboratory, California Institute of Technology, under a contract with the National Aeronautics and Space Administration.

Preface

This report presents a methodology for managing failure risk cost-effectively and evaluating flight readiness of such aerospace systems as launch vehicles and planetary spacecraft. The methodology was developed by the Jet Propulsion Laboratory (JPL) under NASA RTOP 553-02-01 sponsored by the Office of Space Flight (OSF), NASA Headquarters. This work was performed as a part of the Certification Process Assessment task initiated by OSF due to concern about criteria for certifying flight readiness of the Space Shuttle propulsion system. The methodology is not only applicable to flight readiness evaluation, but also to design definition and to the identification of risk control measures during the design, development, or operational phases of a project.

An early phase of this work included an extensive review of certification and failure risk assessment approaches used by the aerospace industry and government agencies. Based on the findings of this review,[1] further work was focused on defining, developing, and demonstrating an improved technical approach for failure risk assessment that can incorporate information from both test experience and analytical modeling to obtain a quantitative failure risk estimate. This approach, called Probabilistic Failure Assessment (PFA), is of particular value when information relevant to failure prediction, including test experience and knowledge of parameters used in analytical modeling of failure phenomena, is expensive or difficult to acquire. Under such constraints, a quantitative evaluation of failure risk based on the information available from both analytical modeling and operating experience is needed to make effective risk management decisions that utilize financial resources efficiently.

The PFA methodology is applicable to failure modes that can be characterized by analytical or empirical modeling of failure phenomena, including those of structural, electro-optical, propulsion, power, and thermal control systems, and is especially useful when models or information used in analysis are uncertain or approximate. PFA can be applied at any time in the design, development, or operational phases of a program to quantitatively estimate failure risk based on the information available at the time of the risk assessment and can be used to evaluate and rank alternative measures to control risk, thereby enabling the more effective allocation of limited financial resources.

---

[1] See [14] of Section 1.0 references.

The work documented in this report was carried out by a multidisciplinary team of JPL technical personnel, which was managed by N. R. Moore. This team was composed of individuals with expertise in statistics, systems modeling, and engineering analysis. D. H. Ebbeler formulated and structured the statistical methodology and directed its implementation. L. E. Newlin formulated and implemented probabilistic engineering models and implemented the statistical methodology. S. Sutharshana formulated and implemented probabilistic analytical methods and models. M. Creager[2] made major contributions to defining and formulating the probabilistic modeling approach and analytical modeling procedures used in this work. D. Goode typeset the manuscript, including graphics, using computerized desktop publishing methods, and E. Reinig edited the manuscript.

In developing the PFA methodology, the JPL team interacted with aerospace system manufacturers, the Marshall Space Flight Center, and the Lewis Research Center. Individuals of these organizations generously shared information and spent significant amounts of time with the JPL team. In particular, Rocketdyne, Canoga Park, California; Aerojet TechSystems, Nimbus, California; and Pratt & Whitney, West Palm Beach, Florida, collaborated in performing the application examples given herein. In addition, technical comments on certification approaches and failure modeling were provided by personnel from the above-listed organizations and General Electric, Cincinnati, Ohio; the Federal Aviation Administration; and the Wright-Patterson Air Force Base.

The PFA methodology, examples of its application to spaceflight components, and computer software used to implement PFA are documented in the two volumes of this report. Volume I documents the PFA methodology and the application examples, including the rationale for PFA and the analysis procedures used in the examples. Volume II contains detailed documentation of the computer software used to implement PFA for the application examples, including user's guides, code execution examples, flowcharts, and listings of the computer programs.

---

[2] Currently of Structural Integrity Engineering, Chatsworth, CA.

Acknowledgments

The authors wish to acknowledge the guidance and encouragement provided by D. L. Winterhalter of the Office of Space Flight, NASA Headquarters, whose support made this work possible. The authors appreciate the encouragement of R. Bardos, J. Mulcahy, and other individuals of OSF. The review and comments on this work provided by R. Weinstock of Vitro, Washington, D.C., contributed substantially to its successful completion.

The application examples of this report were performed in collaboration with Rocketdyne, Canoga Park, California; Aerojet TechSystems, Nimbus, California; and Pratt & Whitney, West Palm Beach, Florida. Several individuals at each organization contributed generously to this work, including E. P. Fox, C. G. Annis, and D. Paulus of Pratt & Whitney; K. J. O'Hara, D. O'Connor, K. J. Chang, and D. Russell of Rocketdyne; and B. Boehm of Aerojet. The authors worked particularly closely with E. P. Fox of Pratt & Whitney and K. J. O'Hara of Rocketdyne; their considerable contributions are gratefully acknowledged. The contributions of C. G. Annis, D. Russell, and K. J. Chang to the crack growth analysis are also gratefully acknowledged.

Present or former personnel of the NASA Marshall Space Flight Center, whose cooperation was instrumental in successfully performing this work, include J. Lombardo, J. S. Richards, G. W. Smith, L. D. Salter, H. P. Stinson, and J. Townsend.

Throughout the course of this work constructive guidance was provided by the Liquid Rocket Engine Certification Subcommittee of Aerospace Division Committee G-11, Society of Automotive Engineers. The membership of this subcommittee included: W. E. Campbell, Aerojet; K. J. O'Hara, Rocketdyne; E. P. Fox, Pratt & Whitney; J. S. Richards and H. P. Stinson, NASA-MSFC; R. L. Doebler, Aerospace Corp.; and N. R. Moore, JPL.

Finally, the authors wish to acknowledge the review of the technical approach of this work provided by the late R. P. Feynman of the California Institute of Technology.

The authors express their gratitude to all those individuals who contributed to this work and regret that a complete listing is not feasible.

Abstract

An improved methodology for quantitatively evaluating failure risk of spaceflight systems to assess flight readiness and identify risk control measures is presented. This methodology, called Probabilistic Failure Assessment (PFA), combines operating experience from tests and flights with analytical modeling of failure phenomena to estimate failure risk. The PFA methodology is of particular value when information on which to base an assessment of failure risk, including test experience and knowledge of parameters used in analytical modeling, is expensive or difficult to acquire.

The PFA methodology is a prescribed statistical structure in which analytical models that characterize failure phenomena are used conjointly with uncertainties about analysis parameters and/or modeling accuracy to estimate failure probability distributions for specific failure modes. These distributions can then be modified, by means of statistical procedures of the PFA methodology, to reflect any test or flight experience. State-of-the-art analytical models currently employed for design, failure prediction, or performance analysis are used in this methodology.

The PFA methodology can be applied at any time in the design, development, or operational phases of a program to quantitatively estimate failure risk based on the information available at the time failure risk is assessed. Sensitivity analyses conducted as a part of PFA can be used to evaluate and rank such alternative measures to control risk as design changes, testing, or inspections, thereby enabling limited program resources to be allocated more effectively.

PFA is generally applicable to failure modes that can be characterized by analytical or empirical models of failure phenomena and is especially valuable when models or information used in analysis are uncertain or approximate. Such failure modes include, but are not limited to, fatigue, flaw propagation, erosion, malfunctions of mechanical or electrical systems, and shortfalls with respect to performance or life goals for thermal control, electro-optical, power, or propulsion systems.

It is often not feasible to acquire enough test experience to establish high reliability at high confidence for spaceflight systems. Moreover, the results of conventionally performed analytical modeling of failure modes can be subject to serious misinterpretation when uncertain or approximate information is used to establish analysis parameters and calibrate the accuracy of analysis models. Under these conditions, a quantitative evaluation of failure risk based on the information

available from both test or flight experience and analytical modeling is needed to make effective risk management decisions.

This report discusses the rationale for the statistical approach taken in the PFA methodology, describes the PFA methodology, and presents examples of its application to structural failure modes. The engineering models and computer software used in fatigue crack growth and fatigue crack initiation applications are thoroughly documented.

Table of Contents

VOLUME I – Methodology and Applications

List of Figures

List of Tables

1.0 Introduction

Section 1.1

Information Available for Flight Readiness Assessment

Critical failures of such aerospace flight systems as launch vehicles or planetary spacecraft must be established as highly unlikely for the system to be considered flight worthy. At any time in the design, development, or operation of flight systems, the information sources for an assessment of flight readiness or failure risk during service are: (1) experience from tests and flights and (2) analytical modeling. It is rarely feasible to establish high reliability at high confidence by testing only for systems, major subsystems, and many components. Moreover, failure prediction by conventional, deterministic methods of analytical modeling can become arbitrary and subject to misinterpretation when information used to establish parameter values and to evaluate the accuracy of engineering models is uncertain or approximate, as discussed in [1] and [2].

For many failure modes of aerospace flight systems, direct experience is sparse and expensive or infeasible to acquire, and demonstrably conservative deterministic analyses results in unacceptable designs or service limits. Deterministic analysis is performed typically using conservative analysis methods along with conservative estimates of such parameters as loads and materials capability. When parameters or models are significantly uncertain, consistently conservative deterministic analysis often does not yield practicable designs or service limits, and the failure risk implied by less conservative deterministic analysis is not known. Under these conditions, an assessment of failure risk that quantitatively incorporates available information from both analytical modeling and test/flight experience enables more effective risk management decisions to be made. Risk management in the design, development, and operational phases of a project can be improved by using a risk assessment approach that can incorporate information quantitatively from both test/flight experience *and* analytical modeling.

In the failure risk assessment approach presented in this report, analytical modeling and test/flight experience are used in a statistical structure in which uncertainties about failure prediction are quantitatively treated. Using this approach, probabilistic analysis to characterize failure risk can be performed with the information available at any time in the design, development, qualification/certification, or operational phases of a project to obtain a quantitative measure of failure risk that is warranted by what is known about a failure mode. Failure modes that can be described by analytical models of the failure phenomena, even when such models

are uncertain or approximate, can be analyzed probabilistically using the approach presented here.

The value of test experience in establishing low failure probability with high confidence for flight configuration systems is limited when testing is halted before failures occur. Failures during testing are often avoided because they can result in the loss of costly hardware and damage to expensive test facilities. The availability of failure experience for flight hardware is further diminished because failure modes discovered during development testing are corrected by design changes which are intended to render their occurrence highly unlikely during subsequent mission operation. Consequently, test experience for aerospace systems typically does not include failure data for flight configuration systems, but instead consists of tests which are suspended before failures occur, i.e., "zero-failure" tests.

When the data from tests or flights consists of some number of trials with no failures, as is often the case for aerospace systems, the data is a weak information source for reliability demonstration or failure risk assessment. Demonstrating high reliability is equivalent to making statements about the left-hand tail of a failure distribution. Nonfailure test data typically provides very conservative bounding information about location and variability of the failure distribution. However, information about the failure distribution from analytical modeling can be extremely informative about the distribution's location. Using the approach presented here and in [1], the inclusion of analytical modeling allows an improved description of the failure distribution, even with the variability implied by uncertainty in analytical modeling due to sparse information. The exclusive use of zero-failure data to establish very low failure risk with high confidence requires an extremely extensive data set that is typically not feasible to acquire, as discussed in [1] and [5].

Failures can be categorized as the consequence of a specific event or as the result of accumulated damage. Erosion, fatigue cracking, degradation, and flaw propagation are examples of damage accumulation failure modes wherein failure is a result of the cumulation of aging effects produced by repeated exposure to operating conditions or by environmental parameters which vary cyclically. In contrast, event consequent failure modes are those in which failure is independent of the extent of previous exposure to operating conditions; instead, failure is a consequence of an event such as applied stress exceeding ultimate strength.

Failure prediction for event consequent failure modes is usually much less uncertain than for damage accumulation failure modes, in part because variability of event consequent failure distributions is often much smaller than that of damage accumulation failure distributions. It may be feasible to conduct testing programs to establish low failure probability with high confidence by testing only for event

consequent failure modes, while such testing is essentially infeasible for damage accumulation failure modes [5].

Probabilistic analyses can yield particularly useful results for a subset of the critical failure modes identified by means of Failure Modes and Effects Analysis (FMEA) or other screening procedures. The probabilistic approach to failure risk assessment presented in this report provides the capability to more effectively organize and interpret the information available to characterize the likelihood of failures during the service life of aerospace systems and to identify additional information that may be needed to control failure risk.

Section 1.2
Probabilistic Failure Risk Assessment

1.2.1 Risk Quantification Approach

Information from analytical modeling can be combined with information from test/flight experience to estimate failure risk quantitatively using a statistical framework based on Bayes' Rule, as shown in Figure 1.2-1. This approach should be applied individually to those failure modes identified for analysis. Analytical modeling is used to characterize conditions under which a specific failure mode may be expected to occur, e.g., excessive pressure difference or accumulated time in service, and it provides the information to establish the prior failure risk distribution of Figure 1.2-1. This prior distribution can be modified to reflect available success/failure data in a Bayesian statistical analysis, as discussed in [1], [3], and [6].

Analytical modeling to predict failure is based on available knowledge of the failure phenomenon and of such governing parameters as loads and material properties. Information about governing parameters can be derived from measurements taken during tests or flights, from analyses to characterize parameter values, from applicable experience with similar systems, or from laboratory tests. Measurements of physical parameters used in analytical modeling, e.g., temperatures and loads, can be a strong information source in failure risk assessment.

As shown in Figure 1.2-1, test/flight experience consists of physical parameter information and success/failure data. Information about physical parameters is incor-

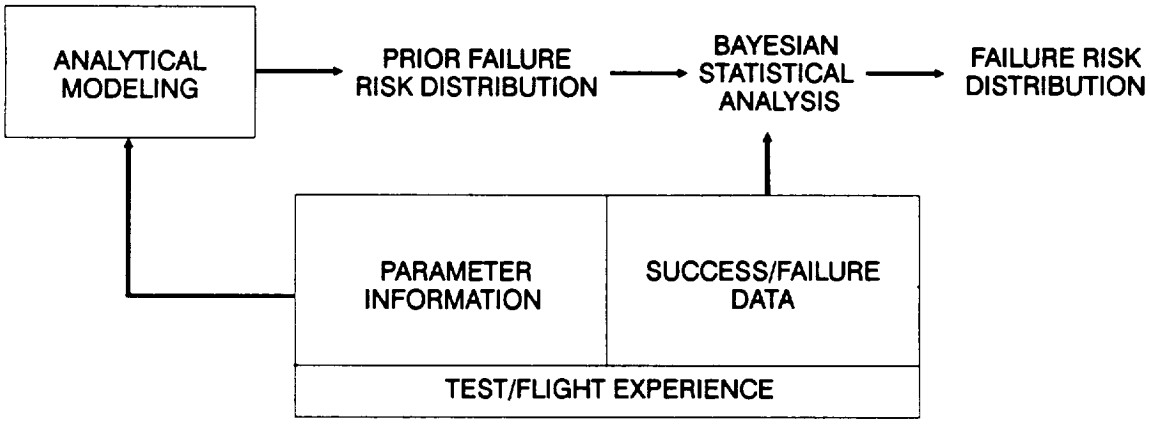

Figure 1.2-1 Information Sources for Failure Risk Assessment

porated into the analytical modeling and is reflected in the prior failure risk distribution. Success/failure data can be acquired from development testing, certification testing, or flight operation. The failure risk distribution resulting from the combination of the prior distribution and the success/failure data is the description of failure risk which is warranted by the information available. As additional information regarding governing physical parameters becomes available it can be incorporated into the analytical modeling to obtain a revised prior failure risk distribution. Additional information in the form of success/failure data can be processed by the Bayesian statistical algorithm to update the prior failure risk distribution using the procedure given in [1].

When the success/failure data for flight configuration hardware consists of some number of trials with no failures, as often occurs for damage accumulation failure modes, this data is usually a weak information source for failure risk assessment. In these cases, the failure risk distribution will be predominantly determined by the prior failure risk distribution of Figure 1.2-1.

1.2.2 The Probabilistic Failure Assessment Methodology

Figure 1.2-2 shows a stochastic structure for quantitatively estimating failure risk based on the available information about specific failure modes identified in a screening procedure such as a FMEA. This stochastic structure is an implementation of the statistical framework described above and is referred to as the Probabilistic Failure Assessment (PFA) methodology. The approach and structure of the PFA methodology are generally applicable to failure modes for which quantita-

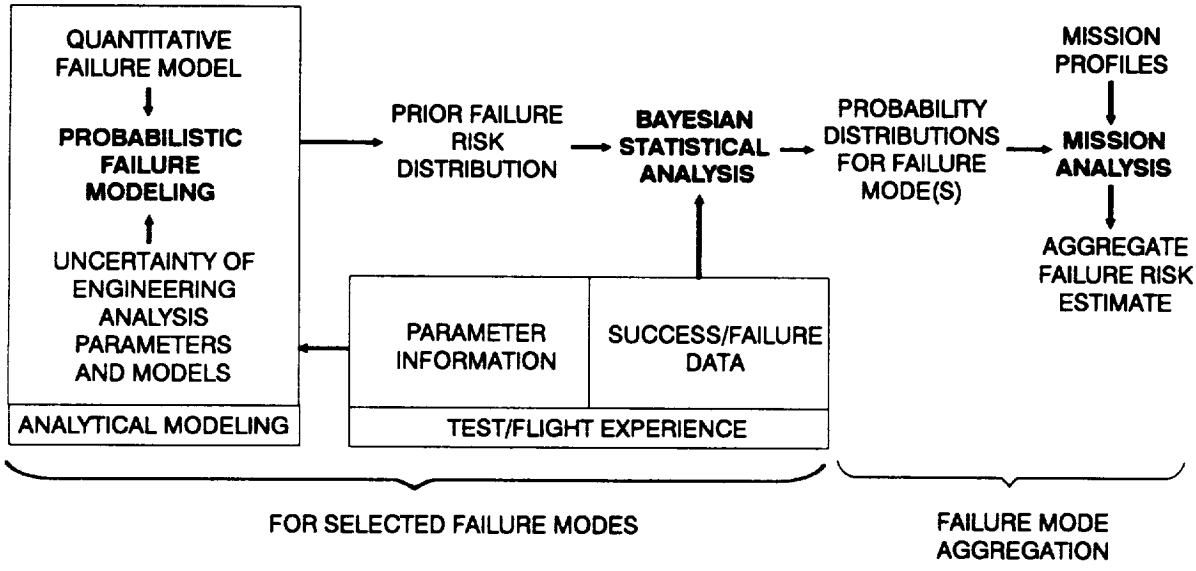

Figure 1.2-2 The Probabilistic Failure Assessment Methodology

tive analytical models can be employed to characterize a failure phenomenon and is particularly valuable when the analysis is uncertain or approximate.

The PFA methodology shown in Figure 1.2-2 consists of three major steps: probabilistic failure modeling, a Bayesian statistical analysis to consider success/failure data, and a mission analysis in which the failure probability distributions for a number of relevant failure modes can be aggregated. Probabilistic failure modeling and the Bayesian statistical analysis are performed for each failure mode identified for analysis. The features of the PFA methodology that are essential to evaluate failure risk meaningfully are: (1) inclusion of information from both analytical modeling *and* available operating experience; (2) analytical modeling of failure phenomena based on engineering analysis and/or physics; (3) representation of the uncertainty about analytical models and governing parameters, including uncertainty due to both intrinsic variation and sparseness or vagueness of information; and (4) consideration of failure risk over the service life.

State-of-the-art analysis models employed in design and in performance or life prediction are used in the PFA methodology. Within the PFA structure, uncertainties due to sparse information about values of analysis parameters and uncertainties about the accuracy of the analysis models are quantitatively treated. For example, in addition to the intrinsic variability of materials fatigue life, the uncertainty resulting from basing a model of fatigue life on limited information was treated in the stochastic materials fatigue life characterization model discussed in [1].

The probabilistic failure modeling element of the PFA methodology is shown in greater detail in Figure 1.2-3. Here, uncertainties in analysis parameters and models for the failure mode being analyzed are used in conjunction with the quantitative model of the failure phenomenon to predict failure probabilistically. Failure models are directly derived from deterministic analyses of failure modes which express failure parameters, such as burst pressure or fatigue life, as a function of governing parameters or *drivers*. For fatigue failure modes, the drivers include dimensions, loads, materials behavior, modeling accuracy, and environmental parameters such as local temperatures.

For many failure modes of concern, the failure model of Figure 1.2-3 is complex and involves the use of several analysis procedures, including finite element structural models. State-of-the-art models and procedures used by the aerospace community for design analysis and to predict performance or service life have evolved through extensive experience. These models and procedures often are comprised of a series of steps, each of which may be complex. The PFA methodology can accommodate generally accepted analysis models in current use. The accuracy of each model and procedure should be probabilistically characterized and treated as

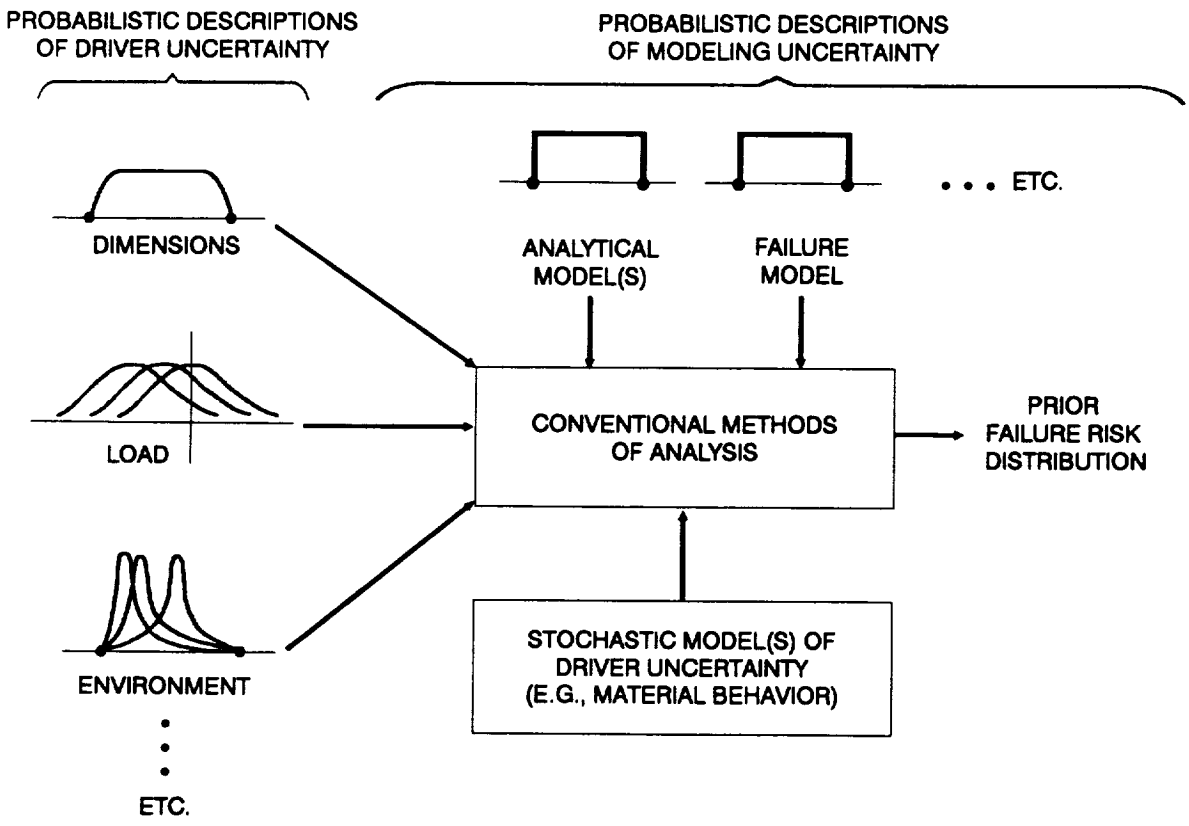

Figure 1.2-3 The Probabilistic Failure Modeling Procedure

a driver. Probabilistic descriptions of model accuracy are based on experience in using the models and, when available, on tests conducted specifically to evaluate model accuracy.

By calculating failure risk from an analysis based on the specification of failure models and drivers and which incorporates the associated uncertainties, the PFA methodology permits the quantitative assessment of failure risk even when failure data applicable to flight configuration hardware does not exist.

1.2.3 Driver Characterization

A driver for which uncertainty is to be considered must be characterized by a probability distribution over the range of values it can assume. That distribution expresses uncertainty regarding specific driver values within the range of possible values. A driver probability distribution must represent both intrinsic variability of the driver and uncertainty due to limited information on which to base the driver characterization.

Stochastic drivers are responsible for the probabilistic character of the PFA methodology. The need to represent a driver stochastically derives from two fundamental sources: intrinsic variability and specification error. Specification error can be due to engineering model accuracy and due to vague or sparse information about physical parameters.

For some stochastic drivers, it may not be possible to distinguish between intrinsic variation and variation due to specification error. In those cases, a stochastic driver is characterized by the compounded effect of both sources of variation without attempting to model each source separately. An example of this is the characterization of the stress concentration factor presented in [1] and [7]. Uncertainty in the stress concentration factor results from geometric variability induced by the manufacturing process and from an imperfect translation of geometric variability into stress concentration factor uncertainty.

Stochastic drivers are characterized by using the information that exists at the time of analysis. If driver information is sparse, the probabilistic characterization of such a driver must reflect that sparseness. If extensive experimental measurements have been performed for a driver, its nominal value and characterization of its variability can be inferred directly from empirical data. However, if little or no directly applicable empirical data is available, analysis to characterize a driver or experience with similar or related systems must be used.

The information on which driver uncertainty characterization is based can include measurements, related experience, and analysis conducted to bound or characterize the driver. All sources of driver uncertainty must be considered to appropriately represent risk due to limited information, and driver distributions must meet the criterion of not overstating the available information. Drivers are fundamental in the sense that they are observable parameters for which additional information regarding their values can be obtained if necessary. Such parameters include temperatures, loads, materials behavior, and statements about model accuracy. If uncertainty due to lack of information about a driver is found to make a significant contribution to failure risk, then the desirability of acquiring additional driver information should be evaluated.

Consider the example of a finite element analysis to characterize stresses. Material properties and loads are possible sources of intrinsic variation. The finite element model itself is a source of specification error in the computation of stresses since the model will not match the hardware precisely. In many cases, loads and material properties are sources of specification error, in addition to having intrinsic variability. There are cases where engineers know that a certain load varies

very little from flight to flight or part to part, but they may know the load magnitude only with a large uncertainty, say within a factor of two to four.

Some general guidelines for characterizing stochastic drivers have emerged from case studies conducted to date [1], [3], [7], [8], and [9]. Information about drivers is typically provided by engineers experienced in the characterization of a particular driver. All sources of uncertainty must be considered, and the information used must be traceable and documented. For drivers which have physical bounds, such as controlled dimensions or loads with physical upper limits, the Beta distribution parameterized with location, shape, and scale parameters has been successfully used [1]. If only bounds are known, a Uniform distribution is appropriate. For a driver such as turbopump speed whose variation can be thought of as due to the combined influence of a large number of small independent effects, the Normal distribution can be used. Also, past experience in characterizing a particular driver such as a material property may suggest the use of a particular distribution, for example, Weibull, Normal, or Lognormal.

The sparseness of the information typically available for characterizing a stochastic driver, the existence of significant specification error, and the manner in which driver uncertainty is often described have led to the use of a hyperparametric structure for driver distributions. For example, to characterize stress concentration factor uncertainty in a fatigue analysis application example given in [1], information from engineering analysis was used in establishing upper and lower bounds on the value for the stress concentration factor. In order to capture the fact that the most likely value of the stress concentration factor was not known with certainty, a Beta distribution with a Uniform distribution on the location parameter was used. This Uniform distribution is the hyperdistribution associated with the stress concentration factor uncertainty, and its parameters are the associated hyperparameters. This driver distribution is given in Figure 3-18 of [1].

1.2.4 Computational Methods

Monte Carlo simulation has been used as the principal computational method in the probabilistic failure modeling step of Figure 1.2-2. Monte Carlo simulation is a general method for probabilistic analysis that can be used with failure models of any complexity. Continually increasing computer power due to improving hardware and software is steadily expanding the practical application of such computationally intensive methods as Monte Carlo simulation. Efficient Monte Carlo techniques can be used to reduce the number of simulation trials for those problems where computational time would be an issue if direct Monte Carlo simulation were used.

Alternative computational methods, for example, FORM/SORM, [10] and [11], and MVFO/AMVFO, [12] and [13], may fail to give accurate results for problems in which significantly nonlinear models are employed and driver uncertainty is large. These computational methods can be used in probabilistic analyses which employ well-behaved failure models, particularly if the failure criterion is expressed explicitly in a closed form equation as opposed to a complex multistep algorithm. A comparison of FORM/SORM with direct Monte Carlo simulation for a flaw propagation example is given in [14].

Certain analysis methods sometimes employed in failure models, such as finite-element structural models, may appear to be too computationally intensive for practical use in a Monte Carlo simulation. However, they can be represented as response surfaces over the range of variation of significant parameters. Response surface methods are discussed in References 2, 3, 4, 5, 6, and 7 of Section 3. The uncertainties of analytical modeling procedures and of the response surface representation must be treated as drivers if significant. Computational methods are discussed further in [1] and [3].

Section 1.3
Implementing the PFA Methodology

Application of the PFA methodology to a subset of failure modes selected by FMEA or other screening procedures will identify those failure modes whose risk of occurrence is unacceptable. Options for corrective action that could be taken to control risk are shown in Figure 1.3-1. The PFA methodology produces a risk assessment that is commensurate with the available information. Unacceptable risk could be reduced by acquiring additional information to reduce the uncertainty of dominant drivers or by changing the design so that the available information is sufficient.

By conducting sensitivity analyses for selected failure modes with the PFA methodology, the sources of unacceptable failure risk can be identified in terms of the responsible drivers, and corrective action can be delineated. Design changes, improvements in manufacturing processes, additional characterization of loads and environments, validation of analytical models, improved characterization of materials behavior, and additional testing are among the options for corrective ac-

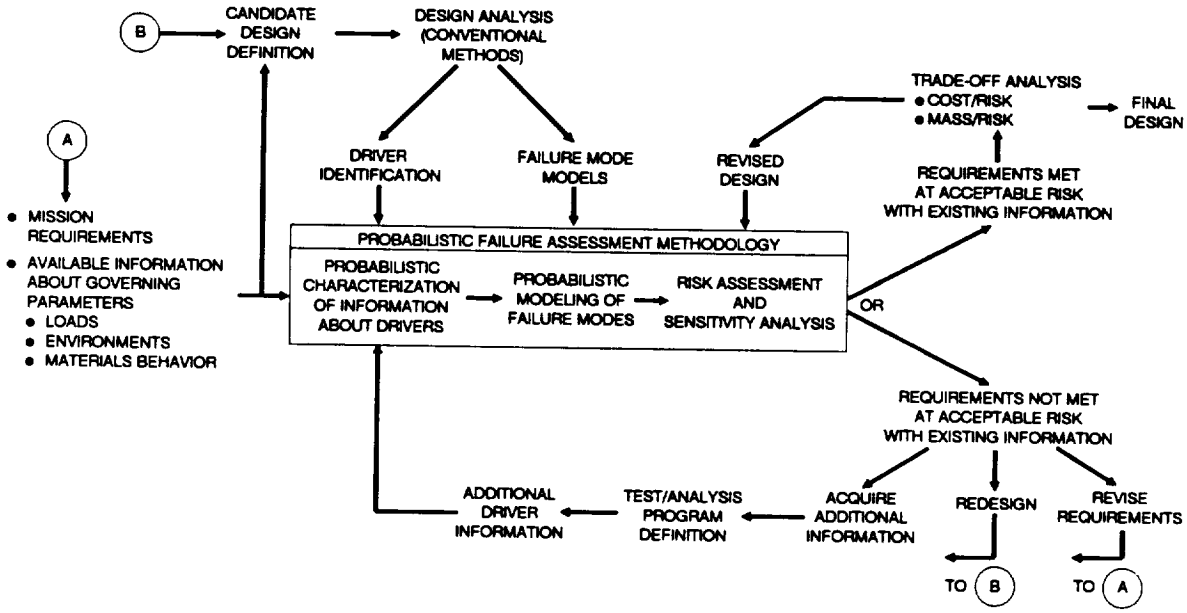

Figure 1.3-1 Integration of PFA into the Design and Development Process

tion that can be quantitatively evaluated by PFA sensitivity analyses. The PFA methodology can be employed to identify risk sources and corrective actions during the design, development, and operational phases of a program, thereby enabling limited financial resources to be allocated more effectively to control failure risk.

The failure models required for meaningful probabilistic analysis must be developed in concert with a valid interpretation of relevant experience. Adjudging failure probabilities, even with the most sophisticated methods, does not imply that the origins, mechanisms, and consequences of known failure modes are understood and have been properly treated nor that unexpected test observations and indications of unanticipated failure modes have been pursued until they are understood. An understanding of the causes and mechanisms by which failures occur is the foundation on which valid failure models must be based.

The PFA methodology can be employed in the design and development process to avoid the compounding of design conservatisms and margins that unnecessarily increase cost or weight when conventional design approaches are used. In addition, PFA enables the definition of test and analysis programs focussed on acquiring information about the most important cost, weight, or risk drivers. PFA is of particular value in the design and development of systems or components when uncertainties exist about important governing parameters or when design conservatism and redundancy used in the past must be reduced to meet more stringent cost or weight requirements.

The implementation of the PFA methodology in development programs would enable the consistent, risk-based definition of design parameters and of flight readiness evaluation criteria. PFA provides the capability to evaluate failure risk based on available information and to identify options to control unacceptable risk when relevant information is sparse and expensive or difficult to acquire. In particular, the PFA methodology provides a means for avoiding excessive conservatism in systems design and for more effectively allocating limited financial resources to control failure risk of lower weight and/or lower cost designs.

Section 1.4
Report Organization

This report consists of two volumes in which an improved methodology for assessing the risk of occurrence of specific failure modes of spaceflight systems is presented. Volume I presents examples of the application of the PFA methodology to crack growth, HCF, and LCF failure modes. Volume II consists of the documentation of the computer software for implementing the methodology in the application examples, including user's guides, code execution examples, and listings of computer programs.

This report and [1] together provide thorough and comprehensive documentation of the technical approach, methods and procedures of analysis, and computer software used in applying the PFA methodology to structural fatigue failure modes. This report presents applications of the PFA methodology to fatigue crack growth failure of a heat exchanger coil, fatigue crack growth failure of a diffusion bonded plate heat exchanger, low cycle fatigue failure of a turbine blade, and high cycle fatigue failure of a turbine blade.

The analysis methods used in crack growth modeling and crack growth application examples are presented in Section 2 of this report. In Sections 3 and 4, the LCF failure model and the HCF failure model for turbine blades are described and an application example for the LCF model is given. No application example for turbine blade HCF is presented, because collaborative work with Pratt and Whitney was halted due to ATD program funding constraints. The computer software used to implement the application examples is documented in Sections 5, 6, and 7 of Volume II.

The statistical methods used in applying the PFA methodology to fatigue failure modes, including the methods used to stochastically represent materials fatigue life are presented in Section 2.1 of [1]. The computer software used to implement these statistical methods is documented in Sections 4, 6, and 7 of [1].

An index of topics covered in this report is presented in Tables 1.4-1 and 1.4-2. The report sections wherein a particular topic is discussed are given in these Tables. Report sections which discuss the topics generically or with respect to an application example are listed separately. These Tables enable all the report sections in which a particular topic is discussed to be located readily.

Table 1.4-1 Index of Topics Contained in the Report

Topic	Generic	Application			
		Crack Growth		LCF	HCF
		Heat Exchanger Coil	External Heat Exchanger	Turbine Blade	Turbine Blade
Analysis Procedures	–	2.5 2.B	2.5	3.4	–
Application Examples	–	2.3	2.4	3.3	–
Bayesian Updating	1.2.1 1.2.2	–	–	–	–
Computational Methods	1.2.4	–	–	–	–
Crack Growth Calculations	2.2.4	2.2.4	2.2.4	–	–
Damage Modeling	–	–	–	3.2.5 3.2.6	4.2.4
Deterministic Analysis	1.1	2.2 2.B.3	2.2	3.2 3.4.2	4.2
Driver Distributions (Probability Distributions for Governing Parameters)	–	2.3.2 2.B.4	2.4.2	3.3.1 3.4.3	–
Driver Transformation (Stress/Strain Analysis)	–	2.2.2.1 2.3.3 2.D.1	2.2.2.2 2.4.3 2.D.2	3.2.4 3.3.3 3.4.2	4.2.3
Failure Mode Identification	1.1 1.2.2	2.3.1 2.B.2	2.4.1	3.2.1 3.4.1	4.2.1
Load Characterization Load History Synthesis Load Scale Factors	–	2.2.2 2.2.2.1 2.2.2.3 2.B.6	2.2.2 2.2.2.2	3.2 3.4.5	4.2
Material Fatigue Life Characterization	3.2.7	–	–	3.3.2 3.4.4	–
Multiple Failure Locations	–	–	–	3.2.8	4.2.5
Prior Distributions Probability of Failure Curve Prior Failure Risk Distribution	1.2.1 1.2.2	2.3.4 2.B.7 2.B.9	2.4.4	3.3.4 3.4.6 3.4.8	–
Probabilistic Approach	1.2.2 1.3	2.1 2.2.1	2.1 2.2.1	3.1 3.2.2	4.1 4.2.2
Reliability Demonstration by Testing	1.1 1.2.1 1.2.2	–	–	–	–
Sensitivity Analysis	1.3	2.3.4 2.B.8 6.1.4	2.4.4 6.1.4	3.3.4 3.4.7 6.2.4	–
Software Documentation Flowcharts	5.B	5.1	5.1	5.2	5.3

Table 1.4-1 Index of Topics Contained in the Report (Cont'd)

Topic	Generic	Application			
		Crack Growth		LCF	HCF
		Heat Exchanger Coil	External Heat Exchanger	Turbine Blade	Turbine Blade
Software Documentation Program Listing/Structure	–	7.1	7.1	7.2	7.3
Software Documentation User's Guide	–	6.1	6.1	6.2	–
Stochastic Crack Growth Model	2.2.3 2.5.2	2.2.3 2.3.1.1 2.B.5	2.2.3 2.4.1.1	–	–

Table 1.4-2 Index of Software Documentation Contained in the Report

TOPIC	METHODOLOGY	SOFTWARE DOCUMENTATION		
		FLOWCHARTS	USER'S GUIDE	STRUCTURE /LISTING
External Heat Exchanger	2.2 2.4	5.1	6.1	7.1
Heat Exchanger Coil	2.2 2.3	5.1	6.1	7.1
Turbine Blade HCF	4.2	5.3	–	7.3
Turbine Blade LCF	3.2	5.2	6.2	7.2

References

[1] Moore, N., et al., An Improved Approach for Flight Readiness Certification – Methodology for Failure Risk Assessment and Application Examples, JPL Publication 92-15, Jet Propulsion Laboratory, California Institute of Technology, Pasadena, California, June 1, 1992.

[2] Feynman, R. P., "Personal Observations on Reliability of Shuttle," Report of the Presidential Commission on the Space Shuttle Challenger Accident, Appendix F, 1986.

[3] Moore, N., Ebbeler, D., and Creager, M., "A Methodology for Probabilistic Prediction of Structural Failures of Launch Vehicle Propulsion Systems," Proceedings of the AIAA/ASME/ASCE/AHS/ASC 31st Annual Structures, Structural Dynamics, and Materials Conference, April, 1990, part 2, pp. 1092-1104.

[4] Moore, N., Ebbeler, D., and Creager, M., "Probabilistic Service Life Assessment," Reliability Technology – 1992, AD-Vol. 28, American Society of Mechanical Engineers, November, 1992, ISBN 0-7918-1095-X.

[5] Moore, N., Ebbeler, D., and Creager, M., "Failure Risk Assessment By Analysis and Testing," AIAA Paper 92-3415, AIAA/SAE/ASME/ASEE 28th Joint Propulsion Conference, July, 1992.

[6] Martz, H. F., and Waller, R. A., Bayesian Reliability Analysis, John Wiley & Sons, New York, N.Y., 1982.

[7] Sutharshana, S., et al., "Probabilistic High Cycle Fatigue Failure Analysis Applicable to Liquid Propellant Rocket Engines," Proceedings of the AIAA/ASME/ASCE /AHS/ASC 31st Annual Structures, Structural Dynamics, and Materials Conference, April, 1990, part 2, pp. 1105-1114.

[8] Newlin, L., et al., "Probabilistic Low Cycle Fatigue Failure Analysis Applicable to Liquid Propellant Rocket Engines," Proceedings of the AIAA/ASME/ASCE/AHS/ASC 31st Annual Structures, Structural Dynamics, and Materials Conference, April, 1990, part 2, pp. 1115-1123.

[9] Sutharshana, S., et al., "A Probabilistic Fracture Mechanics Approach for Structural Reliability Assessment of Space Flight Systems," Advances in Fatigue Lifetime Predictive Techniques, Special Technical Publication 1122, American Society for Testing and Materials, 1991.

[10] Madsen, H. O., Krenk, S., and Lind, N. C., Methods of Structural Safety, Prentice-Hall, Englewood Cliffs, New Jersey, 1986.

[11] Der Kiureghian, A., and Liu, P.-L., "First and Second-Order Finite Element Reliability Methods," to appear in Computational Mechanics of Probabilistic and Reliability Analysis edited by W.-K. Liu and T. Belytschko.

[12] Wirsching, P. H., et al., "An Overview of Reliability Methods in Mechanical and Structural Systems," 28th Annual Structures, Structural Dynamics and Materials Conference, April, 1987.

[13] Wu, Y. T., "Demonstration of a New, Fast, Probability Integration for Reliability Analysis," Journal of Engineering for Industry, Transactions of the ASME, Vol. 109, February, 1987, pp. 24-28.

[14] Moore, N., et al., A Review of Certification Practices Potentially Applicable to Man-Rated Reusable Rocket Engines – Certification Process Assessment Task, JPL D-7969, Jet Propulsion Laboratory, California Institute of Technology, Pasadena, California, February, 1986 (internal document).

Appendix 1.A
List of Acronyms

ATD-HPFTP	Alternate Turbopump Development Program – High Pressure Fuel Turbopump
ATD-HPOTP	Alternate Turbopump Development Program – High Pressure Oxidizer Turbopump
CT	Compact Tension
EXHEX	External Heat Exchanger
FAA	Federal Aviation Administration
FE	Finite Element
FMEA	Failure Modes and Effects Analysis
FORM/SORM	First Order Reliability Method/Second Order Reliability Method
FR	Frequency Response
HCF	High Cycle Fatigue
HEX	Heat Exchanger
HPOTP	High Pressure Oxidizer Turbopump
JPL	Jet Propulsion Laboratory
JSC	Johnson Space Center
LCF	Low Cycle Fatigue
MC	Monte Carlo
MSFC	Marshall Space Flight Center
MVFO/AMVFO	Mean Value First Order/Advanced Mean Value First Order
NASA	National Aeronautics and Space Administration
PFA	Probabilistic Failure Assessment
PFM	Probabilistic Failure Model
PSD	Power Spectral Density
RMS	Root Mean Square
RV	Random Vibration
SIF	Stress Intensity Factor
S/N	Stress/Life or Strain/Life
SSME	Space Shuttle Main Engine
TMF	Thermal-Mechanical Fatigue
USAF	United States Air Force

2.0 Probabilistic Crack Growth Modeling

Section 2.1
Introduction

The crack growth failure model presented in this report probabilistically computes the life of a cracked structure subjected to cyclic loading. For certain structural components of spaceflight systems, loads due to vibration, temperature gradients, aerodynamic effects, and pressure difference combine to cause crack growth which can result in structural failure. Typically, crack growth at a single critical location will determine the life of a component.

The approach to modeling crack growth failure taken in this work is illustrated in Section 2.2. In this approach, Monte Carlo (MC) simulation is employed to establish a distribution of failure lives, as described in Section 2.2.1. A major element in this approach is the transformation of loads and other parameters, such as geometry and material properties, to synthesize a principal stress history. The details of load characterization and stress analysis are given in Section 2.2.2. A description of the stochastic crack growth model is found in Section 2.2.3, which is followed by a description of the crack growth calculations. A schematic diagram of the crack growth modeling approach is given in Figure 2.1-1.

The probabilistic crack growth model presented in this report is generic in nature, and it was used in crack growth analyses of two Space Shuttle Main Engine (SSME) components – the HPOTP Heat Exchanger (HEX) Coil and the proposed

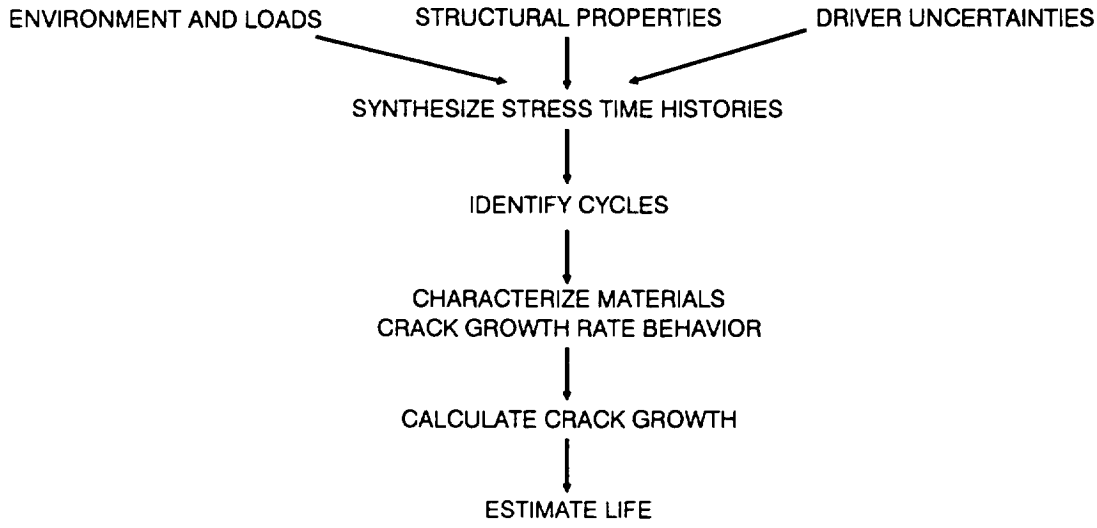

Figure 2.1-1 Crack Growth Failure Modeling Approach

External Heat Exchanger (EXHEX). Descriptions of these two applications of the probabilistic crack growth model are given in Sections 2.3 and 2.4, respectively. In each of these sections, a description of the component and the crack growth data is given. This is followed by the rationale for probabilistic characterization of crack growth model parameters, i.e., the drivers; and finally, analysis procedures and results are presented.

The procedure for conducting an analysis with the probabilistic crack growth model is described in Section 2.5. The results for the intermediate steps of the probabilistic crack growth analysis of the HEX coil are given in Appendix 2.B.

Section 2.2
Crack Growth Methodology

2.2.1 Simulation Structure

The Monte Carlo simulation structure used in this work allows the use of a comprehensive crack growth model and places no restrictions on the formulation of the model nor on the types of probability distributions that may be employed to describe the significant parameters. The MC simulation procedure is easy to understand and implement, especially when a deterministic crack growth algorithm is already in place [1]. Other computational methods have been proposed, in which the fatigue crack growth failure is formulated in terms of limit states and the probability of failure is estimated by first-order and second-order reliability methods called FORM and SORM [2]. For the FORM and SORM computational algorithms it is desirable to have the limit state in closed form so that the gradients on the limit state surface can be calculated analytically. This places restrictions on the type of crack growth rate models and on all other parameters that one may desire to characterize stochastically. A more detailed description of MC simulation is given in [1], and an evaluation of the alternative computational methods is given in [3]. A comparison of the MC simulation and FORM/SORM computational methods in terms of accuracy and efficiency for the HEX coil is given in [4].

The structure of the MC simulation for crack growth failure analysis is given in Figure 2.2-1 (descriptions of the symbols in the figure are given in Appendix 2.A). The number of simulation trials N is user specified. The required simulation size is a function of the failure probability at which a life estimate is desired and the precision required. For the crack growth applications, simulations of 10,000 trials were used for characterizing reliability and simulations of 1000 trials were used for marginal analyses to assess the importance of individual input parameters. The simulation generates a set of failure lives. In order to assess failure probability, the left-hand tail of the simulated distribution of failures is represented in an analytical form which allows for the use of Bayesian updating in order to combine simulation results with operating experience, as described in [1].

A deterministic crack growth failure model is embedded within the simulation structure, as shown in Figure 2.2-1. The failure model expresses the crack growth life as a function of drivers which may be either deterministic or stochastic. The drivers consist of geometry, loads, environmental parameters, material properties, and parameters which account for uncertainties in these driver specifications. Uncertainty about the analysis is formally included by means of model accuracy factors, which are also treated as drivers. Uncertainty in a driver is characterized by a

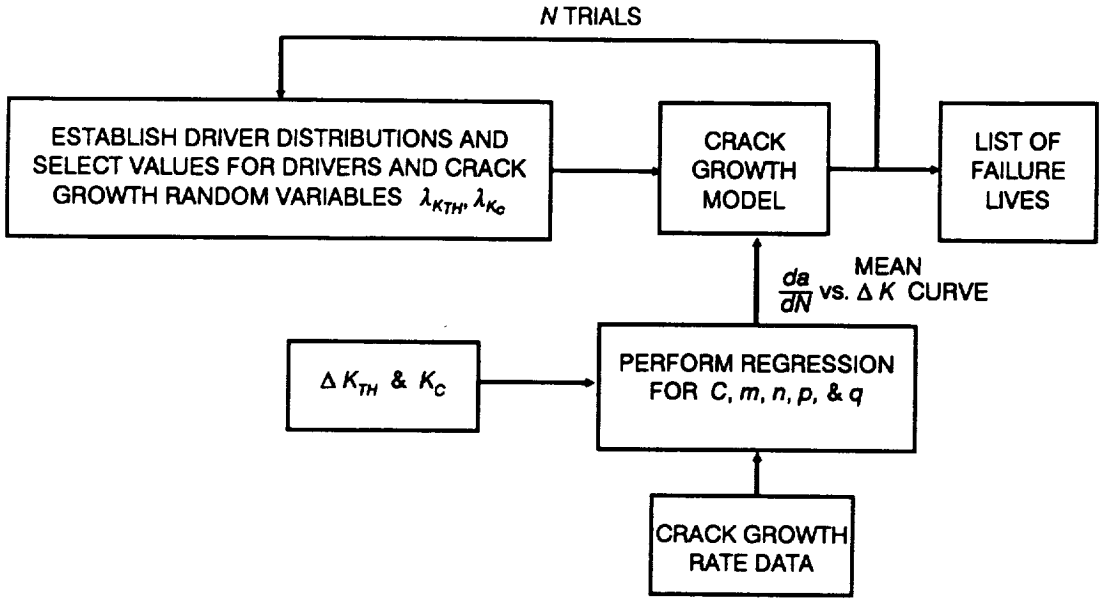

Figure 2.2-1 Crack Growth Failure Simulation Structure

probability distribution over the range of values the driver can assume. The driver distributions are specified to account for both intrinsic variability and uncertain knowledge or limited information, as discussed in Section 1.2.4 of [1]. For the crack growth applications, Uniform, Normal, and Beta distributions were used to characterize the drivers.

2.2.2 Load Characterization and Stress Analysis

In the applications presented here, vibration loads are primarily responsible for crack growth which can result in structural failure. Rocketdyne has characterized the vibration environment of the SSME by power spectral density (PSD) envelopes for different vibration zones, as discussed in Section 2.2.1.2 of [1]. In the procedures employed by Rocketdyne and NASA/MSFC, data for characterizing the SSME vibration environment are obtained from engine hot fire tests. The acceleration PSDs are processed to derive design envelopes which are a part of the current R5 vibration load criteria [5]. A detailed description of the loads analysis is given in Section 2.2.1.2 of [1].

The static and dynamic analyses to determine forces at various locations in the structure, as performed by Rocketdyne using FE models, are described in Section 2.2.1.2 of [1]. Modal dynamic analysis procedures were used to perform random vibration (RV) and frequency response (FR) analyses. The first step prior to modal analyses requires the extraction of the eigenvalues of the system. The FE results

at the location of interest were used by JPL in the probabilistic crack growth analysis.

In the procedure used by JPL, the design envelope loads (i.e., Rocketdyne's design values which are conservative) were adjusted to estimate nominal loads. Scale factors used to adjust the load distribution were based on such information as coefficients of variation and coverage factors of the raw PSD sample population. If strain gage measurements were available, the mean of the scale factor was further adjusted to reflect the acquisition of this additional information. A detailed discussion on the load factors is given in Section 2.1.3.2 of [1].

2.2.2.1 Stress Analyses for the HEX Coil

The commercial software package STARDYNE [6] was used by Rocketdyne to analyze the HEX Coil, shown in Figure 2.3-2, represented by line finite elements (e.g., beams, pipes). This approach provides accurate estimates of beam-end forces, which were extracted at a node close to the location of interest. The beam bending and cylindrical pressure vessel equations were employed to derive the stresses. The beam force-to-stress mapping is described in Section 2.2.1.3 of [1]. These beam-end forces were used as input to the probabilistic crack growth duct analysis programs developed by JPL.

In the JPL probabilistic crack growth program, stresses at the location of interest in a duct are calculated using the beam-end forces derived from the FE analyses, thermal gradient, and internal and external pressures. Figure 2.2-2 describes the geometry and the nomenclature for a duct. The stress equations for an elbow duct, based on the ASME pressure vessel code [7], were used in the JPL program and are given in Section 2.2.1.3 of [1]. The equations given below are a special case of the elbow duct equations for a straight pipe. Only the expression for the longitudinal stress is given below, since its magnitude for the HEX coil application is much larger than the other stress components. This allows the maximum principal stress in the duct, which governs crack growth, to be assumed equal to the longitudinal stress. The longitudinal (axial) stress in the duct is:

$$\sigma_x = K_{OFF}\left\{\frac{P}{A} + \cos\phi\,\frac{M_y R}{I} + \sin\phi\,\frac{M_z R}{I} + \left(p_i - p_o\right)\frac{R_i^2}{R_o^2 - R_i^2}\right\} + \sigma_{TH} \qquad (2\text{-}1)$$

in which the thermal stresses at the inside and outside wall are:

$$\sigma_{TH} = \frac{\Delta T\,\alpha\,E}{2\,(1-\nu)\ln\frac{R_o}{R_i}}\left(1 - \frac{\frac{2R_i^2R_o^2}{R^2}}{\left(R_o^2 - R_i^2\right)}\ln\frac{R_o}{R_i}\right) \qquad (2\text{-}2)$$

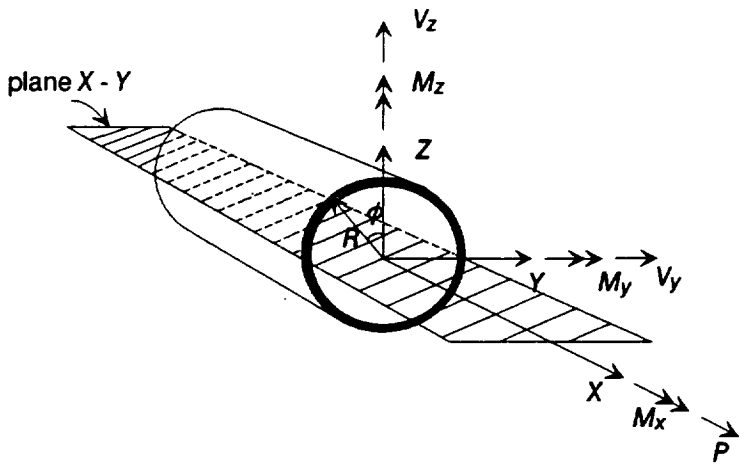

Figure 2.2-2 Geometry of Duct

A positive ΔT will result in tension in the outer wall and compression in the inner wall.

The notation for the above equations is as follows:

p_i, p_o	= internal, external pressures
R	= radius where the stress is to be found
R_i, R_o	= internal, external radii
P	= axial force along axis x
M_y, M_z	= moments about axes y and z
K_{OFF}	= stress concentration factor due to weld offset
ΔT	= temperature difference across wall $T_{in} - T_{out}$
E	= Young's modulus
α	= thermal coefficient of expansion
ν	= Poisson's ratio
ϕ	= angle between z-axis and critical location on the circumference
A	= cross-sectional area
I	= cross-sectional moment of inertia

The factor K_{OFF} is the stress concentration due to weld offset. The relation used to estimate the stress concentration factor is given in Section 2.2.1.3 of [1] as

$$K_{OFF} = \lambda_{OFF} \left[1 + 3F_k W_{OFF}\right] \tag{2-3}$$

in which λ_{OFF} is the weld offset accuracy factor and F_k is a stress reduction factor which is based on the radius to wall thickness ratio R/t. A piecewise linear F_k vs. R/t curve was used to obtain F_k for a given value of R/t. This F_k vs. R/t curve is given in Section 3.A.2.3 of [1].

2.2.2.2 Stress Analyses for the EXHEX

The stress analyses for the EXHEX, shown in Figure 2.4-2, were performed by Aerojet using the commercial software package ANSYS [8]. A two-dimensional plane strain FE model was used for static stress analysis and a three-dimensional FE model with iso-parametric brick elements was used for the dynamic analysis. To enable the assignment of support accelerations, the eigenvalue analysis which preceded the modal random vibration and frequency response analysis was performed with a large mass assigned to the bracket attachment nodes. The material properties for the solid or "land" areas and porous or "channel" areas in the core were assigned in the FE model via a "solidity factor" [9].

2.2.2.3 Stress Summation

The stresses due to static and dynamic load sources are combined to derive the history $\sigma(t)$ for the axial stress component σ_x for the HEX coil and the vertical stress component σ_z for the EXHEX as follows

$$\sigma(t) = \lambda_{ST}\,\lambda_{ST_{str}}\,\sigma_{ST} + \sum_{i=1}^{NLOAD} \lambda_{Di}\,\lambda_{DYN_{str}}\,\sigma_{Di}(t) \tag{2-4}$$

in which

λ_{ST}	= accuracy factor on the static load source
$\lambda_{ST_{str}}$	= static stress analysis accuracy factor
σ_{ST}	= stress due to static loads
λ_{Di}	= accuracy factor on the *i*th dynamic load source
$\lambda_{DYN_{str}}$	= dynamic stress analysis accuracy factor
$\sigma_{Di}(t)$	= time history for stress due to *i*th dynamic load source
NLOAD	= total number of dynamic load sources

The static stresses for the HEX coil and EXHEX are due to pressures and temperatures. The HEX coil has secondary static loads from misalignment, gimbal displacement, fluid momentum, and acceleration loads. Those static loads and the non-vibration component of the aerodynamic loads are specified as concentrated

nodal forces P, M_y, M_z, etc., for the stress calculation. The primary dynamic load sources for both components are due to random vibration and superimposed sinusoidal forces. The HEX coil also has a vibrating component of the aerodynamic load.

An efficient form of the calculation given by Equation 2-4 was implemented for summing the stresses from dynamic loads. First, reference time histories were derived for each dynamic load source. The reference histories due to a random load were generated for a standard deviation of unity. The sinusoidal reference time histories were generated with an amplitude of unity. The reference histories were generated in a separate computer program [1] and used as input for the probabilistic crack growth program. The non-time varying stress amplitudes $\overline{\sigma_{Di}}$ were used to scale the reference histories. For the HEX coil the $\overline{\sigma_{Di}}$ are the longitudinal stresses derived from Equation 2-1 using the root mean square (RMS) values and maximum amplitudes of the beam-end forces obtained from the RV and FR analyses, respectively. For the EXHEX the $\overline{\sigma_{Di}}$ are the RMS values and amplitudes of the σ_z stresses obtained from the RV and FR analyses. The implementation of Equation 2-4 may be written as

$$\sigma_{(t)} = \lambda_{ST}\,\lambda_{ST_{str}}\,\sigma_{ST} + \sum_{i=1}^{NLOAD} \lambda_{Di}\,\lambda_{DYN_{str}}\,\overline{\sigma_{Di}}\;\sigma_i(t) \tag{2-5}$$

in which $\sigma_i(t)$ is the reference time history for the ith dynamic load source.

For the HEX coil, Rocketdyne performed separate RV and FR analyses by applying the excitation along each global direction x, y, and z. Thus, the total stress response is the summation from responses in each direction. The dynamic stresses in Equation 2-5 for the three directions are given by

$$\overline{\sigma_{Di}}\;\sigma_i(t) = \overline{\sigma_{Dix}}\;\sigma_{ix}(t) + \overline{\sigma_{Diy}}\;\sigma_{iy}(t) + \overline{\sigma_{Diz}}\;\sigma_{iz}(t) \tag{2-6}$$

The reference time histories for the different load sources in a given direction were generated by assuming that they were fully correlated. However, across the three directions x, y, and z, the histories were assumed to be uncorrelated.

For the EXHEX only the response along global direction z was considered. Thus, an additional step for summing the stresses from the three input directions was not needed.

2.2.3 Stochastic Crack Growth Model

The generalized Forman model [10] was chosen as the basis for the stochastic crack growth rate model. The Forman equation is

$$\frac{da}{dN} = \frac{C(1-R)^m \ \Delta K^n \ [\ \Delta K - \Delta K_{TH}\ ]^p}{[\ (1-R)K_c - \Delta K\ ]^q} \qquad (2\text{-}7)$$

in which da/dN is the crack growth rate, ΔK is the stress intensity factor range, ΔK_{TH} is the threshold stress intensity factor range, K_c is the critical stress intensity factor, R is the stress ratio, and C, n, m, p, and q are the model parameters. The generalized Forman equation was chosen as the starting point because it captures the crack growth behavior in all of the growth rate regimes and, as will be shown below, it can be directly extended to a stochastic crack growth rate model.

Unlike crack initiation data, fatigue crack growth rate data above 10^{-7} in./cycle and below 10^{-3} in./cycle do not exhibit a large amount of life variation. This can be seen by examining the extensive data sets of [11] and [12] in which, for the same initial crack size, the ratio between the shortest and longest life is typically much less than two. This variation in the mid-rate region is small compared to the life variation that may occur due to uncertainty in other material properties such as ΔK_{TH}, stresses, initial crack geometry, etc. Many empirical da/dN vs. ΔK plots found in the literature seem to suggest that crack growth rate data scatter is large but this is an artifact of data gathering and data reduction. However, this localized growth rate scatter is not significant, as may be seen by comparing the low variability in lives to the much higher scatter in growth rates derived for the same data in [11] and [12]. The generalized Forman model can be easily employed to model variability of crack growth rate in the mid-rate region by stochastically varying C in Equation 2-7, although for the reasons outlined above it was deemed unnecessary.

In contrast to the crack growth in the mid-rate region, the uncertainties in the high- and low-growth rate regions can be significant. This uncertainty is due to both intrinsic growth rate variability and lack of information in these regions, and it may be represented as uncertainty of the stress intensity range values which are asymptotes to the crack growth rate curve at its upper and lower ends. The uncertainty in the asymptotes is readily captured by using two stochastic scale parameters $\lambda_{K_{TH}}$ and λ_{K_c}. The first one modifies the nominal value of the lower asymptote ΔK_{TH} and the second parameter shifts the upper asymptote $(1 - R)\ K_c$. Thus, the stochastic crack growth rate equation is given by

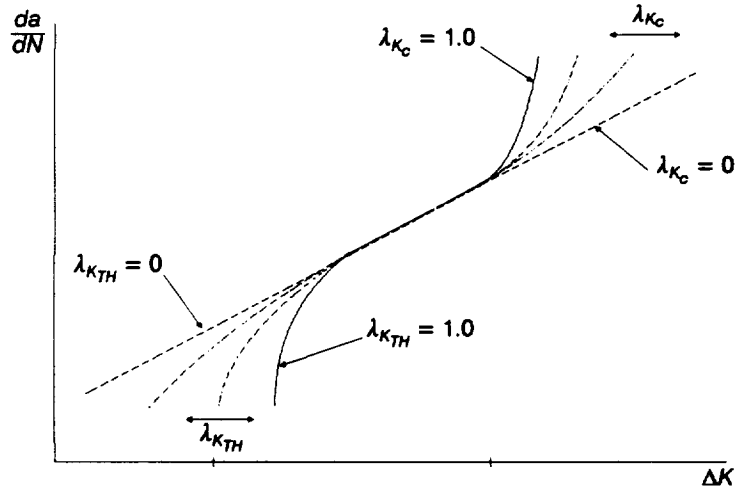

Figure 2.2-3 Description of the Stochastic Crack Growth Equation in Log–Log Space

$$\frac{da}{dN} = \frac{C(1-R)^m \Delta K^n [\Delta K - \lambda_{K_{TH}} \Delta K_{TH}]^p}{[(1-R)\lambda_{K_c} K_c - \Delta K]^q} \quad (2\text{-}8)$$

The uncertainty in $\lambda_{K_{TH}}$ and λ_{K_c} may be characterized by probability distributions, or they may be treated parametrically as was done in the analyses of the HEX coil and EXHEX. Figure 2.2-3 shows the effect of perturbing $\lambda_{K_{TH}}$ and λ_{K_c} in the growth rate Equation 2-8. If there is uncertainty due to sparseness of data, or if the material test conditions do not closely represent the component operating environment, some of the other equation parameters may also be modeled stochastically. For the EXHEX, crack growth rate data was only available for a single stress ratio R, and it was not possible to estimate the parameter m which drives the stress-ratio effects in the mid-rate region using a least squares fit of Equation 2-7. In this case, the uncertainty in m was captured by describing m stochastically, based on values observed for similar materials.

As shown in Figure 2.2-1, the mean crack growth rate equation, which is an input to the crack growth model, is typically determined by performing a regression on crack growth data. The parameters C, m, n, p, and q are estimated by a least squares fit of the growth rate Equation 2-7, as follows:

$$\ln\left[\left(\frac{da}{dN}\right)_i\right] = \ln C + m\ln(1-R) + n\ln\Delta K_i + p\ln[\Delta K_i - \Delta K_{TH}] - q\ln[(1-R)K_c - \Delta K_i] \quad (2\text{-}9)$$

in which K_c and ΔK_{TH} are specified exogenously. The information available to establish K_c and ΔK_{TH} is application dependent. For the HEX coil, where threshold crack growth rate data were available at several values of R, the following threshold model [10] was used.

$$\Delta K_{TH} \geq (1-C_o R)^d \Delta K_{THo} \quad (2\text{-}10)$$

where the inequality is a consequence of requiring that ΔK_{TH} be a "threshold" in the sense that all ΔK data points used to determine the threshold must be greater than the estimated threshold. The parameters d and C_o can be estimated by a non-linear least squares fit of the threshold model, as follows:

$$\ln\Delta K_{TH} = d\ln(1-C_o R) + \ln\Delta K_{THo} \quad (2\text{-}11)$$

The value of ΔK_{THo} is estimated by $\min_R \left[\frac{\Delta K_{TH}}{(1-C_o R)^d}\right]$ to satisfy the inequality.

A similar model could be used to characterize K_c. However, for the HEX coil and EXHEX, K_c was modeled as a fixed parameter since the ΔK values for these applications were in the threshold region and life was not sensitive to the value of K_c.

2.2.4 Crack Growth Calculations

The software developed for performing crack growth analysis synthesizes a stress history due to dynamic load sources and uses a linear elastic fracture mechanics formulation. The stress cycles were obtained by performing a cycle count on the composite stress time history. The rainflow cycle counting method described in Section 2.2.1.4 of [1] was used. The information from the cycle counting was assigned to a stress level vs. number of cycles table. One hundred stress level ranges were used for the table.

The load interaction in growth calculations was accounted for using the generalized Willenborg [13] retardation model. In this model the minimum and maximum stress intensity factors (SIF) are reduced based on the sizes of the plastic zones due to an overload and the current load. That is,

$$K_{max.eff} = K_{max} - K_{red} \tag{2-12}$$

$$K_{min.eff} = K_{min} - K_{red}$$

in which the SIF reduction is

$$K_{red} = \frac{K_{max.req} - K_{max}}{RSO - 1} \tag{2-13}$$

RSO is a parameter of the generalized Willenborg model and $K_{max.req}$ is the SIF required to extend the current plastic zone boundary to the overload boundary and it is given by

$$K_{max.req} = \sigma_y \left[\frac{a_o + r_{po} - a_i}{\gamma}\right]^{1/2} \tag{2-14}$$

in which σ_y is the yield stress, a_o and r_{po} are the crack length and plastic zone size at overload cycle, respectively, and a_i is crack length at the current cycle. γ is a geometry factor that is $\frac{1}{6\pi}$ for plane strain and $\frac{1}{2\pi}$ for plane stress. The plastic zone size is given by

$$r_p = \frac{\gamma K_{max}^2}{\sigma_y} \tag{2-15}$$

In the calculation of the effective *K* values, if $K_{min.eff} \leq 0$ then $K_{min.eff} = 0$. The effective SIF range and stress ratio due to retardation that is used for growth calculation are given by

$$\Delta K_{eff} = K_{max.eff} - K_{min.eff} \tag{2-16}$$

$$R_{eff} = \frac{K_{min.eff}}{K_{max.eff}}$$

A single typical value of $RSO = 2.3$ was used since crack growth retardation effects were not significant for the HEX coil and EXHEX. If retardation is significant the empirical parameter *RSO* may be characterized stochastically to model the uncertainty.

Since the traditional cycle-by-cycle crack growth life calculation is computationally intensive, an extremely fast yet accurate block-by-block approach first intro-

duced by Brussat [14] is used here. A block is a repeatable segment of the applied loads. For the HEX coil and the EXHEX, the loading blocks were the aggregated reference time histories of one-second duration. A duration of one second was sufficient to represent the probabilistic characteristics of the applied loads. In the block approach, a block growth rate, da/dB, is calculated at distinct crack lengths, starting from the initial crack length a_i to the final length a_f, by summing the crack growth rates, da/dN, from Equation 2-8 that correspond to ΔK_{eff} and R_{eff} for each stress level in the load block, as follows:

$$\frac{da}{dB} = \sum_{i=1}^{100} \left(\frac{da}{dN}\right)_i n_i \tag{2-17}$$

in which n_i is the number of cycles at the ith stress level.

Although the crack length is held constant and the ratio of the stress intensity factor to stress is computed only once at every crack segment, the retardation parameters are changed appropriately for the cycles in each stress level of the loading. The life is computed by numerically integrating the inverted rate per block between the initial and final crack length. The life in seconds is

$$L = \lambda_{gro}\ T \int_{a_i}^{a_f} \frac{da}{da/dB} \tag{2-18}$$

in which λ_{gro} is the uncertainty in the growth calculation and T is the length of a load block in seconds. This calculation is performed as a summation over unequally divided N_{CRL} crack lengths, as follows:

$$L = \lambda_{gro}\ T \sum_{j=1}^{N_{CRL}} \left(\frac{\Delta a}{da/dB}\right)_j \tag{2-19}$$

Comparisons were made between lives predicted using the block approach and the cycle by cycle approach. The block rates were calculated at unequally incremented crack lengths from the initial crack length a_i to the final crack length a_f. By using small crack length increments at the start and larger increments near the end, only twenty-five crack lengths were required to keep the life estimates, by the block approach and by the cycle-by-cycle approach, to within a few percent.

For block growth calculation in two directions, a and c, the crack length increment in the c direction Δc is determined using the information that $\Delta c/\Delta a = (dc/dB/\ da/dB)$, given the increment in the a direction Δa. A flowchart for the crack growth calculations is given in Figure 2.2-4.

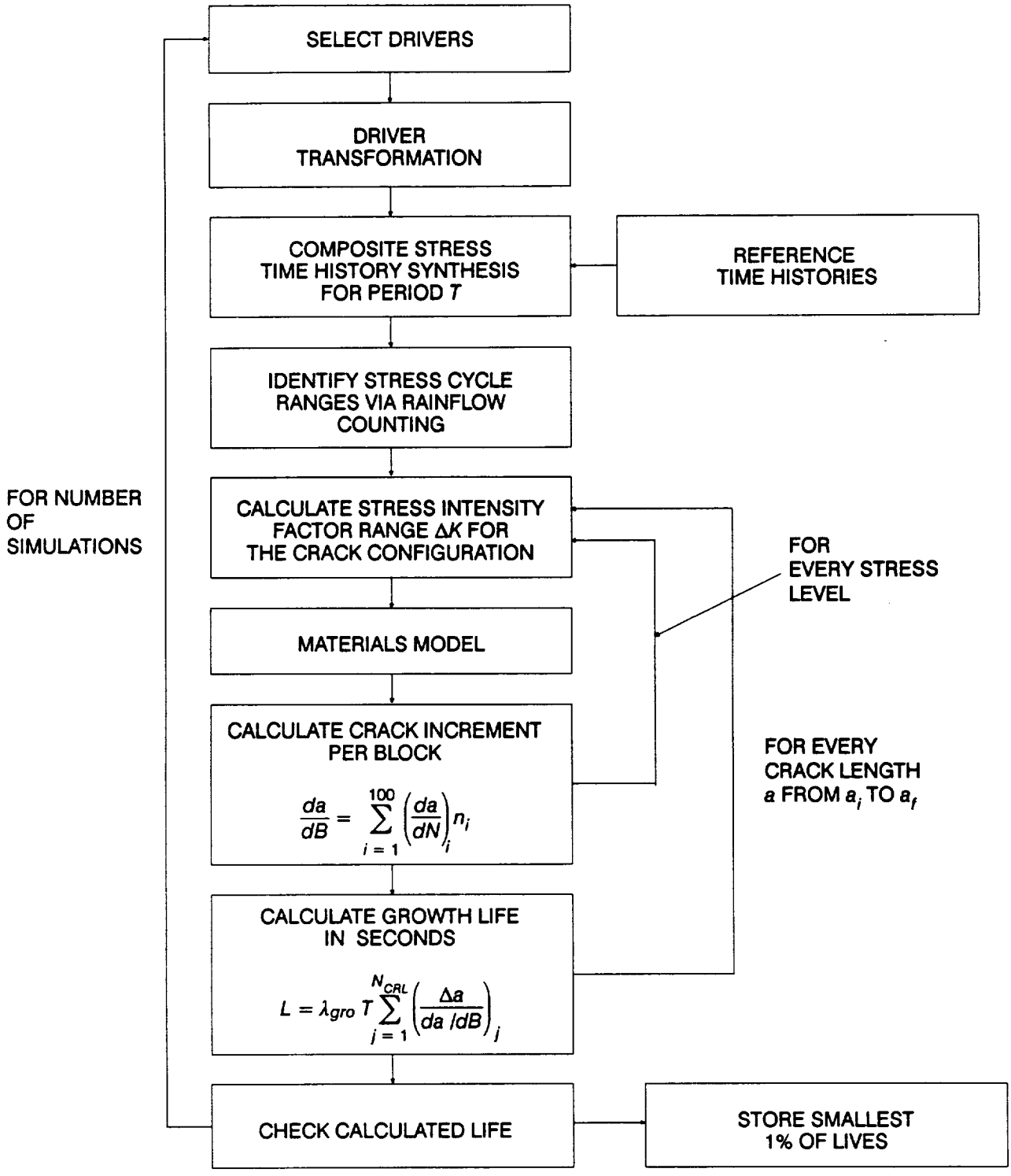

Figure 2.2-4 Flowchart for the Crack Growth Calculations

Section 2.3
Heat Exchanger Coil Case Study

2.3.1 Component Description

The heat exchanger is a coil pack installed in the oxidizer side of the hot gas manifold and is shown in Figure 2.3-1. It converts liquid oxygen tapped from the discharge of the high pressure oxygen turbopump (HPOTP) to gaseous oxygen for the vehicle oxygen tank and the POGO accumulator pressurization system. The cross flow of the hot turbine exhaust gases from the HPOTP provides the heat energy required to gasify the oxygen. The coil pack consists of a helically wound small tube approximately 30 inches long (primary tube) in series with two larger tubes, each approximately 300 inches long (secondary tubes). The tubes are made of 316L CRES stainless steel. The critical location is at weld 3 on the small tube outlet near the bifurcation joint, as shown in Figure 2.3-2. Analyses by Rocketdyne showed that weld 3 stresses control the life for the HEX coil. Failure was attainment of a through-the-thickness crack in the tube wall. A HCF failure analysis for the HEX coil is presented in [1].

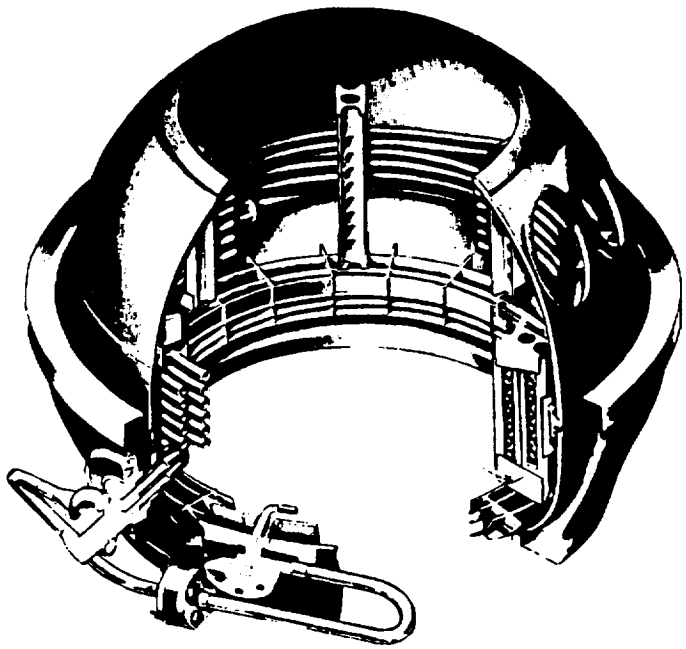

Figure 2.3-1 HPOTP Heat Exchanger

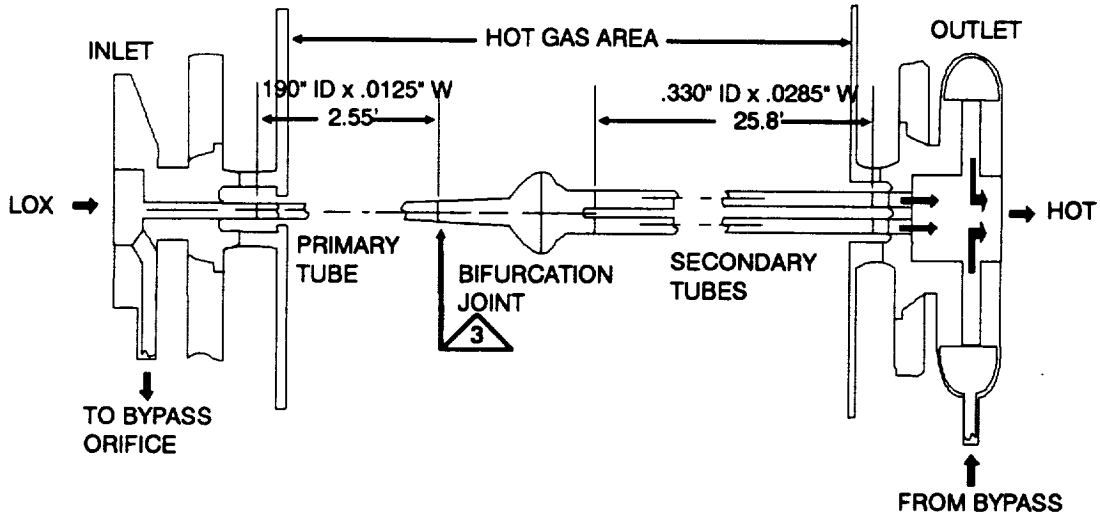

Figure 2.3-2 Detail of the HPOTP Heat Exchanger Coil Near Weld 3

The standard stress intensity factor solution given in NASA/FLAGRO [10] for a semi-elliptic crack in a finite width plate subject to axial and bending stresses was employed to calculate ΔK for the heat exchanger tube. The use of the finite width plate solution for the duct is schematically shown in Figure 2.3-3. The temperature difference across the wall of the tube (cold inside and hot outside) induces significant thermal stresses over the thickness, whose variation across tube thickness is similar to that of bending stresses. Limited finite element analyses were performed to evaluate the approximations involved in using the finite width solution and in modeling the thermal stress as an applied bending load. Standard stress intensity factor solutions for cylinders with radial cracks, subjected to bending stresses over the thickness, are not available. The SIF expressions used in the analysis are given in Appendix 2.D.1.

2.3.1.1 Crack Growth Rate Data

Crack growth rate data [15] were available for welded 316L at stress ratios of R = 0.16, 0.7, and 0.9. The low growth rate data were used to fit the model given by Equation 2-10, which resulted in the following values for threshold stress intensity range model parameters: ΔK_{THo} = 4.03 ksi$\sqrt{\text{in.}}$, C_o = 1.07, and d = 0.163. The entire crack growth data set was employed to derive the parameters of the generalized Forman model which is given by Equation 2-7. This gave the following model parameters: $C = 1.139 \times 10^{-9}$, n = 1.900, m = 0.856, p = 0.478, and q = 0.988. The mean growth rate curves for three stress ratios are given in Figure 2.3-4.

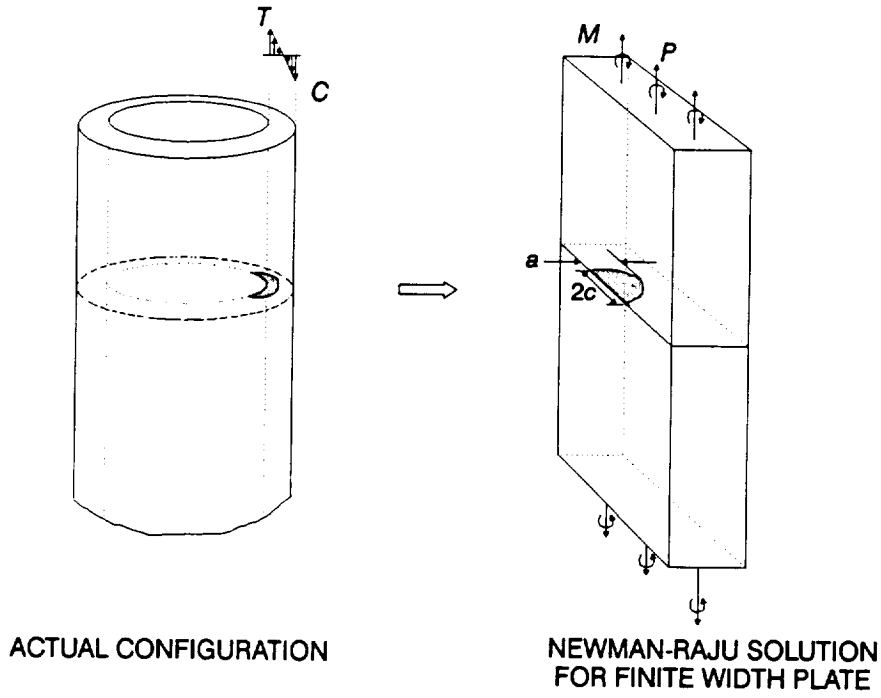

Figure 2.3-3 Schematic of Approximating the SIF Solution for Duct with a Finite Width Plate Solution

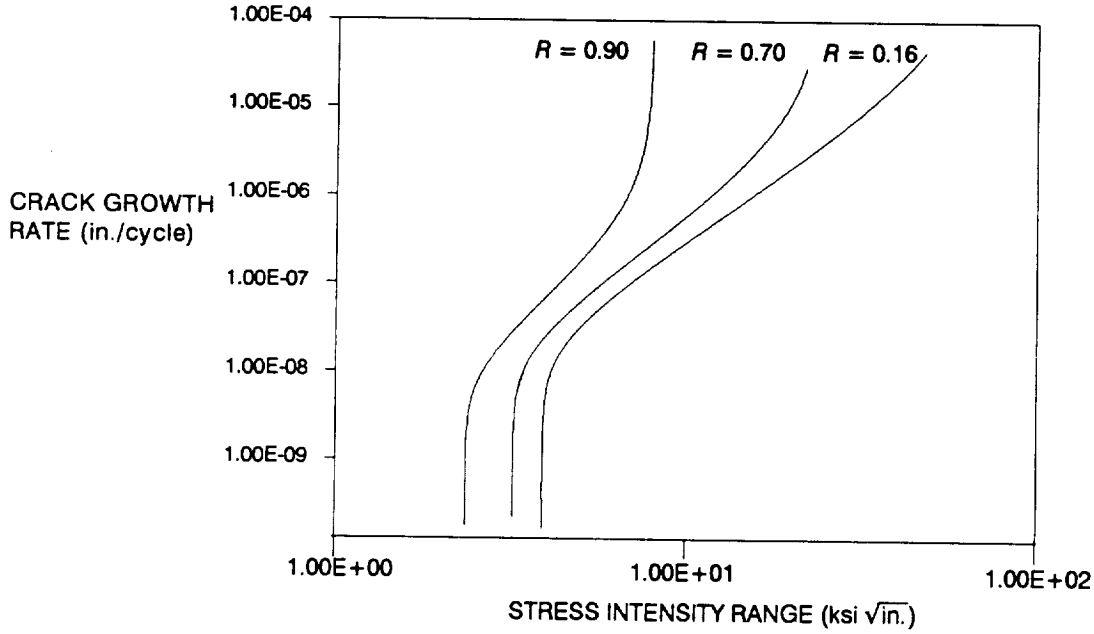

Figure 2.3-4 The Mean Crack Growth Rate Curves for Welded 316L Data

2.3.2 Driver Description

A description of guidelines for driver characterization in a probabilistic failure analysis is given in [1], [3] and [16]. From among the load, dimension, and environment parameters that were used for the HEX coil stress analysis, a total of nineteen drivers were identified. Included were five drivers, which accounts for accuracy of the analysis model. The relative importance of uncertainty in these drivers was studied via a sensitivity analysis described later. The drivers for the HEX coil crack growth analysis, their distributions, and parameters are given in Table 2.3-1. The drivers unique to the crack growth analysis of the heat exchanger are discussed below, and the remaining drivers are discussed in Section 3.2.2 of [1].

In general, the drivers may be uncorrelated or correlated, and the correlation structure may be specified explicitly or implicitly. For many drivers, there are physical reasons why they are uncorrelated. In the HEX coil analysis, all the drivers except the flow conditions (wall temperatures and internal pressure) are uncorrelated. The correlation in the flow conditions was implicitly specified in the driver transformation by requiring the inner and outer wall temperatures and internal pressure to increase and decrease according to the governing physics.

The initial crack shape aspect ratio a/c was modeled using a Uniform distribution with end points of 0.2 and 1.0. The crack geometry was then defined by treating initial crack length, a_i, parametrically. The analysis was run with the value of a_i fixed at 0.001 in., 0.0025 in., 0.005 in., and 0.0075 in. The crack shape distribution was based on an assessment of the crack aspect ratios that could result from the manufacturing process used for the weld joint.

The parameters $\lambda_{K_{TH}}$ and λ_{K_c} were also treated parametrically. From preliminary analysis it was determined that growth would be primarily in the threshold region. Thus, the location of the threshold, i.e., the uncertainty factor $\lambda_{K_{TH}}$, governed crack growth. The tube wall thickness is nominally 0.0125 in., which leads to the concern that "short crack" behavior may be relevant to this case. Short crack growth rate curves have been observed not to have definite thresholds [17]. If a threshold exists, it is a conservative assumption for the linear segment of the curve in the mid-rate region to be extrapolated down into the threshold region. Fixing $\lambda_{K_{TH}} = 0$ in Equation 2-8 accomplishes this, as shown in Figure 2.2-3. Due to lack of any information on short crack behavior of welded 316L, a value of $\lambda_{K_{TH}} = 0$ was employed to bound the failure probability. Analyses were also performed with values of $\lambda_{K_{TH}}$ at 0.1, 0.2, etc., to study the impact of the threshold location. Since growth was in the low rate region, the driver λ_{K_c} was not relevant, and its value was arbitrarily fixed at unity.

Table 2.3-1 Description of Drivers Used in the HEX Coil Analysis

DRIVER	DISTRIBUTION	RANGE
Initial crack size a_i, in.	Fixed	.0010 to .0075
Initial crack shape a/c	Uniform	.2 to 1.0
Threshold stress intensity factor range accuracy factor $\lambda_{K_{TH}}$	Fixed	0.0 to 1.0
Fracture toughness accuracy factor λ_{K_c}	Fixed	0.0 to 1.0
Random load adjustment factor $\lambda_{D_{RANDOM}}$	Normal $k = 2.0$ $C = 0.15$	–
Sinusoidal load adjustment factor $\lambda_{D_{SINUSOIDAL}}$	Normal $k = 2.0$ $C = 0.20$	–
Aerodynamic load factor $\lambda_{AERO_{DYN}}$	Uniform	.5 to 1.5
Aerostatic load factor $\lambda_{AERO_{ST}}$	Uniform	.8 to 1.2
Inner wall temperature T_i (°R)	Normal (μ, σ^2) $\mu \sim$ Uniform (486, 666) $\sigma \sim$ Uniform (29, 56.5)	–
Outer wall temperature T_o (°R)	Normal (μ, σ^2) $\mu \sim$ Uniform (799, 908) $\sigma \sim$ Uniform (48, 49.5)	–
Internal pressure p_i, ksi	Normal (μ, σ^2) $\mu \sim U$ (3.808, 4.177) $\sigma = .069$	–
Inner diameter D_i, in.	Beta (ρ, θ) $\rho = .5$ $\theta \sim$ Uniform (.5, 20)	.1885 to .1915
Wall thickness t, in.	Beta (ρ, θ) $\rho = .27$ $\theta \sim$ Uniform (.5, 20)	.0113 to .0157
Dynamic stress analysis accuracy factor $\lambda_{DYN_{str}}$	Uniform	.8 to 1.2
Static stress analysis accuracy factor $\lambda_{ST_{str}}$	Uniform	.9 to 1.1
Stress intensity factor calculation accuracy factor λ_{sif}	Uniform	.9 to 1.1
Growth calculation accuracy factor λ_{gro}	Uniform	ln ½ to ln 1.75
Neuber's rule accuracy factor λ_{neu}	Uniform	.6 to 1.4
Weld offset stress concentration accuracy factor λ_{OFF}	Uniform	.8 to 1.2

The stress intensity factor calculation accuracy factor λ_{sif} accounts for the error in the standard stress intensity factor solution and the uncertainty associated with employing a finite width plate solution for a crack in a cylinder. A Uniform distribution was used for λ_{sif} with a range of 0.9 to 1.1. These values are based on the reported error for the stress intensity factor expressions and the level of approximation estimated for this application. The growth calculation accuracy factor λ_{gro} accounts for uncertainties in the block-by-block growth calculation and in transformation of a variable amplitude stress history to a constant amplitude stress vs. number of cycles table using rainflow counting. Evidence in the literature indicates that factors of two between the calculated crack growth life and tests are appropriate. Since crack propagation is the result of a number of multiplicative events, the distribution on λ_{gro} was specified in log space. A Uniform distribution was used with the lower bound set at ln(1/2). In order for the mean value of λ_{gro} to be 1.0, the upper bound was set at ln(1.75).

2.3.3 Analysis

The program PROCRK was employed for probabilistic crack growth analysis of the HEX coil. MC simulations were used to derive the failure life distribution. Static and dynamic analyses to determine beam-end forces were conducted by Rocketdyne on 3-D finite element models. The static analyses took account of the loads due to misalignment, gimbaling, acceleration, and fluid momentum. Static beam-end forces were obtained at a node closest to the critical location from these analyses. Similarly, the RV analyses provided the RMS beam-end forces and the expected frequencies, and the FR analyses gave the beam-end force amplitudes at the critical location. The beam-end forces from the static and dynamic analyses were used in the crack growth failure analysis performed at JPL. Before performing failure analyses, preliminary analyses were made to identify the worst circumferential location and to choose a suitable load history length and a random number seed for the stochastic reference time histories.

In general, the worst circumferential location on a pipe does not necessarily lie on the bending axes since multi-axial moments can cause the highest stresses to occur anywhere around the circumference of the pipe. Thus, the worst location was identified by computing single fatigue life values (i.e., a deterministic run with nominal values) for different circumferential positions on the duct. This involved repeating the analyses and varying angle ϕ in Equation 2-1. The critical circumferential angle corresponds to the analysis with minimum life.

The stochastic reference histories are generated for a given length (in seconds) of load history. The suitable length for a specific problem is determined by calculating single fatigue lives, each time increasing history lengths, until the change in the lives becomes negligible. The histories are generated using a random number

stream as described in Section 2.1.4 of [1]. Since finite length histories are employed to keep computational costs down, the occurrence of peaks in the histories will vary with different random number streams. The random number stream is based on the random number seed input for the analysis. The suitable random number seed is selected by generating reference time-histories for 21 seeds and calculating a single fatigue life for each history. The chosen seed is the one that gave the median life from among the 21 lives calculated. The details of the analysis are given in Appendix 2.B.

2.3.4 Results

The results of the failure simulation are given in Figures 2.3-5, 2.3-6, and 2.3-7. Input and output files for the analysis are given in Appendix 2.C.1. The graphs in Figures 2.3-5 and 2.3-6 present the left-hand tail of the failure distribution for different values of drivers that were treated parametrically. The ordinate of these graphs is the failure probability. The abscissa is the life in seconds for crack growth through the thickness of the HEX Coil. The life at 1/1000 failure probability (sometimes denoted by B.1) is usually of interest. The graph in Figure 2.3-7 illustrates the effects of the crack growth threshold and initial crack size on B.1 life.

The life estimates in Figures 2.3-5 and 2.3-6 are for a conservative crack growth threshold, modeled by setting $\lambda_{K_{TH}} = 0$. The results in Figure 2.3-5 are given for an initial crack size $a_i = 0.005$ in. The left curve labeled "all driver variation" is for a simulation where all the drivers were allowed to vary except a_i, $\lambda_{K_{TH}}$, and λ_{K_c}. The "nominal" value shown on the graph is for an analysis with all the drivers fixed at their nominal or most likely values. Measures of the relative importance of individual drivers are given in the upper left corner in Figure 2.3-5. These were obtained by finding marginal effects of driver uncertainties on B1 lives using several sensitivity runs, where one driver was allowed to vary while the rest were held at their nominal values. The crack shape and the growth calculation accuracy are the most important drivers with a 90% contribution to decrease in life. The right-hand curve in Figure 2.3-5 shows the shift to the left due to the variation in the crack shape and growth calculation accuracy. It was also determined that dynamic loads variation, weld offset accuracy, stress calculation accuracy, and stress intensity factor calculation accuracy are moderately important drivers. Neuber's rule accuracy and inner diameter are not important drivers.

The impact of initial crack size a_i on life is shown in Figure 2.3-6. The B.1 life at 95% assurance decreases from 1.5×10^5 seconds to about 2.5×10^4 seconds when the initial crack size increases from 0.001 in. to 0.0075 in.

For this application, uncertainty due to incomplete knowledge and limited information concerning the accurate characterization of analysis models and physical

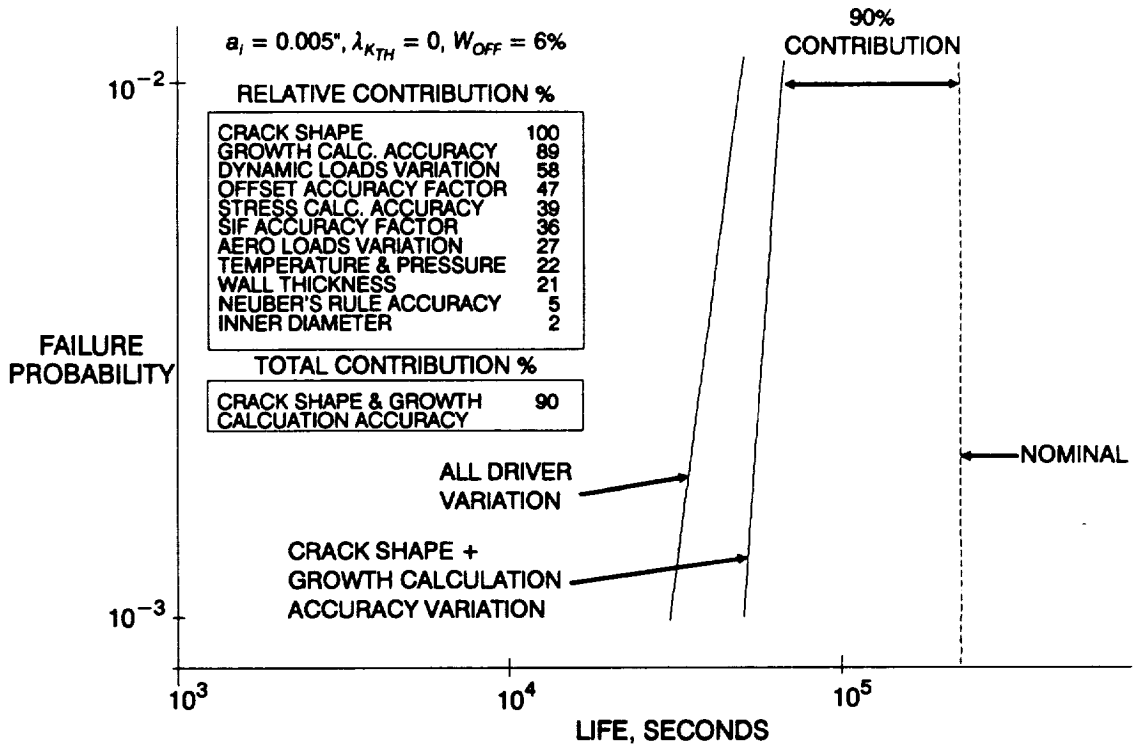

Figure 2.3-5 Failure Life Distributions and Driver Sensitivities for HEX Coil

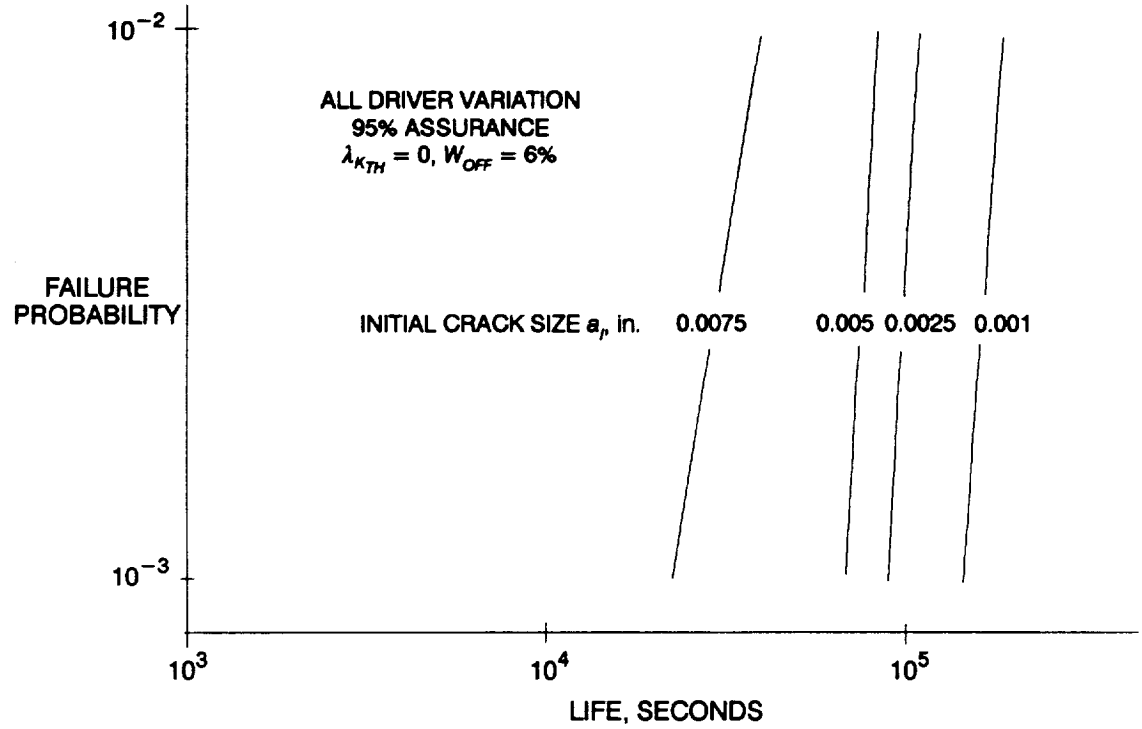

Figure 2.3-6 Impact of Initial Crack Size a_i on Failure Life Distributions for HEX Coil

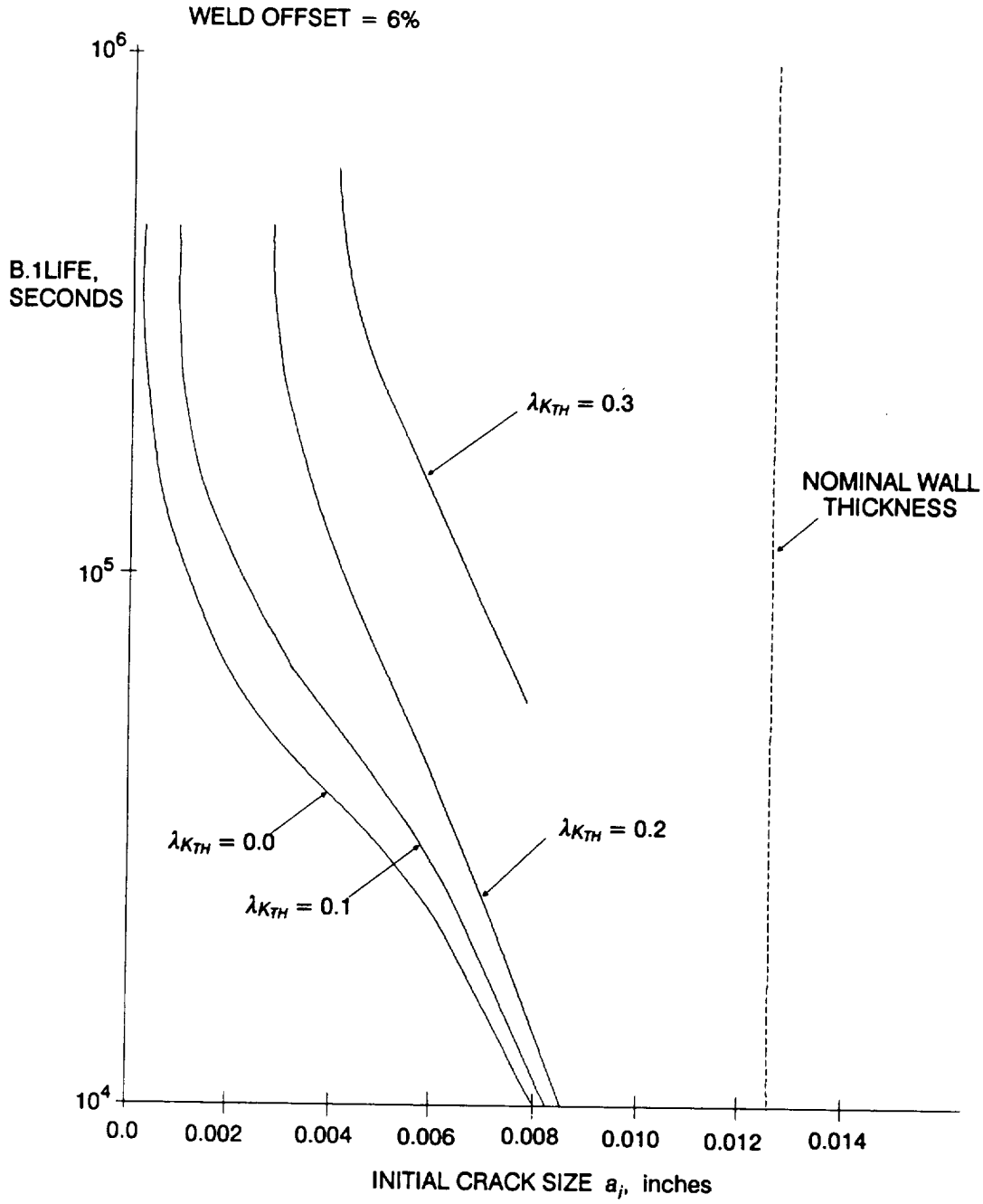

Figure 2.3-7 Effect of Initial Crack Size and Crack Growth Threshold on B.1 Life for HEX Coil

driver parameters have a much larger impact on what we can say about failure risk than does any intrinsic parameter variability. For the HEX Coil, the information available was insufficient to meaningfully characterize initial crack size and threshold stress intensity factor for "short cracks". Consequently these important drivers were treated parametrically in order to show their impact on crack growth life and to better define information that is needed to reduce failure risk. A tradeoff between knowledge of initial crack size and knowledge of short crack threshold stress intensity factor, conditioned on the uncertainties in other drivers, can be inferred from the results shown in Figure 2.3-7.

It can be seen from Figure 2.3-7 that, for a conservative "short crack" threshold ($\lambda_{K_{TH}} = 0$) assumption, inspection techniques that can detect 0.005 in. initial cracks with high reliability are required to achieve a life of about 3×10^4 seconds. On the other hand, if more representative crack growth data can be generated that can reliably establish a nonzero growth threshold ($\lambda_{K_{TH}} > 0$), then the requirements on the inspection may be relaxed while achieving the same B.1 life. A summary of the probabilistic crack growth model and the HEX coil analysis and results may be found in [18].

Section 2.4
External Heat Exchanger Case Study

2.4.1 Component Description

The Block II design of the proposed external heat exchanger, shown in Figure 2.4-1, consisted of an inner core of about 300 zirconium copper (ZrCu) platelets and two stainless steel end plates. The ZrCu core contained about 450 channels per fuel or oxidizer circuit. The arrangement of the channels in a portion of the core is shown in Figure 2.4-2. The critical location was taken to be at the channel corners at mid height of the core based on the highest stress under steady state conditions. Failure was propagation of the crack to the adjacent channel.

The crack configuration used for the analysis was a crack in a finite width plate subject to tension [19] shown in Figure 2.4-3. The initial size of the crack is taken as the width of the channel of interest. The width W used for SIF calculation is taken as the width of the adjacent land area and the channel width. The SIF expressions for this crack configuration are given in Appendix 2.D.2.

2.4.1.1 Crack Growth Rate Data

Crack growth rate data was not available for bonded ZrCu material. Limited C10100 copper crack growth data [20] available from NASA/JSC was used as proxy for the ZrCu crack growth data. This crack growth data for $R = 0.2$ was employed for the regression to derive the parameters C and n of the generalized Forman model, which is given by Equation 2-7. Since growth data was not available for different R values, m could not be derived by fitting this data, and m was set to – 2.0 based on values observed for similar materials. Also, due to sparsity of data, the other Forman constants were set to $p = 0$ and $q = 0$ for performing the regression. The regression gave the model parameters: $C = 3.273 \times 10^{-9}$ and $n = 4.148$. The value of m was treated as a stochastic driver as described in the next section. The copper crack growth data did not extend into the threshold region and reliable threshold region data could not be found for copper or its alloys. Hence, a conservative zero threshold was used in the analysis as described below. The C10100 data employed and the mean growth rate curve for $R = 0.2$ stress ratio is given in Figure 2.4-4.

2.4.2 Driver Description

A total of ten drivers were identified for the EXHEX analysis. The drivers for the EXHEX crack growth analysis, their distributions, and parameters are given in Table 2.4-1. The drivers unique to the crack growth analysis of the EXHEX are dis-

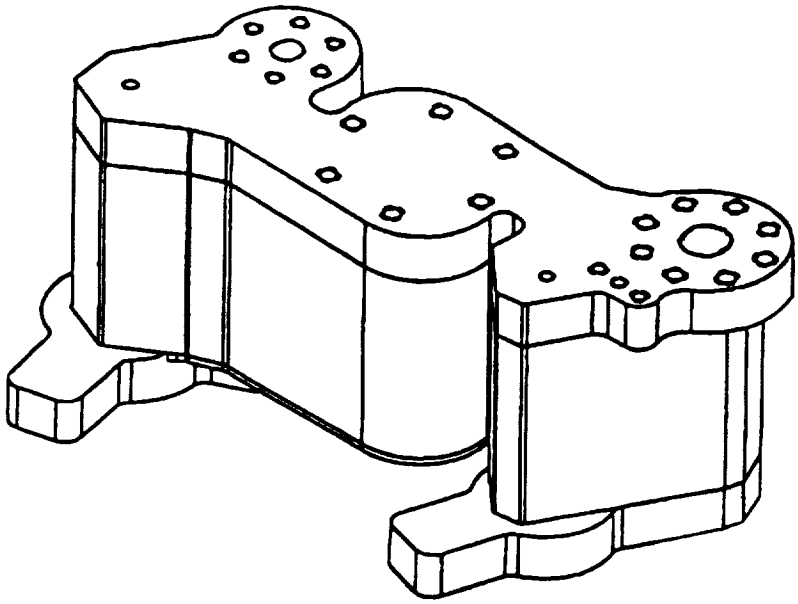

Figure 2.4-1 Proposed External Heat Exchanger Block II Design

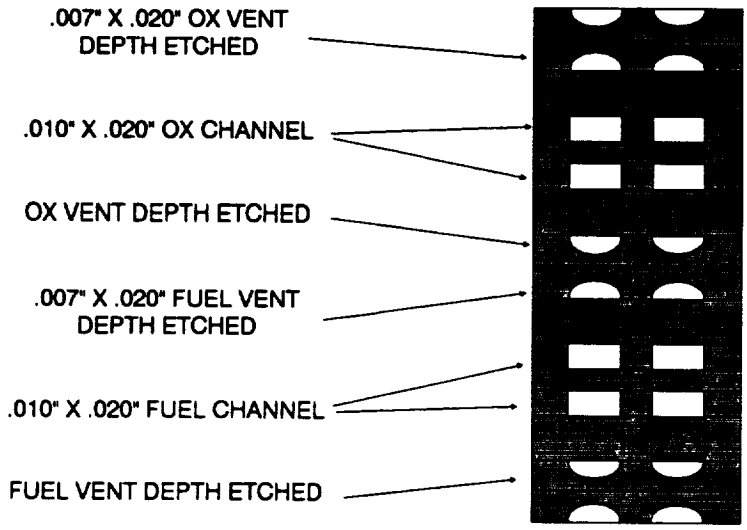

Figure 2.4-2 Arrangement of the Channels in the EXHEX

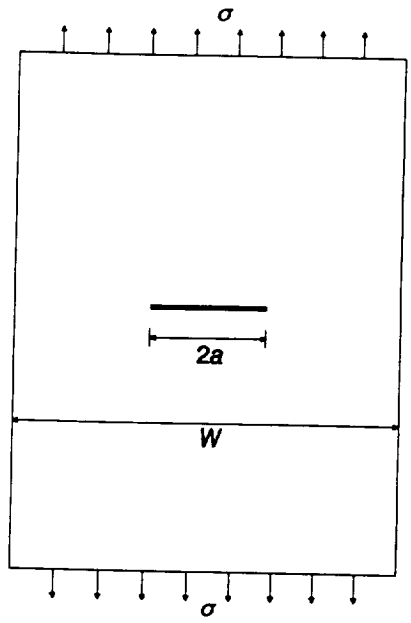

Figure 2.4-3 Crack Configuration Used for EXHEX Channel

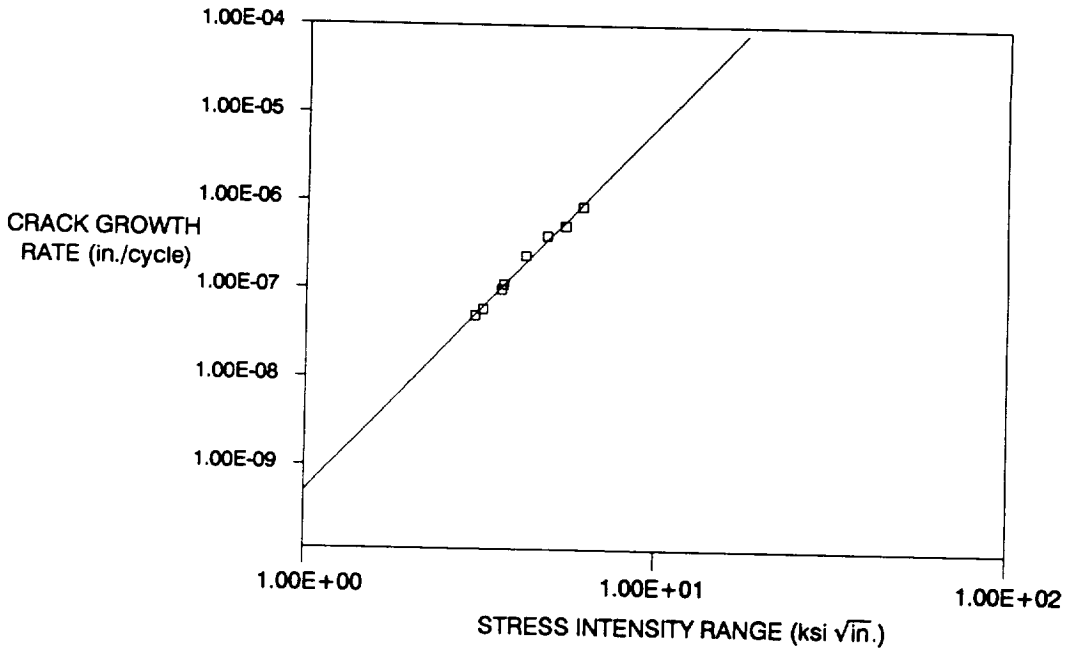

Figure 2.4-4 Crack Growth Data for C10100 Copper and Mean Curve with $\lambda_{k_{TH}} = 0$

Table 2.4-1 Driver Distributions for EXHEX

DRIVER	DISTRIBUTION	RANGE
Initial crack size a_i, in.	Uniform	0.009 to 0.011
Width W, in.	Uniform	0.054 to 0.066
Threshold stress intensity factor range accuracy factor $\lambda_{K_{TH}}$	Fixed	0.0 to 1.0
Critical stress intensity factor accuracy factor λ_{K_c}	Fixed	0.0 to 1.0
Random load adjustment factor $\lambda_{D_{RANDOM}}$	Normal $k = 2.0$ $C = 0.15$	–
Sinusoidal load adjustment factor $\lambda_{D_{SINUSOIDAL}}$	Normal $k = 2.0$ $C = 0.20$	–
Dynamic stress analysis accuracy factor $\lambda_{DYN_{str}}$	Uniform	.8 to 1.2
Stress intensity factor calculation accuracy factor λ_{sif}	Uniform	.9 to 1.10
Growth calculation accuracy factor λ_{gro}	Uniform	ln ½ to ln 1.75
Crack growth coefficient m variation	Uniform	– 1.5 to – 2.5

cussed below, and the remaining drivers are discussed in Section 2.3.2 above and Section 3.2.2 of [1].

The initial crack, a_i, was assumed to be the size of the channel with a nominal value of 0.010 in. The uncertainty in the initial crack size was assumed to be a Uniform distribution with a range of 0.009 in. to 0.011 in. which results from a likely manufacturing tolerance of 10%. The width W for the SIF solution is the distance between the middle of the areas on both sides of the channel, as shown in Figure 2.4-3, with a nominal value of 0.060 in. Similar to the initial crack size, the uncertainty was assumed to be 10%, and the width was Uniformly distributed in the range of 0.054 in. to 0.066 in.

The parameters $\lambda_{K_{TH}}$, and λ_{K_c} were treated parametrically, similar to their treatment in the HEX coil analysis described in Section 2.3.2. Since no reliable data on the crack growth threshold was available, it is a conservative assumption for the linear segment of the curve in the mid-rate region to be extrapolated down into the

threshold region. Fixing $\lambda_{K_{TH}} = 0$ in Equation 2-8 accomplishes this, as shown in Figure 2.2-3. Also, since growth was not in the high rate region, the driver λ_{K_c} was not relevant, and its value was arbitrarily fixed at unity.

Since copper crack growth data was not available for different stress ratios R, the Forman constant m could not be derived from the least squares fit of Equation 2.7. The nominal value of m was assumed to be – 2.0 and was used for the least squares fitting of the Forman constants C and n. The uncertainty in m was assumed to Uniformly vary between – 1.5 and – 2.5.

2.4.3 Analysis

The probabilistic crack growth analysis of the EXHEX was performed using the program PROCRK. Static and dynamic analyses to determine the stresses were conducted by Aerojet using ANSYS. The static analyses were performed on a plane strain FE model and the loads were due to internal pressure and temperature. The dynamic analyses were performed on an FE model with isoparametric solid elements consisting of approximately 400 nodes. The dynamic model employed a solidity factor [8] to assign properties to solid regions and channeled regions of the ZrCu core. The inverse of the solidity factor was used to recover the stresses from the analysis within these regions. The stochastic reference histories were generated for a given length (in seconds) of load history using a random number stream as described in Section 2.1.4 of [1].

2.4.4 Results

The results of the failure simulation are given in Figure 2.4-5. The input and output files for the analysis are given in Appendix 2.C.2. The graphs in Figure 2.4-5 present the left-hand tail of the failure distribution for different values of drivers that were treated parametrically. The ordinate of these graphs is the failure probability. The abscissa is the life in seconds for the crack to grow the width of the land area in the EXHEX core.

The life estimates in Figures 2.4-5 are for a conservative crack growth threshold, modeled by setting $\lambda_{K_{TH}} = 0$. The left-hand curve labeled "all driver variation" is for a simulation where all the drivers were allowed to vary except $\lambda_{K_{TH}}$ and λ_{K_c}. The "nominal" value shown on the graph is for an analysis with all the drivers fixed at their nominal or most likely values. Measures of the relative importance of individual drivers are given in the upper left corner in Figure 2.4-5. These were obtained by finding marginal effects of driver uncertainties on B1 lives. The dynamic loads variation, Forman parameter m variation, and growth calculation accuracy are, together, the most important drivers with a 93% contribution to decrease in

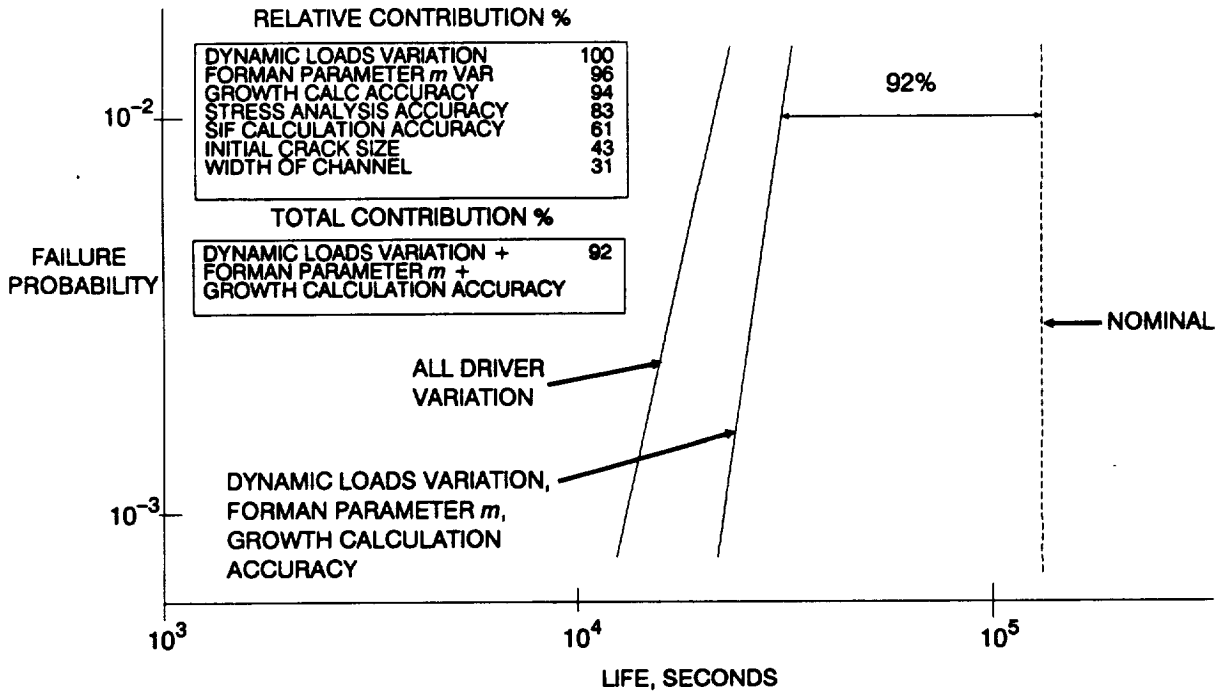

Figure 2.4-5 EXHEX Failure Life Distribution and Driver Sensitivities

life. The right curve in Figure 2.4-5 shows the shift to the left due to the variation in these three important drivers.

This is a preliminary analysis of the EXHEX and it was performed with proxy copper C10100 material data for ZrCu, a conservative SIF solution for a crack at a channel corner, and under the assumption that the steady state conditions were critical and that the dynamic loads controlled the life of the component.

Section 2.5
Analysis Procedure

2.5.1 Introduction

The procedure for conducting a probabilistic analysis of the crack growth failure mode is outlined here. The relevant statistical and engineering theory is given in Section 2.1 of [1] and Section 2.2 of this document, respectively.

The overall procedure is schematically described in Figure 2.5-1. Since the procedure for fatigue failure mode analyses described in Section 2.3 of [1] is similar to that for the crack growth failure mode, only the materials characterization step that differs from the fatigue analyses procedure will be described here. A detailed description of driver characterization, preliminary deterministic analysis, driver transformation, probabilistic failure model formulation, time history definition, significant parameter identification, probability of failure curve parameter estimation, driver sensitivity analysis, Bayesian updating, and probability of failure curve standardization is given in Section 2.3 of [1].

The driver characterization and preliminary deterministic analysis steps are carried out in parallel. This information is then utilized in the driver transformation step. For fatigue and crack growth failure modes, the driver transformation is the mapping of the applied loads to stress or strain at the critical location. The key step in the procedure is the formulation of the probabilistic failure model. This step incorporates the driver transformation, stress history, materials characterization, and the damage accumulation model in a stochastic simulation structure. The materials characterization is described in Section 2.5.2.

Once the probabilistic model is in place, a set of abbreviated probabilistic analyses is often employed to identify and eliminate non-life controlling parameters (e.g., insignificant load components). This step is optional and it was employed in the EXHEX analysis to identify the significant load components. The next step in the procedure is a simulation consisting of 10,000 trials. This is followed by the driver sensitivity analysis, the inclusion of operating experience by Bayesian updating, and the standardization of the probability of failure curve to a desired assurance level.

2.5.2 Materials Characterization

Materials characterization is the process of using the information available to provide a probabilistic representation of material properties. For the crack growth applications, the materials characterization model described in Section 2.2.3 has

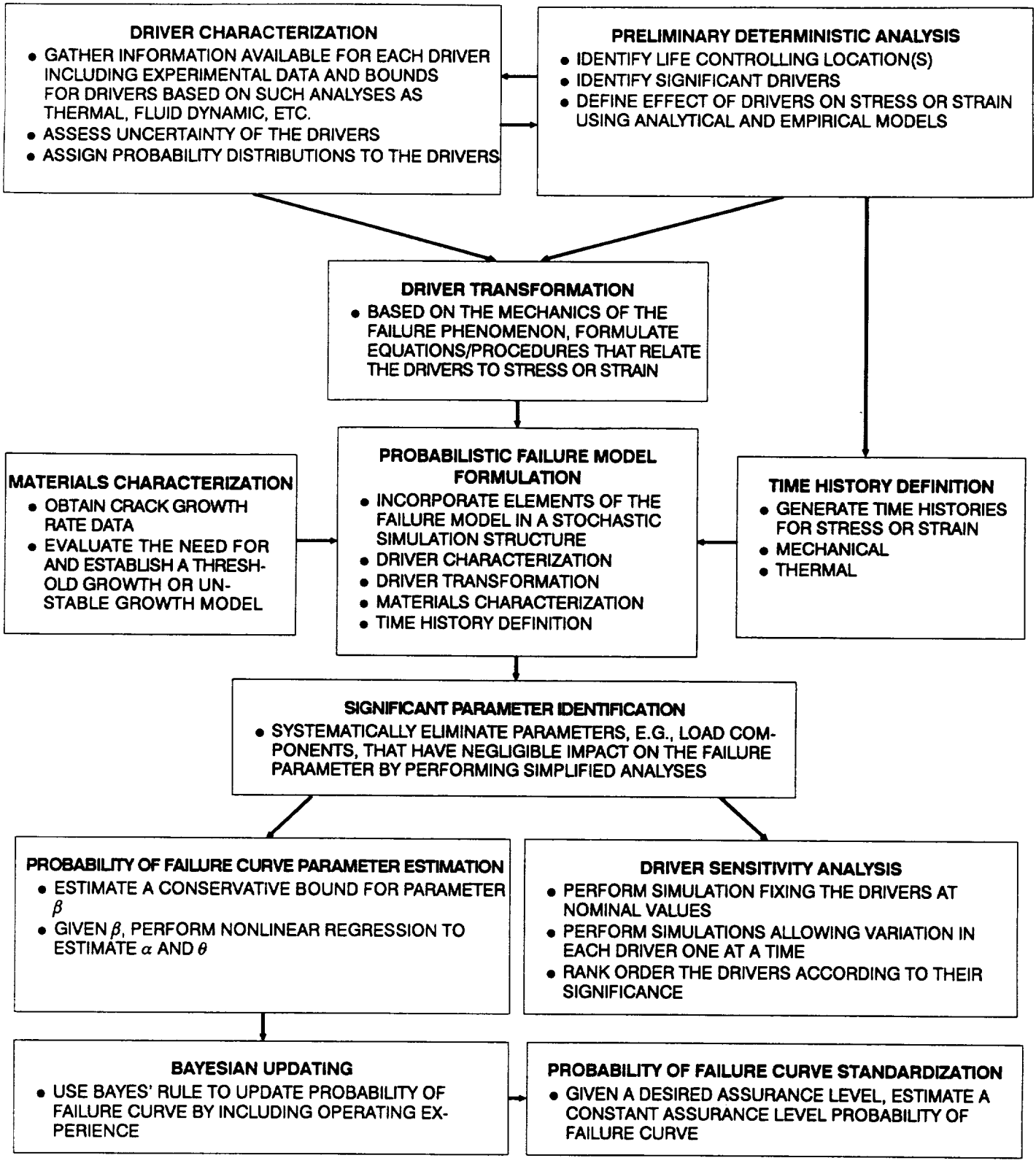

Figure 2.5-1 Overall Procedure for Crack Growth Failure Mode

been used. The generalized Forman equation, given by Equation 2-7, was used to characterize mean crack growth behavior in the two applications described in Sections 2.3 and 2.4. A least squares fit is performed to derive the Forman constants from crack growth data for the component material. The first step is to seek crack growth rate test data generated under conditions that are the same or similar to the application. Since loading for the component will not be constant amplitude loading, it is desirable to have the crack growth data for different stress ratios R. Some preliminary calculations may be performed to determine if growth for the application is predominantly in the low-rate (threshold), mid-rate, or high-rate (unstable growth) region of crack growth for the specific material. It is then important to ensure that crack growth data is available for the region of interest. If the region of interest is the low-rate or the high-rate region, empirical relationships may be established to model the variation of the material properties ΔK_{TH} and K_c which define the asymptotes in the Forman equation. For example, if the threshold crack growth rate region is important, a ΔK_{TH} vs. R model may be established using crack growth rate data in the threshold region in order to define the lower asymptote (i.e., the growth/no-growth boundary in crack growth calculations). Such a model is given by Equation 2-10 and it was used for the HEX coil application.

References

[1] Moore, N., et al., An Improved Approach for Flight Readiness Certification – Methodology for Failure Risk Assessment and Application Examples, JPL Publication 92-15, Jet Propulsion Laboratory, California Institute of Technology, Pasadena, California, June 1, 1992.

[2] Madsen, H. O., Krenk, S. O., and Lind, N. C., Methods of Structural Safety, Prentice Hall, Englewood Cliffs, New Jersey, 1986.

[3] Moore, N., et. al., "A Methodology for Probabilistic Prediction of Structural Failure of Launch Vehicle Propulsion Systems," Paper No. 90-1140-CP, Proceedings of the AIAA 31st Structures, Structural Dynamics and Materials Conference, April, 1990, pp. 1092 - 1104.

[4] Sutharshana, S., et al., "Computational Methods for Probabilistic Flaw Propagation Analyses," Proceedings of the ASCE Structures Congress '91, April, 1991.

[5] SSME Structural Loads Criteria, Rockwell International, RSS-8561-22, October, 1987.

[6] STARDYNE User Information Manual, MRI, 1984.

[7] ASME Boiler and Pressure Vessel Code, Division 1, NB-3600, 1989.

[8] ANSYS User Manual.

[9] SSME EXHEX Probabilistic Design Assessment Fracture Mechanics Model (Phase 1), ATCHEX-900201-1, Aerojet TechSystems, Sacramento, California, February, 1990.

[10] Fatigue Crack Growth Computer Program, "NASA/FLAGRO" Manual, NASA/JSC 22287, 1986.

[11] Virkler, D. A., Hillberry, B. M., and Goel, P. K., "Statistical Nature of Fatigue Crack Propagation," Journal of Engineering Materials and Technology, ASME, Vol. 101, April, 1979, pp. 148 - 153.

[12] Ghonem, H., and Dore, S., "Experimental Study of the Constant-Probability Crack Growth Curves Under Constant Amplitude Loading," Engineering Fracture Mechanics, Vol. 27, No.1, 1987, pp. 1 - 25.

[13] Gallager, J. P., and Hughes, T. S., "Influence of the Yield Stress on the Overload Affected Fatigue Crack Growth Behavior of 4340 Steel," AFFDL-TR-74-27, Air Force Flight Dynamics Laboratory, Wright-Patterson Air Force Base, Ohio, 1974.

[14] Brussat, T. R., "Rapid Calculation of Fatigue Crack Growth by Integration," Fracture Toughness and Slow Stable Cracking, ASTM STP 559, American Society of Testing of Materials, 1974, pp. 298 - 311.

[15] "Fatigue Crack Growth Rate Testing of Welded 316L," Rocketdyne Division, Rockwell International, Canoga Park, California, 1989.

[16] Moore, N., Ebbeler, D., and Creager, M., "Probabilistic Service Life Assessment," Reliability Technology – 1992, AD-Vol. 28, American Society of Mechanical Engineers, November, 1992, ISBN 0-7918-1095-X.

[17] Morris, W. L., and James, M. R., "Investigation of the Growth Threshold for Short Cracks," Proceedings of the International Symposium on Fatigue Crack Growth Threshold Concepts, AIME, October, 1983, pp. 479 - 495.

[18] Sutharshana, S., et al., "A Probabilistic Fracture Mechanics Approach for Structural Reliability Assessment of Space Flight Systems," Advances in Fatigue Lifetime Predictive Techniques, Special Technical Publication 1122, American Society for Testing and Materials, 1991.

[19] Broek, D., Elementary Engineering Fracture Mechanics, Martinus Nijhoff Publishers, Dordrecht, The Netherlands, 1986.

[20] "Fatigue Crack Growth Rate Data for Copper," NASA/JSC, Houston, Texas, 1990.

Appendix 2.A
List of Symbols

a	half crack length or crack depth for surface flaw; a_i = initial crack size; a_f = final crack size; a_o = crack size at overload; Δa = crack length increment
A	cross-sectional area of duct
c	half crack length for surface flaw; c_i = initial crack size; Δc = crack length increment
C	generalized Forman equation parameter
$\frac{da}{dN}$	cycle crack growth rate
$\frac{da}{dB}$	block crack growth rate
E	Young's modulus
F	stress intensity factor (SIF) coefficient for modifying stress; F_o = SIF coefficient for tensile stress; F_2 = SIF coefficient for bending stress
F_k	stress reduction factor to calculate the weld offset stress concentration factor
I	cross-sectional moment of inertia of duct
K	stress intensity factor; K_c = critical SIF; K_{max} = maximum SIF; $K_{max.eff}$ = maximum effective SIF after retardation; $K_{max.req}$ = SIF required to extend the current plastic zone boundary; K_{min} = minimum SIF; $K_{min.eff}$ = minimum effective SIF after retardation; K_{red} = reduction in SIF at current load due to size of plastic zone
K_{OFF}	stress concentration due to weld offset
L	crack growth life in seconds
m	generalized Forman equation parameter
M	moment; M_x = moment about x-axis; M_y = moment about y-axis; M_z = moment about z-axis
n	generalized Forman equation parameter
N	number of simulation trials
N_{CRL}	number of crack lengths
$NLOAD$	total number of dynamic load sources

p	generalized Forman equation parameter
p	pressure; p_i = internal pressure; p_o = external pressure
P	axial force along x-axis
r_p	plastic zone size in retardation; r_{po} = plastic zone size at overload
q	generalized Forman equation parameter
R	radius; R_i = internal duct radius; R_m = mean duct radius; R_o = external duct radius
R	stress ratio = K_{min} / K_{max}; R_{eff} = effective stress ratio after retardation
RSO	Willenborg retardation model parameter
S	stress; S_o = tensile stress; S_2 = bending stress
T	length of reference time history in seconds
T	temperature; T_{in} = temperature at the duct inner wall; T_{out} = temperature at the duct outer wall
t	wall thickness of duct
V	shear force; V_y = shear along y direction; V_z = shear along z direction
W	plate width
W_{OFF}	decimal equivalent percentage weld offset for duct
α	thermal coefficient of expansion
ΔK	stress intensity factor range ($K_{max} - K_{min}$); ΔK_{eff} = effective SIF range after retardation; ΔK_{TH} = threshold SIF range; ΔK_{THo} = threshold SIF range at $R = 0$
ΔT	temperature difference across duct wall ($T_{in} - T_{out}$)
γ	geometry factor for plastic zone size used in retardation
I	cross-sectional moment of inertia of duct
λ	accuracy or uncertainty factor; $\lambda_{AERODYN}$ = aerodynamic load factor; λ_{AEROST} = aerostatic load factor; λ_{Di} = accuracy factor on the ith dynamic load source; λ_{DYNstr} = dynamic stress analysis accuracy; λ_{gro} = growth calculation accuracy factor; λ_{K_c} = critical stress intensity factor accuracy; $\lambda_{K_{TH}}$ = threshold stress intensity factor range accuracy; λ_{neu} = Neuber's rule accuracy factor; λ_{OFF} = weld offset accuracy factor for duct; λ_{sif} = stress intensity factor calculation accuracy; λ_{ST} = accuracy factor on the static load source; $\lambda_{ST_{str}}$ = static stress analysis accuracy
ν	Poisson's ratio

ϕ angle between z-axis and critical location on the circumference of the tube

σ stress; $\sigma(t)$ = principal stress history; $\sigma_{Di}(t)$ = time history due to *i*th dynamic load source; $\overline{\sigma_{Di}}$ = non-time varying stress amplitude; $\overline{\sigma_{Dix}}$ = non-time varying stress amplitude due to load in the x direction; $\overline{\sigma_{Diy}}$ = non-time varying stress amplitude due to load in the y direction; $\overline{\sigma_{Diz}}$ = non-time varying stress amplitude due to load in the z direction; $\sigma_i(t)$ = reference time history for *i*th load source; $\sigma_{ix}(t)$ = reference time history for *i*th x-direction load source; $\sigma_{iy}(t)$ = reference time history for *i*th y-direction load source; $\sigma_{iz}(t)$ = reference time history for *i*th z-direction load source; σ_{MEAN} = mean stress; σ_{ST} = stress due to static loads; σ_{TH} = thermal stress; σ_x = longitudinal or axial stress; σ_y = yield stress; σ_z = stress along the z direction

Appendix 2.B
Details of Probabilistic Failure Analysis

2.B.1 Introduction

The details of Probabilistic Failure Assessment (PFA) application for the HPOTP Heat Exchanger Coil crack growth analysis are given here. Each step of the procedure, including intermediate calculations and results, is presented. The general procedure for the PFA methodology is given in Section 2.5 of this document and Section 2.3 of [1].

2.B.2 Selecting the Component, Failure Mode, and Critical Location

The HEX coil is a critical component since a leak in the coil carrying liquid oxygen can cause the liquid oxygen to mix with the hydrogen outside and cause loss of the system. The failure mode and critical location for this study were based on the deterministic analyses that had been performed for the HEX coil by Rocketdyne. Since the HEX coil was already in operation at the time of this study, deterministic stress analyses were available for the component. These deterministic analyses indicated that the stresses at the small tube outlet weld would govern crack growth life. Thus, it was deemed appropriate to apply the PFA methodology to evaluate its crack growth failure risk.

2.B.3 Preliminary Deterministic Analysis

The stress, thermal, and fluid flow deterministic analyses performed by Rocketdyne were used for formulating the driver transformation and to identify and characterize driver distributions for the PFA. The Rocketdyne stress analyses included random vibration and frequency response dynamic analyses.

The radius of bend for the coil was relatively large as compared with its cross-sectional dimensions. This allowed the tube to be considered as a straight pipe for the stress analysis. As described in Section 2.2.2.1, the beam-end forces close to weld 3 were extracted from FE analyses conducted by Rocketdyne on a beam model of the HEX coil. The node and element numbers for the beam model are shown in Figure 2.B-1. The beam-end forces at node 27 are given in Table 2.B-1. The aerodynamic loads on the coil due to flow past it were provided by Rocketdyne as the maximum static and dynamic stress values. The aerodynamic beam-end forces given in Table 2.B-1a were estimated from the stresses by assuming the coil to be a simple beam.

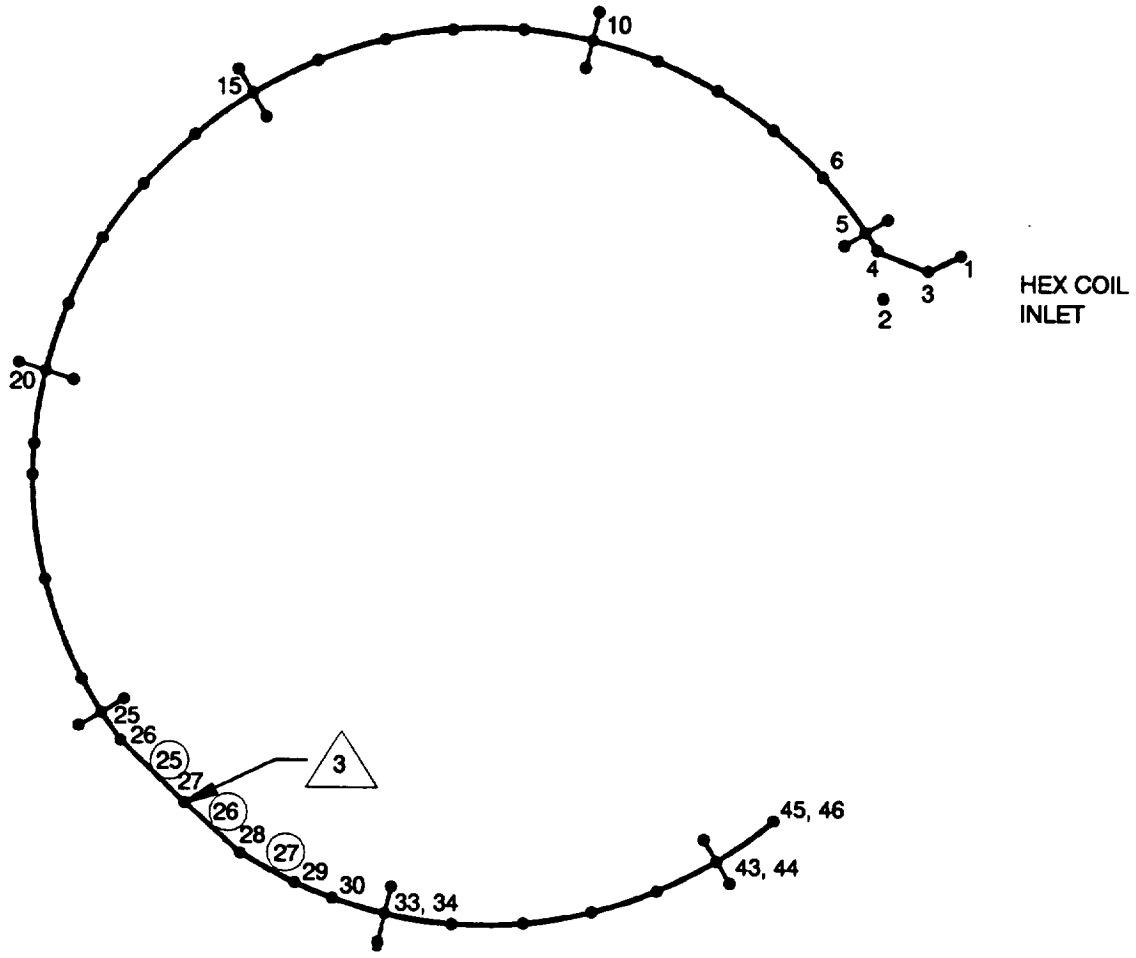

Figure 2.B-1 Finite Element Discretization of HPOTP Heat Exchanger Coil-Forces Extracted from Node 27

Table 2.B-1 HPOTP Heat Exchanger Coil Beam-End Forces Near Weld 3

(a) BEAM-END FORCES FROM AERO LOADS

	P (lb)	M_x (in.-lb)	M_y (in.-lb)	M_z (in.-lb)	V_y (lb)	V_z (lb)
STATIC	0.000	0.000	– 0.072	0.000	0.000	0.000
DYNAMIC 1780 Hz	0.000	0.000	0.000	0.072	0.000	0.000

(b) BEAM-END FORCES FROM RANDOM VIBRATION ANALYSES

	P	M_x	M_y	M_z	V_y	V_z
X-DIR						
RMS VALUE	0.857	0.001	0.004	0.141	0.259	0.019
FREQUENCY (Hz)	236	634	424	386	740	358
Y-DIR						
RMS VALUE	0.621	0.004	0.009	0.355	0.627	0.016
FREQUENCY (Hz)	840	800	275	320	1040	1011
Z-DIR						
RMS VALUE	0.041	0.014	0.050	0.007	0.049	0.643
FREQUENCY (Hz)	1404	1018	1224	1336	1392	1394

(c) BEAM-END FORCES FROM FREQUENCY RESPONSE ANALYSES

FREQUENCY (Hz)	P	M_x	M_y	M_z	V_y	V_z
500	0.270	0.003	0.010	0.205	0.348	0.052
600	0.070	0.002	0.005	0.015	0.035	0.038
1000	0.126	0.003	0.007	0.024	0.127	0.035
1500	0.077	0.003	0.019	0.019	0.144	0.307
1800	0.024	0.0003	0.0002	0.003	0.035	0.0007
2000	0.074	0.0009	0.003	0.009	0.099	0.077

The R5 vibration environment [4] was employed for the RV and FR STARDYNE analyses performed by Rocketdyne. The HEX coil was primarily excited by the R5 zone G vibration environment. Analyses were performed for excitations applied along the X, Y, and Z directions. The RMS beam-end forces and the corresponding force velocities were extracted at node 27 from the RV analysis output. The RMS force magnitudes given in Table 2.B-1b are the averages of the RMS values from element numbers 25 and 26 on both sides of node 27. The expected frequency for each force component was calculated using the corresponding force velocity. The beam-end force amplitudes were extracted for node 27 from the FR analyses output. The forces given in Table 2.B-1c are the sum of the amplitudes from X, Y, and Z direction FR analyses.

For the HEX coil, a deterministic module, which was a variation of the module embedded in the simulation loops, was used to test the driver transformation and scan the circumference of the duct to find the worst stress position. The analysis for location of the worst stress position on the circumference was run with single cycle time histories—the amplitude of the random reference histories was three, and the amplitude for each sinusoidal reference history was one. Table 2.B-2 gives the outcome of the deterministic analysis for finding the critical location at the circumferential angle of 85° in the HEX coil.

2.B.4 Driver Characterization

The list of drivers for the HEX coil, their distributions, and ranges are given in Table 2.3-1. The rationale for assigning the distributions for these drivers was presented in Section 2.3.2. The information used to describe some of these distributions and the specification of the distribution parameters are given here.

2.B.4.1 Weld Offset

Weld offset measurements were available from ten coils at weld 3. Table 3-9 of [1] gives the serial numbers of the coils and the weld offsets in inches. This data was considered inadequate to assign a probability distribution and hence the weld offset was treated parametrically. The average percentage weld offset from the measurements of 6% was used here.

2.B.4.2 Wall Temperature and Internal Pressure

The ranges of temperatures and internal pressure obtained from an engine balance model were provided by Rocketdyne. These were the nominal, or mean, values of the temperatures and pressure for minimum and maximum flow conditions and they are given in Table 3-10 in [1]. For the PFA, the temperatures and pressure were characterized with hyperparametric Normal distributions. That is, the mean and standard deviation of the Normal distributions themselves were characterized by Uniform distributions whose endpoints correspond to the driver

Table 2.B-2 Scanning Circumference for Critical Angle Causing Minimum Life

ANGLE (deg)	LIFE (secs)
0	1.1195×10^4
40	9.3847×10^2
60	5.7924×10^2
70	5.1228×10^2
75	4.9427×10^2
80	4.8477×10^2
85	4.8318×10^2
90	4.8941×10^2
100	5.2740×10^2
120	7.6050×10^2
160	6.2194×10^3
200	8.0868×10^3
240	1.1815×10^3
280	1.042×10^3
320	5.1179×10^3

values given in Table 3-10 of [1] for the minimum and maximum flow conditions. The variations of the temperatures and pressure were correlated such that they assumed values that corresponded to the same flow condition; the correlation was specified implicitly in the PROCRK program.

2.B.4.3 Weld Offset Stress Concentration Accuracy Factors

The weld offset stress concentration is given by Equation 2-3, and the F_k factor in this equation was determined using finite element stress analyses of detailed models of the weld region as described in Section 3.A.2.3 of [1]. The F_k factors were determined to be functions of the radius to thickness ratio R/t. The offset stress concentration accuracy factor λ_{OFF} accounts for the uncertainty in the F_k vs. R/t curve and it is characterized by a Uniform distribution with end points of 0.9 and 1.1.

2.B.5 Materials Characterization

As described in Section 2.3.1.1 crack growth data was available for welded 316L at stress ratios of R = 0.16, 0.7, and 0.9. The data was generated from tests on Compact Tension (CT) specimens with a thickness of 0.340 in., a width of 1.750 in., and a starter notch of 0.435 in., and hence the validity of the data was in question, for use in the HEX coil with "short cracks" in a tube with only 0.0125 in. nominal wall thickness, especially in the threshold growth region of the data.

The crack growth rate data generated at 400°F was used for the HEX coil application. Decreasing K-gradient tests were used to obtain the low growth rate data and increasing K-gradient tests were used to generate data in the higher growth rate region. The crack growth rate data points are given in the input file CRKDAT in Section 2.C.1. The low growth rate data were used to fit the model given by Equation 2-10, which resulted in the following values for threshold stress intensity range model parameters: ΔK_{THo} = 4.03 ksi$\sqrt{\text{in.}}$, C_o = 1.07, and d = 0.163. The entire crack growth data set was employed to derive the parameters of the generalized Forman model which is given by Equation 2-7. This gave the following model parameters: $C = 1.139 \times 10^{-9}$, n = 1.900, m = 0.856, p = 0.478, and q = 0.988. The mean growth rate curves for three stress ratios are given in Figure 2.3-4.

2.B.6 Time History Definition

The time histories were generated as described in Section 2.1.4 of [1]. The frequencies f of the random and sinusoidal load components for the HEX coil are given in Table 2.B-1. If the highest frequency among the significant load components is f_{max}, then the number of points that will be generated is given by $N \cdot f_{max} \cdot T$, where T is the length of the history in seconds and N is the number of points within a single cycle of the highest frequency history. The length and the initiating random number seed for the reference time histories were decided based on the lives calculated with 21 random number seeds and lengths of T = 1.0, 2.0, 3.0, 4.0 seconds. The lives were calculated with nominal driver values and are given, for each value of T, in Table 2.B-3. The desired random number seed and history length are those which correspond to the life near the median life and the shortest value of T for which the calculated life is close to those for higher values of T. From Table 2.B-3 the chosen seed was 1475 and the optimum length was 1.0 sec.

2.B.7 Probability of Failure Curve Parameter Estimation

The steps required to carry out the probability of failure curve parameter estimation for this HEX example are given in Figure 2.B-2. This procedure was used to obtain the results discussed in Section 2.3.4. Only the calculations for the 0.005 in. initial crack size will be presented in this section.

Table 2.B-3 Lives for Different Random Number Seeds and History Lengths

SEED	$T = 1$	$T = 2$	$T = 3$	$T = 4$
175	1.7238×10^5	1.7468×10^5	1.7593×10^5	1.7688×10^5
275	1.7536×10^5	1.7285×10^5	1.7182×10^5	1.7244×10^5
375	1.6713×10^5	1.6331×10^5	1.6392×10^5	1.6361×10^5
475	1.6684×10^5	1.6644×10^5	1.6564×10^5	1.6830×10^5
575	1.6270×10^5	1.6420×10^5	1.6490×10^5	1.6421×10^5
675	1.6480×10^5	1.6656×10^5	1.6364×10^5	1.6414×10^5
775	1.6946×10^5	1.6702×10^5	1.6599×10^5	1.6528×10^5
875	1.6901×10^5	1.6930×10^5	1.6737×10^5	1.6796×10^5
975	1.6583×10^5	1.6629×10^5	1.6597×10^5	1.6563×10^5
1075	1.6557×10^5	1.6589×10^5	1.6896×10^5	1.7147×10^5
1175	1.6993×10^5	1.6993×10^5	1.6748×10^5	1.6566×10^5
1275	1.6736×10^5	1.6514×10^5	1.6697×10^5	1.6728×10^5
1375	1.6779×10^5	1.6535×10^5	1.6392×10^5	1.6491×10^5
1475	1.6605×10^5	1.6711×10^5	1.7050×10^5	1.7257×10^5
1575	1.6336×10^5	1.6262×10^5	1.6523×10^5	1.6497×10^5
1675	1.6124×10^5	1.6588×10^5	1.6828×10^5	1.6745×10^5
1775	1.6345×10^5	1.6853×10^5	1.6793×10^5	1.6960×10^5
1875	1.6243×10^5	1.6205×10^5	1.6578×10^5	1.6586×10^5
1975	1.6226×10^5	1.6383×10^5	1.6276×10^5	1.7193×10^5
2075	1.6443×10^5	1.7516×10^5	1.7160×10^5	1.7140×10^5
2175	1.6862×10^5	1.6740×10^5	1.6683×10^5	1.6478×10^5

The parameters of the prior distribution are estimated by determining a value for β, then estimating α and θ for fixed β. The first step in the procedure is to plot the failure simulation results contained in file LOWLIF for the "all drivers" run. That plot is shown in Figure 2.3-5. Since the all drivers run is nonlinear, the alternative procedure described in Section 2.3.9 of [1] was used. This run is called the "capability" run and was carried out by allowing variation in the crack shape, inner diameter, wall thickness, and offset accuracy factor. The other drivers were held at their nominal values.

1 Plot the failure simulation results contained in file LOWLIF in log–log space for both the "all driver" and "capability" runs.

2 Since the curve for the capability run from probability of .002 to .005, that is, point 20 to point 50 of file LOWLIF, is approximately linear, it can be used to estimate β.

3 Create file BFITD to indicate the indices of the LOWLIF data to be used in the β estimation. See Section 6.4.3.1 of [1] for a detailed description of the contents of file BFITD.

4 Run program BFIT. The pertinent methodology is discussed in Section 2.1.1 of [1]; the program description and flowcharts are presented in Section 4.2.2 of [1]; the user's guide for running this program is given in Sections 6.4.1–6.4.6 of [1]; and the code structure and listing are provided in Section 7.4.1 of [1]. BFIT has two input files, LOWLIF and BFITD, and two output files, BFITO and IOUTPR.

5 Obtain β estimate from output files BFITO and IOUTPR. Program BFIT has provided the estimate of 10.98.

6 In order for α and θ to be uniquely determined, it is only necessary to consider the range .002 to .01, that is, point 20 to point 100 inclusive, of file LOWLIF (for the all driver run), for the estimated curve to be nonlinear in log–log space. Create file PARAMS to indicate the indices of the LOWLIF data to be used in the α, θ estimation, the initial values for α and θ, and any scaling factors required. See Section 6.4.9.1 of [1] for a detailed description of the contents of file PARAMS.

7 Run program ABTFIT. The pertinent methodology is discussed in Section 2.1.1 of [1]; the program description and flowcharts are presented in Section 4.2.3 of [1]; the user's guide for running this program is given in Sections 6.4.7–6.4.12 of [1]; and the code structure and listing are provided in Section 7.4.2 of [1]. ABTFIT has two input files, LOWLIF and PARAMS, and three output files, ABTOUT, BAYESD and IOUTPR.

8 Obtain α, θ estimates from output files ABTOUT and BAYESD. Program ABTFIT has provided the values 2.68×10^{50} for θ and 4.022×10^{-3} for α.

9 Calculate assurance based on estimates of α, β, θ. The assurance calculation is performed by program LZERO. The pertinent methodology is discussed in Section 2.1.1 of [1]; the program description and flowcharts are presented in Section 4.2.4 of [1]; the user's guide for running this program is given in Sections 6.4.13–6.4.18 of [1]; and the code structure and listing are provided in Section 7.4.3 of [1].

Figure 2.B-2 Steps of the Probability of Failure Curve Parameter Estimation

The β estimate is based on an approximate linear portion of the left-hand tail (.002 to .005 on the ordinate) for this example. This probability range corresponds to simulated lives with index numbers 20 through 50, inclusive, in file LOWLIF. A value for β is estimated by program BFIT. The pertinent methodology is discussed in Section 2.1.1 of [1], the program description and flowcharts are presented in Section 4.2.2 of [1], the user's guide for running this program is given in Sections 6.4.1 through 6.4.6 of [1], and the code structure and listing are provided in Section 7.4.1 of [1]. Program BFIT has provided the estimate $\beta = 10.98$ for this example.

The α and θ estimate must be based on the all driver run in order to fit a model which is nonlinear in log–log space. It is only necessary to consider points with probability in the range .002 to .01. α, θ are estimated by program ABTFIT. The pertinent methodology is discussed in Section 2.1.1 of [1], the program description and flowcharts are presented in Section 4.2.3 of [1], the user's guide for running this program is given in Section 6.4.7 through 6.4.12 of [1], and the code structure and listing are provided in Section 7.4.2 of [1].

PARAMS requires initial values[1] for α and θ that were obtained as follows:

B.1[2] = 3.0076×10^4
B1 = 4.8558×10^4

LSCALE[3] = $\left(1 \,/\, 3.0076 \times 10^4\right) \approx 3 \times 10^{-5}$

$\theta_o = N_{.001}^{\beta} = \left(3.0076 \times 10^4\right)^{10.9787} = 1.4623 \times 10^{49}$

XGUESS(1)[4] = $\left(N_{.001} * \textbf{LSCALE}\right)^{\beta} = \left(3.0076 \times 10^4 \times 3 \times 10^{-5}\right)^{10.9787} = .323$

XGUESS(2) = $\alpha_o = -\ln .999 \,/\, \ln 2 = .0014434$

Program ABTFIT has provided the estimates $\theta = 2.6759 \times 10^{50}$ and $\alpha = 4.0227 \times 10^{-3}$. Table 2.B-4 gives the α, β, and θ values which define the left-hand tail of the

---

1 The calculation of initial values is illustrated in Section 6.4.11 of [1].

2 B-lives were obtained from file LOWLIF. A B-life is the value of the failure parameter (e.g., failure time) at a failure probability specified as a percent: e.g., B.1 is the failure time at a probability of .001 or .1%.

3 Life scaling factor is described in Section 6.4.9 of [1].

4 Calculation of initial guesses is described in Section 6.4.11 of [1].

Table 2.B-4 Probability of Failure Curve Parameter Estimates for Different Initial Crack Sizes

	Inital Crack Size a_i, in.			
	0.001 in.	0.0025 in.	0.005 in.	0.0075 in.
β	10.8485	11.0476	10.9787	4.20336
α	6.3531×10^{-3}	5.3007×10^{-3}	4.0227×10^{-3}	6.8452×10^{-3}
θ	1.9279×10^{55}	2.2648×10^{53}	2.6759×10^{50}	7.5838×10^{17}
λ_o for 95% Assurance	9.1242×10^{-60}	1.5619×10^{-58}	6.1037×10^{-57}	4.1468×10^{-22}

probability – life distribution for initial crack sizes of 0.001 in., 0.0025 in., 0.005 in., and 0.0075 in.

2.B.8 Driver Sensitivity Analysis

As described in Section 2.3.10 of [1], a set of simulations was executed to obtain the driver sensitivities. The first simulation was the nominal run in which all the drivers were fixed at their nominal or most likely values. Figure 2.3-5 shows the output of the nominal simulation for the HEX with a 0.005 in. initial crack size. The next simulation was the "all driver" variation run, which was performed by allowing all the drivers to vary. Figure 2.3-5 shows the output of the all-driver run for the HEX with a 0.005 in. initial crack size.

Finally, the driver sensitivities were derived using simulations for which each driver was allowed to vary one at a time while all the other drivers were held at their nominal values. Some related drivers, such as the flow parameters (inner and outer wall temperatures and internal pressure), must vary together for driver sensitivity analysis. The output from these simulations along with the results from the aforementioned all-driver variation and nominal runs allows the drivers to be rank ordered and allows their relative importance to be characterized. The impact of the drivers was calculated based on the failure lives at the .01 probability level, given in Table 2.B-5, for the all-driver, nominal, and driver sensitivity runs.

To calculate the relative importance of a driver, the change in life from the nominal analysis due to driver variation was first calculated as a percentage of the shift due to the all-driver variation, for each driver. The largest shift was caused by variation in the crack shape, which is therefore the most important driver. The relative importance was derived by normalizing the percentage shifts due to variation of each driver with the percentage shift due to variation of the most important driver, in this case the crack shape. Table 2.B-5 gives the percentage shift in lives and the relative importance for each driver.

Table 2.B-5 Driver Sensitivity Analysis for 0.005 in. Initial Crack Size

DRIVER VARIATION IN ANALYSIS	B1 LIFE (seconds)	SHIFT FROM NOMINAL VALUE	% SHIFT FROM ALL DRIVERS CURVE	RELATIVE IMPORTANCE
NOMINAL	2.2035×10^5			
ALL DRIVERS	4.8558×10^4	1.71792×10^5		
a / c	9.8132×10^4	1.22218×10^5	71.1	100
λ_{gro}	1.1161×10^5	1.0874×10^5	63.3	89
$\lambda_{DRANDOM} + \lambda_{DSINUSOIDAL}$	1.4930×10^5	7.1050×10^4	41.4	58
λ_{OFF}	1.6354×10^5	5.6810×10^4	33.1	47
$\lambda_{DYNstr} + \lambda_{STstr}$	1.7330×10^5	4.7050×10^4	27.4	39
λ_{sif}	1.7588×10^5	4.4470×10^4	25.9	36
$\lambda_{AEROST} + \lambda_{AERODYN}$	1.7849×10^5	4.1860×10^4	24.4	34
$T_i + T_o + P_i$	1.9324×10^5	2.7110×10^4	15.8	22
t	1.9472×10^5	2.5630×10^4	14.9	21
λ_{neu}	2.1482×10^5	5.530×10^3	3.2	5
D_i	2.1773×10^5	2.620×10^3	1.5	2

2.B.9 Probability of Failure Curve Standardization

In order to standardize the results, the probability of failure vs. life curves were generated for a given assurance level of 95% by using the program LZERO. The pertinent methodology is discussed in Section 2.1.1 of [1], the program description and flowcharts are presented in Section 4.2.4 of [1], the user's guide for running this program is given in Sections 6.4.13 through 6.4.18 of [1], and the code structure and listing are provided in Section 7.4.3 of [1]. The values of λ_o for 0.001 in., 0.0025 in., 0.005 in., and 0.0075 in. initial crack sizes are given in Table 2.B-4. Given λ_o and the bounding value of β, the assurance curve may be defined as described in Section 2.3.12 of [1]. The 95% assurance curves for the four initial crack sizes are given in Figure 2.3-6.

Appendix 2.C
Input And Output Files

2.C.1 HPOTP Heat Exchanger Coil Analysis Files

Selected input and output files for the HPOTP heat exchanger coil "all driver" analysis are given here. The analysis program PROCRK requires the input file CRKDAT along with the force history files. Annotated examples of the data file format for CRKDAT are given in Figure 6.1-1. The input file CRKDAT is given below. Section 6.1.3.1 contains a description of the input variables and a user's guide for running PROCRK.

The output files from a PROCRK run are CRKRES, LOWLIF, and IOUTPR. The CRKRES and LOWLIF from an "all drivers" analysis of the HEX coil are given below. The CRKRES file contains an echo of the input data, output from the crack growth model regression, and the B-lives. The LOWLIF file contains the lowest 100 (1% of total simulated) crack growth failure lives for the HEX coil; these failure lives are plotted in Figure 2.3-5.

Input File - CRKDAT

```
1
1
675
0
1
10000
1
1
5
0.0001   0.0005   0.001   0.005   0.01
0.06      0.06      0.00    0.00     0.0    0.0
0.00      0.00      0.00    0.00     0.0    0.0
1.00
0.1885    0.1915    0.50      0.50      0.5    20.
0.0113    0.0157    0.27273   0.27273   0.5    20.
0.200    1.000    0.50    0.50    0.0    0.0
0.005    0.005    0.00    0.00    0.0    0.0
2.00      2.00      0.15    1.00
2.00      2.00      0.20    1.00
 486.     666.     29.     56.5
 799.     908.     49.5    48.
3808.    4177.     69.     69.
```

```
0.80    1.20
0.50    1.50
0.80    1.20
0.90    1.10
0.80    1.20
0.60    1.40
0.00    0.00
1.00    1.00
0.90    1.10
-0.6931    0.557
16
0.00      0.00      -0.07214    0.00       0.00       0.00
'XP'     1   0.856685 0.00       0.00       0.00       0.00       0.00
'YP'     1   0.620780 0.00       0.00       0.00       0.00       0.00
'ZP'     1   0.041151 0.00       0.00       0.00       0.00       0.00
'XM2'    1   0.00     0.00       0.004000   0.00       0.00       0.00
'YM2'    1   0.00     0.00       0.009390   0.00       0.00       0.00
'ZM2'    1   0.00     0.00       0.050300   0.00       0.00       0.00
'XM3'    1   0.00     0.00       0.00       0.141020   0.00       0.00
'YM3'    1   0.00     0.00       0.00       0.355475   0.00       0.00
'ZM3'    1   0.00     0.00       0.00       0.007480   0.00       0.00
'SIN1'   2   0.269884 0.003040   0.009640   0.205000   0.348000   0.05160
'SIN2'   2   0.069594 0.001740   0.005010   0.014900   0.034800   0.03790
'SIN3'   2   0.125976 0.003210   0.007200   0.024200   0.127000   0.03500
'SIN4'   2   0.076991 0.003310   0.019400   0.018700   0.144000   0.30700
'SIN5'   2   0.023680 0.000325   0.000179   0.002890   0.034700   0.00069
'SIN6'   2   0.074108 0.000946   0.003270   0.009340   0.099100   0.07690
'AERO'   3   0.00     0.00       0.00       0.07179    0.00       0.00
3640.
2
85.
2.30
1.0
0.0
20000
29000000.    8.8E-06    0.30
0.235      2.00
0.300      4.80
0.350      7.20
0.400      9.60
0.450     12.50
0.500     15.80
0.550     20.00
0.580     24.00
0.600     30.00
0.600    200.00
6
   21.95    0.001
   55.77    0.002
  144.85    0.005
```

```
  322.73    0.010
 1945.90    0.050
50688.0     0.660
'400F 316L WELDED, FROM Rkd'
27000  80.0  8  4
4.0317  1.070  0.16327
39  0.90
2.446E-10  2.53
5.568E-10  2.56
1.115E-9  2.61
2.913E-9  2.66
4.460E-9  2.64
9.765E-9  2.70
1.224E-8  2.76
1.452E-8  2.82
2.146E-8  2.88
3.468E-8  2.94
5.660E-8  3.00
6.879E-8  3.06
7.226E-8  3.12
6.625E-8  3.18
5.230E-8  3.24
4.720E-8  3.30
4.886E-8  3.37
4.904E-8  3.44
4.827E-8  3.51
5.806E-8  3.58
6.929E-8  3.65
6.903E-8  3.73
6.752E-8  3.80
6.674E-8  3.87
6.513E-8  3.96
8.996E-8  4.09
1.277E-7  4.23
1.398E-7  4.41
1.382E-7  4.58
1.694E-7  4.78
1.894E-7  4.95
1.887E-7  5.16
2.305E-7  5.36
2.984E-7  5.57
4.530E-7  5.80
7.381E-7  6.02
1.267E-6  6.31
2.514E-6  6.60
8.049E-6  7.19
38  0.90
9.183E-10  2.56
1.374E-9  2.60
2.950E-9  2.62
```

```
1.006E-8  2.66
1.138E-8  2.69
1.183E-8  2.72
1.247E-8  2.75
2.835E-9  2.59
6.084E-9  2.65
1.530E-8  2.74
3.362E-8  2.82
6.708E-8  2.91
8.473E-8  3.00
7.658E-8  3.08
6.251E-8  3.16
5.100E-8  3.24
4.408E-8  3.33
4.807E-8  3.43
5.838E-8  3.53
5.787E-8  3.63
5.679E-8  3.74
6.307E-8  3.84
7.220E-8  3.95
8.042E-8  4.07
8.202E-8  4.18
7.896E-8  4.30
7.440E-8  4.42
7.603E-8  4.54
9.028E-8  4.67
1.019E-7  4.80
1.133E-7  4.94
1.378E-7  5.08
1.533E-7  5.22
1.543E-7  5.36
1.629E-7  5.51
1.734E-7  5.66
1.727E-7  5.81
2.321E-7  5.99
64  0.70
2.330E-9  3.46
9.799E-9  3.50
2.562E-8  3.57
3.132E-8  3.64
3.112E-8  3.72
3.319E-8  3.79
3.333E-8  3.87
3.621E-8  3.95
4.207E-8  4.05
4.017E-8  4.11
3.923E-8  4.21
4.155E-8  4.28
4.497E-8  4.38
5.670E-8  4.47
```

6.300E-8	4.56
6.466E-8	4.65
6.798E-8	4.75
7.103E-8	4.85
7.335E-8	4.95
7.690E-8	5.05
8.277E-8	5.16
8.703E-8	5.26
8.951E-8	5.37
9.151E-8	5.49
8.674E-8	5.61
8.323E-8	5.73
9.206E-8	5.85
1.040E-7	5.97
1.501E-8	3.49
2.321E-8	3.66
4.565E-8	3.83
7.893E-8	4.00
7.586E-8	4.18
7.386E-8	4.36
8.960E-8	4.53
9.996E-8	4.72
1.064E-7	4.92
1.216E-7	5.13
1.300E-7	5.36
1.517E-7	5.61
1.698E-7	5.84
1.559E-7	6.10
1.607E-7	6.36
1.732E-7	6.62
1.903E-7	6.91
2.152E-7	7.20
2.560E-7	7.52
2.930E-7	7.84
3.197E-7	8.18
3.833E-7	8.53
4.219E-7	8.89
4.190E-7	9.27
4.288E-7	9.66
4.699E-7	10.07
5.430E-7	10.49
6.424E-7	10.95
7.510E-7	11.41
9.050E-7	11.92
1.027E-6	12.41
1.088E-6	12.94
1.268E-6	13.49
1.351E-6	14.04
1.389E-6	14.65
1.530E-6	15.25

```
 70  0.70
 9.676E-10  3.45
 4.535E-9  3.48
 1.616E-8  3.56
 2.225E-8  3.63
 2.960E-8  3.70
 3.208E-8  3.77
 3.158E-8  3.85
 3.917E-8  3.93
 4.525E-8  4.01
 4.366E-8  4.09
 4.370E-8  4.17
 4.884E-8  4.26
 5.192E-8  4.35
 5.530E-8  4.44
 6.224E-8  4.53
 6.708E-8  4.62
 7.141E-8  4.71
 7.335E-8  4.81
 7.289E-8  4.91
 7.304E-8  5.02
 7.340E-8  5.12
 7.039E-8  5.22
 7.575E-8  5.34
 8.416E-8  5.44
 8.978E-8  5.56
 9.889E-8  5.68
 9.942E-8  5.80
 9.637E-8  5.92
 4.661E-9  3.58
 9.538E-9  3.68
 2.469E-8  3.80
 3.830E-8  3.95
 7.246E-8  4.12
 1.180E-7  4.32
 1.387E-7  4.49
 1.224E-7  4.70
 1.162E-7  4.88
 1.419E-7  5.08
 1.631E-7  5.28
 1.492E-7  5.51
 1.539E-7  5.74
 1.585E-7  5.98
 1.562E-7  6.24
 1.645E-7  6.50
 1.839E-7  6.77
 1.783E-7  7.03
 2.089E-7  7.35
 2.881E-7  7.64
 3.497E-7  7.99
```

```
 3.640E-7   8.32
 2.936E-7   8.65
 2.630E-7   9.00
 2.949E-7   9.37
 3.418E-7   9.75
 3.848E-7  10.15
 4.242E-7  10.57
 4.819E-7  11.01
 5.694E-7  11.45
 6.968E-7  11.91
 8.182E-7  12.38
 8.980E-7  12.87
 1.019E-6  13.37
 1.111E-6  13.89
 1.201E-6  14.45
 1.380E-6  15.00
 1.553E-6  15.60
 1.804E-6  16.22
 2.205E-6  16.82
 2.790E-6  17.49
 3.901E-6  18.17
66   0.16
 1.775E-7   9.10
 1.857E-7   9.29
 1.847E-7   9.50
 1.955E-7   9.70
 1.969E-7   9.91
 2.072E-7  10.13
 2.199E-7  10.34
 2.241E-7  10.57
 2.454E-7  10.79
 2.534E-7  11.03
 2.423E-7  11.27
 2.382E-7  11.52
 2.543E-7  11.78
 2.776E-7  12.03
 3.073E-7  12.30
 3.535E-7  12.55
 4.050E-7  12.83
 4.535E-7  13.10
 4.697E-7  13.37
 5.007E-7  13.68
 5.355E-7  13.96
 5.107E-7  14.25
 5.483E-7  14.58
 6.766E-7  14.88
 7.369E-7  15.20
 7.901E-7  15.54
 8.893E-7  15.85
 9.689E-7  16.20
```

```
1.058E-6  16.53
1.163E-6  16.88
1.464E-6  17.25
1.752E-6  17.59
2.008E-6  18.00
2.116E-6  18.35
2.003E-6  18.76
2.246E-6  19.15
2.650E-6  19.56
3.047E-6  19.98
3.698E-6  20.40
4.175E-6  20.83
4.238E-6  21.24
4.486E-6  21.71
4.876E-6  22.15
5.194E-6  22.63
5.679E-6  23.11
6.518E-6  23.58
7.327E-6  24.07
8.302E-6  24.57
8.308E-6  25.07
8.564E-6  25.59
9.132E-6  26.11
9.010E-6  26.65
9.687E-6  27.33
1.085E-5  28.18
1.172E-5  29.18
1.293E-5  30.40
1.493E-5  31.61
1.649E-5  32.96
1.773E-5  34.26
1.935E-5  35.67
2.178E-5  37.08
2.335E-5  38.56
2.616E-5  40.12
2.863E-5  41.71
2.963E-5  43.34
3.304E-5  45.07
42  0.16
2.122E-8  3.99
3.204E-8  4.08
3.169E-8  4.17
3.095E-8  4.27
3.366E-8  4.36
4.457E-8  4.47
4.677E-8  4.56
4.259E-8  4.67
4.540E-8  4.77
4.413E-8  4.88
4.354E-8  4.99
```

```
 4.579E-8  5.10
 4.958E-8  5.22
 5.564E-8  5.34
 5.773E-8  5.45
 6.046E-8  5.58
 6.388E-8  5.70
 6.303E-8  5.84
 6.063E-8  5.96
 5.612E-8  6.10
 5.512E-8  6.23
 8.505E-8  6.37
 6.466E-8  6.52
 5.077E-8  6.67
 7.039E-8  6.82
 7.186E-8  6.97
 7.511E-8  7.13
 8.152E-8  7.28
 8.613E-8  7.44
 9.279E-8  7.61
 9.644E-8  7.78
 9.540E-8  7.95
 1.021E-7  8.14
 1.152E-7  8.32
 1.224E-7  8.50
 3.212E-8  4.35
 5.321E-8  4.55
 9.616E-8  4.74
 1.433E-7  4.97
 1.611E-7  5.18
 1.701E-7  5.41
 1.944E-7  5.63
92   0.16
 2.462E-9  3.94
 8.454E-9  4.00
 1.084E-8  4.07
 1.024E-8  4.15
 1.092E-8  4.23
 1.201E-8  4.31
 1.283E-8  4.38
 1.738E-8  4.47
 2.292E-8  4.55
 2.511E-8  4.63
 2.747E-8  4.72
 3.153E-8  4.80
 3.652E-8  4.89
 3.924E-8  4.98
 4.126E-8  5.07
 4.061E-8  5.16
 3.903E-8  5.26
 4.231E-8  5.35
```

5.293E-8	5.45
6.007E-8	5.55
6.032E-8	5.65
6.260E-8	5.75
6.590E-8	5.85
7.010E-8	5.96
7.227E-8	6.07
7.489E-8	6.18
7.383E-8	6.29
6.902E-8	6.41
7.069E-8	6.52
7.956E-8	6.64
8.426E-8	6.76
7.979E-8	6.88
7.867E-8	7.00
8.313E-8	7.13
8.994E-8	7.25
9.403E-8	7.38
9.391E-8	7.52
9.783E-8	7.65
1.056E-7	7.79
1.032E-7	7.93
9.733E-8	8.08
9.633E-8	8.22
9.990E-8	8.37
1.079E-7	8.52
1.155E-7	8.67
1.210E-8	4.40
1.574E-8	4.57
3.055E-8	4.77
6.529E-8	4.99
8.832E-8	5.22
9.955E-8	5.45
1.046E-7	5.68
1.013E-7	5.92
1.023E-7	6.17
1.117E-7	6.43
1.247E-7	6.71
1.361E-7	7.00
1.468E-7	7.32
1.528E-7	7.63
1.576E-7	7.95
1.634E-7	8.29
1.753E-7	8.65
1.882E-7	9.02
1.996E-7	9.42
2.158E-7	9.82
2.252E-7	10.24
2.455E-7	10.68
2.742E-7	11.13

```
3.017E-7  11.60
3.563E-7  12.10
4.273E-7  12.60
4.916E-7  13.14
5.613E-7  13.69
6.961E-7  14.30
8.600E-7  14.89
9.727E-7  15.52
1.227E-6  16.18
1.573E-6  16.85
1.903E-6  17.57
2.538E-6  18.32
3.363E-6  19.09
3.763E-6  19.82
4.324E-6  20.66
4.842E-6  21.47
5.167E-6  22.37
5.859E-6  23.30
7.262E-6  24.27
8.478E-6  25.23
9.053E-6  26.30
9.442E-6  27.35
1.046E-5  28.49
1.122E-5  29.67
79  0.16
1.825E-9  4.48
1.241E-8  4.57
1.910E-8  4.68
2.544E-8  4.78
3.081E-8  4.89
3.331E-8  5.00
3.428E-8  5.11
3.632E-8  5.23
3.502E-8  5.34
3.939E-8  5.47
4.942E-8  5.59
5.201E-8  5.71
5.026E-8  5.84
4.848E-8  5.97
5.131E-8  6.10
5.305E-8  6.25
5.463E-8  6.39
5.491E-8  6.54
5.579E-8  6.68
6.352E-8  6.83
6.847E-8  6.98
7.381E-8  7.13
7.999E-8  7.29
7.965E-8  7.46
8.777E-8  7.63
```

9.269E-8	7.80
8.880E-8	7.97
1.041E-7	8.16
1.114E-7	8.33
1.041E-7	8.52
1.378E-8	4.88
4.458E-8	5.04
9.903E-8	5.26
1.491E-7	5.46
1.834E-7	5.65
2.372E-7	5.85
2.564E-7	6.04
2.222E-7	6.23
1.866E-7	6.44
1.689E-7	6.64
1.586E-7	6.84
1.652E-7	7.08
1.784E-7	7.31
1.804E-7	7.56
2.080E-7	7.82
2.556E-7	8.10
2.301E-7	8.37
2.013E-7	8.66
2.438E-7	8.97
2.570E-7	9.25
2.482E-7	9.61
2.568E-7	9.90
2.900E-7	10.26
3.551E-7	10.60
3.587E-7	10.96
3.928E-7	11.34
4.457E-7	11.71
4.539E-7	12.11
5.313E-7	12.53
6.756E-7	12.94
7.735E-7	13.38
8.485E-7	13.83
9.304E-7	14.31
1.030E-6	14.81
1.202E-6	15.31
1.572E-6	15.85
1.965E-6	16.39
2.112E-6	16.94
2.491E-6	17.50
3.067E-6	18.07
3.326E-6	18.62
3.515E-6	19.26
3.877E-6	19.86
4.332E-6	20.52
5.239E-6	21.23

```
6.519E-6  21.98
7.768E-6  22.68
8.908E-6  23.43
9.110E-6  24.21
```

Output File - CRKRES

P R O C R K

INPUT DATA

LIFE DRIVERS		PARAMETERS RHO	THETA
WELD OFFSET (%)	B(0.06, 0.06) B(0.00, 0.00) TEST = 1.00	(0.00000, 0.00000) (0.00000, 0.00000)	(0.0, 0.0) (0.0, 0.0)
INNER DIAMETER	B(0.1885, 0.1915)	(0.50000, 0.50000)	(0.5, 20.0)
WALL THICKNESS	B(0.0113, 0.0157)	(0.27273, 0.27273)	(0.5, 20.0)
CRACK SHAPE A/C	B(0.2000, 1.0000)	(0.50000, 0.50000)	(0.0, 0.0)
CRACK SIZE A	B(0.0050, 0.0050)	(0.00000, 0.00000)	(0.0, 0.0)
LAMBDA RANDOM	k: U(2.00000, 2.00000) COEFFICIENT OF VARIATION: 0.150 STRAIN GAGE FACTOR: 1.0000000		
LAMBDA SINE	k: U(2.00000, 2.00000) COEFFICIENT OF VARIATION: 0.200 STRAIN GAGE FACTOR: 1.0000000		
INNER TEMPERATURE	NORMAL: MU(486.0, 666.0)	SIGMA(29.0, 56.5)	
OUTER TEMPERATURE	NORMAL: MU(799.0, 908.0)	SIGMA(49.5, 48.0)	
INNER PRESSURE	NORMAL: MU(3808.0, 4177.0)	SIGMA(69.0, 69.0)	

WELD OFFSET K FAC	U(0.80000, 1.20000)
DYN AERO LOAD FAC	U(0.50000, 1.50000)
STAT AERO LOAD FAC	U(0.80000, 1.20000)
AERO STR ANAL FAC	U(0.90000, 1.10000)
DYN STR ANAL FAC	U(0.80000, 1.20000)
NEUBERS RULE	U(0.60000, 1.40000)
LAMBDA Kth	U(0.00000, 0.00000)
LAMBDA Kc	U(1.00000, 1.00000)
K CALC FAC	U(0.90000, 1.10000)
GROWTH CALC FAC	U(-0.69310, 0.55700)

LOADS INPUT

P LOADS	T LOADS	M2 LOADS	M3 LOADS	V2 LOADS	V3 LOADS
STATIC AERO					
0.000000	0.000E+00	-.721E-01	0.000E+00	0.000E+00	0.000E+00
XP					
0.856685	0.000E+00	0.000E+00	0.000E+00	0.000E+00	0.000E+00
YP					
0.620780	0.000E+00	0.000E+00	0.000E+00	0.000E+00	0.000E+00
ZP					
0.041151	0.000E+00	0.000E+00	0.000E+00	0.000E+00	0.000E+00
XM2					
0.000000	0.000E+00	0.400E-02	0.000E+00	0.000E+00	0.000E+00
YM2					
0.000000	0.000E+00	0.939E-02	0.000E+00	0.000E+00	0.000E+00
ZM2					
0.000000	0.000E+00	0.503E-01	0.000E+00	0.000E+00	0.000E+00
XM3					
0.000000	0.000E+00	0.000E+00	0.141E+00	0.000E+00	0.000E+00
YM3					
0.000000	0.000E+00	0.000E+00	0.355E+00	0.000E+00	0.000E+00
ZM3					
0.000000	0.000E+00	0.000E+00	0.748E-02	0.000E+00	0.000E+00
SIN1					

0.269884	0.304E-02	0.964E-02	0.205E+00	0.348E+00	0.516E-01
SIN2					
0.069594	0.174E-02	0.501E-02	0.149E-01	0.348E-01	0.379E-01
SIN3					
0.125976	0.321E-02	0.720E-02	0.242E-01	0.127E+00	0.350E-01
SIN4					
0.076991	0.331E-02	0.194E-01	0.187E-01	0.144E+00	0.307E+00
SIN5					
0.023680	0.325E-03	0.179E-03	0.289E-02	0.347E-01	0.690E-03
SIN6					
0.074108	0.946E-03	0.327E-02	0.934E-02	0.991E-01	0.769E-01
AERO					
0.000000	0.000E+00	0.000E+00	0.718E-01	0.000E+00	0.000E+00

MISCELLANEOUS INPUT

EXTERNAL PRESSURE	3640.
ANALYSIS LOCATION	2
ANGLE THETA (DEGREES)	85.0
WILLENBORG OVERLOAD FACTOR	0.23000E+01
STRESS-TIME HISTORY PERIOD	1.00000
STRESS-TIME HISTORY NOISE FILTER	0.0
NUMBER OF TIME-VARYING LOADS	16
NUMBER OF POINTS IN HISTORIES	20000

ELASTIC MODULUS	0.290E+08
COEFF OF THERMAL EXPANSION	0.87999997E-05
POISSONS RATIO	0.300

Fk VS. Rt CURVE INPUT

Fk	Rt

0.23	2.00
0.30	4.80
0.35	7.20
0.40	9.60
0.45	12.50
0.50	15.80
0.55	20.00
0.58	24.00
0.60	30.00
0.60	200.00

STRESS-STRAIN CURVE INPUT

MAXIMUM NUMBER OF SEGMENTS 6

STRESS-STRAIN PRODUCT	STRAIN VALUES
21.95	0.00100
55.77	0.00200
144.85	0.00500
322.73	0.01000
1945.90	0.05000
50688.00	0.66000

MATERIAL INPUT

DESCRIPTION: 400F 316L WELDED, FROM Rkd

YIELD STRENGTH 27000.

CRITICAL S I F 80.

NUMBER OF DIVISIONS 8

REGRESSION OPTION 4

THRESHOLD MODEL DESCRIPTION

DKTHo = 0.40317E+01
Co = 0.10700E+01
d = 0.16327E+00

STRESS RATIO R = 0.90

da/dN	DELK
0.24460E-09	0.25300E+01
0.55680E-09	0.25600E+01
0.11150E-08	0.26100E+01
0.29130E-08	0.26600E+01
0.44600E-08	0.26400E+01
0.97650E-08	0.27000E+01
0.12240E-07	0.27600E+01
0.14520E-07	0.28200E+01
0.21460E-07	0.28800E+01
0.34680E-07	0.29400E+01
0.56600E-07	0.30000E+01
0.68790E-07	0.30600E+01
0.72260E-07	0.31200E+01
0.66250E-07	0.31800E+01
0.52300E-07	0.32400E+01
0.47200E-07	0.33000E+01
0.48860E-07	0.33700E+01
0.49040E-07	0.34400E+01
0.48270E-07	0.35100E+01
0.58060E-07	0.35800E+01
0.69290E-07	0.36500E+01
0.69030E-07	0.37300E+01
0.67520E-07	0.38000E+01
0.66740E-07	0.38700E+01
0.65130E-07	0.39600E+01
0.89960E-07	0.40900E+01
0.12770E-06	0.42300E+01
0.13980E-06	0.44100E+01
0.13820E-06	0.45800E+01
0.16940E-06	0.47800E+01

0.18940E-06	0.49500E+01
0.18870E-06	0.51600E+01
0.23050E-06	0.53600E+01
0.29840E-06	0.55700E+01
0.45300E-06	0.58000E+01
0.73810E-06	0.60200E+01
0.12670E-05	0.63100E+01
0.25140E-05	0.66000E+01
0.80490E-05	0.71900E+01

STRESS RATIO R = 0.90

da/dN	DELK
0.91830E-09	0.25600E+01
0.13740E-08	0.26000E+01
0.29500E-08	0.26200E+01
0.10060E-07	0.26600E+01
0.11380E-07	0.26900E+01
0.11830E-07	0.27200E+01
0.12470E-07	0.27500E+01
0.28350E-08	0.25900E+01
0.60840E-08	0.26500E+01
0.15300E-07	0.27400E+01
0.33620E-07	0.28200E+01
0.67080E-07	0.29100E+01
0.84730E-07	0.30000E+01
0.76580E-07	0.30800E+01
0.62510E-07	0.31600E+01
0.51000E-07	0.32400E+01
0.44080E-07	0.33300E+01
0.48070E-07	0.34300E+01
0.58380E-07	0.35300E+01
0.57870E-07	0.36300E+01
0.56790E-07	0.37400E+01
0.63070E-07	0.38400E+01
0.72200E-07	0.39500E+01
0.80420E-07	0.40700E+01
0.82020E-07	0.41800E+01
0.78960E-07	0.43000E+01
0.74400E-07	0.44200E+01
0.76030E-07	0.45400E+01
0.90280E-07	0.46700E+01
0.10190E-06	0.48000E+01
0.11330E-06	0.49400E+01
0.13780E-06	0.50800E+01
0.15330E-06	0.52200E+01
0.15430E-06	0.53600E+01
0.16290E-06	0.55100E+01
0.17340E-06	0.56600E+01

0.17270E-06	0.58100E+01
0.23210E-06	0.59900E+01

STRESS RATIO R = 0.70

da/dN	DELK
0.23300E-08	0.34600E+01
0.97990E-08	0.35000E+01
0.25620E-07	0.35700E+01
0.31320E-07	0.36400E+01
0.31120E-07	0.37200E+01
0.33190E-07	0.37900E+01
0.33330E-07	0.38700E+01
0.36210E-07	0.39500E+01
0.42070E-07	0.40500E+01
0.40170E-07	0.41100E+01
0.39230E-07	0.42100E+01
0.41550E-07	0.42800E+01
0.44970E-07	0.43800E+01
0.56700E-07	0.44700E+01
0.63000E-07	0.45600E+01
0.64660E-07	0.46500E+01
0.67980E-07	0.47500E+01
0.71030E-07	0.48500E+01
0.73350E-07	0.49500E+01
0.76900E-07	0.50500E+01
0.82770E-07	0.51600E+01
0.87030E-07	0.52600E+01
0.89510E-07	0.53700E+01
0.91510E-07	0.54900E+01
0.86740E-07	0.56100E+01
0.83230E-07	0.57300E+01
0.92060E-07	0.58500E+01
0.10400E-06	0.59700E+01
0.15010E-07	0.34900E+01
0.23210E-07	0.36600E+01
0.45650E-07	0.38300E+01
0.78930E-07	0.40000E+01
0.75860E-07	0.41800E+01
0.73860E-07	0.43600E+01
0.89600E-07	0.45300E+01
0.99960E-07	0.47200E+01
0.10640E-06	0.49200E+01
0.12160E-06	0.51300E+01
0.13000E-06	0.53600E+01
0.15170E-06	0.56100E+01
0.16980E-06	0.58400E+01
0.15590E-06	0.61000E+01
0.16070E-06	0.63600E+01

0.17320E-06	0.66200E+01
0.19030E-06	0.69100E+01
0.21520E-06	0.72000E+01
0.25600E-06	0.75200E+01
0.29300E-06	0.78400E+01
0.31970E-06	0.81800E+01
0.38330E-06	0.85300E+01
0.42190E-06	0.88900E+01
0.41900E-06	0.92700E+01
0.42880E-06	0.96600E+01
0.46990E-06	0.10070E+02
0.54300E-06	0.10490E+02
0.64240E-06	0.10950E+02
0.75100E-06	0.11410E+02
0.90500E-06	0.11920E+02
0.10270E-05	0.12410E+02
0.10880E-05	0.12940E+02
0.12680E-05	0.13490E+02
0.13510E-05	0.14040E+02
0.13890E-05	0.14650E+02
0.15300E-05	0.15250E+02

STRESS RATIO R = 0.70

da/dN	DELK
0.96760E-09	0.34500E+01
0.45350E-08	0.34800E+01
0.16160E-07	0.35600E+01
0.22250E-07	0.36300E+01
0.29600E-07	0.37000E+01
0.32080E-07	0.37700E+01
0.31580E-07	0.38500E+01
0.39170E-07	0.39300E+01
0.45250E-07	0.40100E+01
0.43660E-07	0.40900E+01
0.43700E-07	0.41700E+01
0.48840E-07	0.42600E+01
0.51920E-07	0.43500E+01
0.55300E-07	0.44400E+01
0.62240E-07	0.45300E+01
0.67080E-07	0.46200E+01
0.71410E-07	0.47100E+01
0.73350E-07	0.48100E+01
0.72890E-07	0.49100E+01
0.73040E-07	0.50200E+01
0.73400E-07	0.51200E+01
0.70390E-07	0.52200E+01
0.75750E-07	0.53400E+01
0.84160E-07	0.54400E+01

0.89780E-07	0.55600E+01
0.98890E-07	0.56800E+01
0.99420E-07	0.58000E+01
0.96370E-07	0.59200E+01
0.46610E-08	0.35800E+01
0.95380E-08	0.36800E+01
0.24690E-07	0.38000E+01
0.38300E-07	0.39500E+01
0.72460E-07	0.41200E+01
0.11800E-06	0.43200E+01
0.13870E-06	0.44900E+01
0.12240E-06	0.47000E+01
0.11620E-06	0.48800E+01
0.14190E-06	0.50800E+01
0.16310E-06	0.52800E+01
0.14920E-06	0.55100E+01
0.15390E-06	0.57400E+01
0.15850E-06	0.59800E+01
0.15620E-06	0.62400E+01
0.16450E-06	0.65000E+01
0.18390E-06	0.67700E+01
0.17830E-06	0.70300E+01
0.20890E-06	0.73500E+01
0.28810E-06	0.76400E+01
0.34970E-06	0.79900E+01
0.36400E-06	0.83200E+01
0.29360E-06	0.86500E+01
0.26300E-06	0.90000E+01
0.29490E-06	0.93700E+01
0.34180E-06	0.97500E+01
0.38480E-06	0.10150E+02
0.42420E-06	0.10570E+02
0.48190E-06	0.11010E+02
0.56940E-06	0.11450E+02
0.69680E-06	0.11910E+02
0.81820E-06	0.12380E+02
0.89800E-06	0.12870E+02
0.10190E-05	0.13370E+02
0.11110E-05	0.13890E+02
0.12010E-05	0.14450E+02
0.13800E-05	0.15000E+02
0.15530E-05	0.15600E+02
0.18040E-05	0.16220E+02
0.22050E-05	0.16820E+02
0.27900E-05	0.17490E+02
0.39010E-05	0.18170E+02

STRESS RATIO R = 0.16

da/dN	DELK
0.17750E-06	0.91000E+01
0.18570E-06	0.92900E+01
0.18470E-06	0.95000E+01
0.19550E-06	0.97000E+01
0.19690E-06	0.99100E+01
0.20720E-06	0.10130E+02
0.21990E-06	0.10340E+02
0.22410E-06	0.10570E+02
0.24540E-06	0.10790E+02
0.25340E-06	0.11030E+02
0.24230E-06	0.11270E+02
0.23820E-06	0.11520E+02
0.25430E-06	0.11780E+02
0.27760E-06	0.12030E+02
0.30730E-06	0.12300E+02
0.35350E-06	0.12550E+02
0.40500E-06	0.12830E+02
0.45350E-06	0.13100E+02
0.46970E-06	0.13370E+02
0.50070E-06	0.13680E+02
0.53550E-06	0.13960E+02
0.51070E-06	0.14250E+02
0.54830E-06	0.14580E+02
0.67660E-06	0.14880E+02
0.73690E-06	0.15200E+02
0.79010E-06	0.15540E+02
0.88930E-06	0.15850E+02
0.96890E-06	0.16200E+02
0.10580E-05	0.16530E+02
0.11630E-05	0.16880E+02
0.14640E-05	0.17250E+02
0.17520E-05	0.17590E+02
0.20080E-05	0.18000E+02
0.21160E-05	0.18350E+02
0.20030E-05	0.18760E+02
0.22460E-05	0.19150E+02
0.26500E-05	0.19560E+02
0.30470E-05	0.19980E+02
0.36980E-05	0.20400E+02
0.41750E-05	0.20830E+02
0.42380E-05	0.21240E+02
0.44860E-05	0.21710E+02
0.48760E-05	0.22150E+02
0.51940E-05	0.22630E+02
0.56790E-05	0.23110E+02
0.65180E-05	0.23580E+02
0.73270E-05	0.24070E+02
0.83020E-05	0.24570E+02
0.83080E-05	0.25070E+02

0.85640E-05	0.25590E+02
0.91320E-05	0.26110E+02
0.90100E-05	0.26650E+02
0.96870E-05	0.27330E+02
0.10850E-04	0.28180E+02
0.11720E-04	0.29180E+02
0.12930E-04	0.30400E+02
0.14930E-04	0.31610E+02
0.16490E-04	0.32960E+02
0.17730E-04	0.34260E+02
0.19350E-04	0.35670E+02
0.21780E-04	0.37080E+02
0.23350E-04	0.38560E+02
0.26160E-04	0.40120E+02
0.28630E-04	0.41710E+02
0.29630E-04	0.43340E+02
0.33040E-04	0.45070E+02

STRESS RATIO R = 0.16

da/dN	DELK
0.21220E-07	0.39900E+01
0.32040E-07	0.40800E+01
0.31690E-07	0.41700E+01
0.30950E-07	0.42700E+01
0.33660E-07	0.43600E+01
0.44570E-07	0.44700E+01
0.46770E-07	0.45600E+01
0.42590E-07	0.46700E+01
0.45400E-07	0.47700E+01
0.44130E-07	0.48800E+01
0.43540E-07	0.49900E+01
0.45790E-07	0.51000E+01
0.49580E-07	0.52200E+01
0.55640E-07	0.53400E+01
0.57730E-07	0.54500E+01
0.60460E-07	0.55800E+01
0.63880E-07	0.57000E+01
0.63030E-07	0.58400E+01
0.60630E-07	0.59600E+01
0.56120E-07	0.61000E+01
0.55120E-07	0.62300E+01
0.85050E-07	0.63700E+01
0.64660E-07	0.65200E+01
0.50770E-07	0.66700E+01
0.70390E-07	0.68200E+01
0.71860E-07	0.69700E+01
0.75110E-07	0.71300E+01
0.81520E-07	0.72800E+01

0.86130E-07	0.74400E+01
0.92790E-07	0.76100E+01
0.96440E-07	0.77800E+01
0.95400E-07	0.79500E+01
0.10210E-06	0.81400E+01
0.11520E-06	0.83200E+01
0.12240E-06	0.85000E+01
0.32120E-07	0.43500E+01
0.53210E-07	0.45500E+01
0.96160E-07	0.47400E+01
0.14330E-06	0.49700E+01
0.16110E-06	0.51800E+01
0.17010E-06	0.54100E+01
0.19440E-06	0.56300E+01

STRESS RATIO R = 0.16

da/dN	DELK
0.24620E-08	0.39400E+01
0.84540E-08	0.40000E+01
0.10840E-07	0.40700E+01
0.10240E-07	0.41500E+01
0.10920E-07	0.42300E+01
0.12010E-07	0.43100E+01
0.12830E-07	0.43800E+01
0.17380E-07	0.44700E+01
0.22920E-07	0.45500E+01
0.25110E-07	0.46300E+01
0.27470E-07	0.47200E+01
0.31530E-07	0.48000E+01
0.36520E-07	0.48900E+01
0.39240E-07	0.49800E+01
0.41260E-07	0.50700E+01
0.40610E-07	0.51600E+01
0.39030E-07	0.52600E+01
0.42310E-07	0.53500E+01
0.52930E-07	0.54500E+01
0.60070E-07	0.55500E+01
0.60320E-07	0.56500E+01
0.62600E-07	0.57500E+01
0.65900E-07	0.58500E+01
0.70100E-07	0.59600E+01
0.72270E-07	0.60700E+01
0.74890E-07	0.61800E+01
0.73830E-07	0.62900E+01
0.69020E-07	0.64100E+01
0.70690E-07	0.65200E+01
0.79560E-07	0.66400E+01
0.84260E-07	0.67600E+01

0.79790E-07	0.68800E+01
0.78670E-07	0.70000E+01
0.83130E-07	0.71300E+01
0.89940E-07	0.72500E+01
0.94030E-07	0.73800E+01
0.93910E-07	0.75200E+01
0.97830E-07	0.76500E+01
0.10560E-06	0.77900E+01
0.10320E-06	0.79300E+01
0.97330E-07	0.80800E+01
0.96330E-07	0.82200E+01
0.99900E-07	0.83700E+01
0.10790E-06	0.85200E+01
0.11550E-06	0.86700E+01
0.12100E-07	0.44000E+01
0.15740E-07	0.45700E+01
0.30550E-07	0.47700E+01
0.65290E-07	0.49900E+01
0.88320E-07	0.52200E+01
0.99550E-07	0.54500E+01
0.10460E-06	0.56800E+01
0.10130E-06	0.59200E+01
0.10230E-06	0.61700E+01
0.11170E-06	0.64300E+01
0.12470E-06	0.67100E+01
0.13610E-06	0.70000E+01
0.14680E-06	0.73200E+01
0.15280E-06	0.76300E+01
0.15760E-06	0.79500E+01
0.16340E-06	0.82900E+01
0.17530E-06	0.86500E+01
0.18820E-06	0.90200E+01
0.19960E-06	0.94200E+01
0.21580E-06	0.98200E+01
0.22520E-06	0.10240E+02
0.24550E-06	0.10680E+02
0.27420E-06	0.11130E+02
0.30170E-06	0.11600E+02
0.35630E-06	0.12100E+02
0.42730E-06	0.12600E+02
0.49160E-06	0.13140E+02
0.56130E-06	0.13690E+02
0.69610E-06	0.14300E+02
0.86000E-06	0.14890E+02
0.97270E-06	0.15520E+02
0.12270E-05	0.16180E+02
0.15730E-05	0.16850E+02
0.19030E-05	0.17570E+02
0.25380E-05	0.18320E+02
0.33630E-05	0.19090E+02

0.37630E-05	0.19820E+02
0.43240E-05	0.20660E+02
0.48420E-05	0.21470E+02
0.51670E-05	0.22370E+02
0.58590E-05	0.23300E+02
0.72620E-05	0.24270E+02
0.84780E-05	0.25230E+02
0.90530E-05	0.26300E+02
0.94420E-05	0.27350E+02
0.10460E-04	0.28490E+02
0.11220E-04	0.29670E+02

STRESS RATIO R = 0.16

da/dN	DELK
0.18250E-08	0.44800E+01
0.12410E-07	0.45700E+01
0.19100E-07	0.46800E+01
0.25440E-07	0.47800E+01
0.30810E-07	0.48900E+01
0.33310E-07	0.50000E+01
0.34280E-07	0.51100E+01
0.36320E-07	0.52300E+01
0.35020E-07	0.53400E+01
0.39390E-07	0.54700E+01
0.49420E-07	0.55900E+01
0.52010E-07	0.57100E+01
0.50260E-07	0.58400E+01
0.48480E-07	0.59700E+01
0.51310E-07	0.61000E+01
0.53050E-07	0.62500E+01
0.54630E-07	0.63900E+01
0.54910E-07	0.65400E+01
0.55790E-07	0.66800E+01
0.63520E-07	0.68300E+01
0.68470E-07	0.69800E+01
0.73810E-07	0.71300E+01
0.79990E-07	0.72900E+01
0.79650E-07	0.74600E+01
0.87770E-07	0.76300E+01
0.92690E-07	0.78000E+01
0.88800E-07	0.79700E+01
0.10410E-06	0.81600E+01
0.11140E-06	0.83300E+01
0.10410E-06	0.85200E+01
0.13780E-07	0.48800E+01
0.44580E-07	0.50400E+01
0.99030E-07	0.52600E+01
0.14910E-06	0.54600E+01

0.18340E-06	0.56500E+01
0.23720E-06	0.58500E+01
0.25640E-06	0.60400E+01
0.22220E-06	0.62300E+01
0.18660E-06	0.64400E+01
0.16890E-06	0.66400E+01
0.15860E-06	0.68400E+01
0.16520E-06	0.70800E+01
0.17840E-06	0.73100E+01
0.18040E-06	0.75600E+01
0.20800E-06	0.78200E+01
0.25560E-06	0.81000E+01
0.23010E-06	0.83700E+01
0.20130E-06	0.86600E+01
0.24380E-06	0.89700E+01
0.25700E-06	0.92500E+01
0.24820E-06	0.96100E+01
0.25680E-06	0.99000E+01
0.29000E-06	0.10260E+02
0.35510E-06	0.10600E+02
0.35870E-06	0.10960E+02
0.39280E-06	0.11340E+02
0.44570E-06	0.11710E+02
0.45390E-06	0.12110E+02
0.53130E-06	0.12530E+02
0.67560E-06	0.12940E+02
0.77350E-06	0.13380E+02
0.84850E-06	0.13830E+02
0.93040E-06	0.14310E+02
0.10300E-05	0.14810E+02
0.12020E-05	0.15310E+02
0.15720E-05	0.15850E+02
0.19650E-05	0.16390E+02
0.21120E-05	0.16940E+02
0.24910E-05	0.17500E+02
0.30670E-05	0.18070E+02
0.33260E-05	0.18620E+02
0.35150E-05	0.19260E+02
0.38770E-05	0.19860E+02
0.43320E-05	0.20520E+02
0.52390E-05	0.21230E+02
0.65190E-05	0.21980E+02
0.77680E-05	0.22680E+02
0.89080E-05	0.23430E+02
0.91100E-05	0.24210E+02

REGRESSION OUTCOME

c	n	m	p	q
0.11389E-06	0.19004E+01	0.85600E+00	0.47840E+00	0.98810E+00

SIMULATION OUTPUT

SHORTEST 1% OF CRACK GROWTH LIVES

LIFE
0.19183E+05
0.20971E+05
0.23759E+05
0.24608E+05
0.26555E+05
0.26641E+05
0.27098E+05
0.27890E+05
0.28998E+05
0.30076E+05
0.31128E+05
0.33111E+05
0.33171E+05
0.33438E+05
0.33778E+05
0.34019E+05
0.34121E+05
0.34778E+05
0.34943E+05
0.35060E+05
0.35349E+05
0.35541E+05
0.37142E+05
0.37452E+05
0.38176E+05
0.38687E+05
0.38835E+05
0.38872E+05
0.38938E+05
0.39074E+05
0.39150E+05
0.39524E+05
0.39617E+05
0.39716E+05
0.39998E+05

0.40049E+05
0.40437E+05
0.40473E+05
0.40644E+05
0.40769E+05
0.40923E+05
0.41291E+05
0.41370E+05
0.41825E+05
0.41925E+05
0.42378E+05
0.42553E+05
0.42693E+05
0.43034E+05
0.43133E+05
0.43394E+05
0.43452E+05
0.43558E+05
0.43626E+05
0.44096E+05
0.44256E+05
0.44349E+05
0.44381E+05
0.44391E+05
0.44500E+05
0.44558E+05
0.44759E+05
0.44866E+05
0.44968E+05
0.45066E+05
0.45143E+05
0.45158E+05
0.45166E+05
0.45188E+05
0.45195E+05
0.45199E+05
0.45275E+05
0.45407E+05
0.45410E+05
0.45568E+05
0.45628E+05
0.45664E+05
0.45705E+05
0.46036E+05
0.46159E+05
0.46195E+05
0.46266E+05
0.46293E+05
0.46779E+05
0.46971E+05

```
0.47009E+05
0.47140E+05
0.47283E+05
0.47370E+05
0.47467E+05
0.47512E+05
0.47529E+05
0.47759E+05
0.47957E+05
0.47975E+05
0.47995E+05
0.48217E+05
0.48220E+05
0.48476E+05
0.48558E+05
```

B LIVES:	EMPIRICAL
0.00010	0.19183E+05
0.00050	0.26555E+05
0.00100	0.30076E+05
0.00500	0.43133E+05
0.01000	0.48558E+05

Output File - LOWLIF

1	0.100000E-03	19183.2
2	0.200000E-03	20971.3
3	0.300000E-03	23758.6
4	0.400000E-03	24607.5
5	0.500000E-03	26555.1
6	0.600000E-03	26640.7
7	0.700000E-03	27097.7
8	0.800000E-03	27890.2
9	0.900000E-03	28997.5
10	0.100000E-02	30076.2
11	0.110000E-02	31128.4
12	0.120000E-02	33111.2
13	0.130000E-02	33171.4
14	0.140000E-02	33437.7
15	0.150000E-02	33777.9
16	0.160000E-02	34018.9
17	0.170000E-02	34120.8
18	0.180000E-02	34777.9
19	0.190000E-02	34942.5
20	0.200000E-02	35060.3
21	0.210000E-02	35348.7

22	0.220000E-02	35540.7
23	0.230000E-02	37142.4
24	0.240000E-02	37451.9
25	0.250000E-02	38176.5
26	0.260000E-02	38686.7
27	0.270000E-02	38834.7
28	0.280000E-02	38871.9
29	0.290000E-02	38938.4
30	0.300000E-02	39074.2
31	0.310000E-02	39150.0
32	0.320000E-02	39524.2
33	0.330000E-02	39616.8
34	0.340000E-02	39716.2
35	0.350000E-02	39997.7
36	0.360000E-02	40048.5
37	0.370000E-02	40437.4
38	0.380000E-02	40473.2
39	0.390000E-02	40643.9
40	0.400000E-02	40769.4
41	0.410000E-02	40922.6
42	0.420000E-02	41291.4
43	0.430000E-02	41370.2
44	0.440000E-02	41825.2
45	0.450000E-02	41925.0
46	0.460000E-02	42377.6
47	0.470000E-02	42552.7
48	0.480000E-02	42692.7
49	0.490000E-02	43034.4
50	0.500000E-02	43133.0
51	0.510000E-02	43393.5
52	0.520000E-02	43451.6
53	0.530000E-02	43557.6
54	0.540000E-02	43625.8
55	0.550000E-02	44095.9
56	0.560000E-02	44255.9
57	0.570000E-02	44348.8
58	0.580000E-02	44381.0
59	0.590000E-02	44391.1
60	0.600000E-02	44499.6
61	0.610000E-02	44558.1
62	0.620000E-02	44759.4
63	0.630000E-02	44865.7
64	0.640000E-02	44968.0
65	0.650000E-02	45066.3
66	0.660000E-02	45143.3
67	0.670000E-02	45158.1
68	0.680000E-02	45166.4
69	0.690000E-02	45187.6
70	0.700000E-02	45194.6
71	0.710000E-02	45199.2

72	0.720000E-02	45274.9
73	0.730000E-02	45407.1
74	0.740000E-02	45410.5
75	0.750000E-02	45568.3
76	0.760000E-02	45628.0
77	0.770000E-02	45664.2
78	0.780000E-02	45705.1
79	0.790000E-02	46036.0
80	0.800000E-02	46159.3
81	0.810000E-02	46195.2
82	0.820000E-02	46265.9
83	0.830000E-02	46293.2
84	0.840000E-02	46779.5
85	0.850000E-02	46970.6
86	0.860000E-02	47008.6
87	0.870000E-02	47140.0
88	0.880000E-02	47282.5
89	0.890000E-02	47370.0
90	0.900000E-02	47467.3
91	0.910000E-02	47511.6
92	0.920000E-02	47529.3
93	0.930000E-02	47759.1
94	0.940000E-02	47956.6
95	0.950000E-02	47974.9
96	0.960000E-02	47995.4
97	0.970000E-02	48216.7
98	0.980000E-02	48219.6
99	0.990000E-02	48476.1
100	0.100000E-01	48558.2

2.C.2 External Heat Exchanger Analysis Files

Selected input and output files for the external heat exchanger "all driver" analysis are given here. The analysis program PROCRK requires the input file CRKDAT along with the stress history files. Annotated examples of the data file format for CRKDAT are given in Figure 6.1-2. The input file CRKDAT is given below. Section 6.1.3.1 contains a description of the input variables and a user's guide for running PROCRK.

The output files from a PROCRK run are CRKRES, LOWLIF, and IOUTPR. The CRKRES and LOWLIF from an "all drivers" analysis of the HEX coil are given below. The CRKRES file contains an echo of the input data, output from the crack growth model regression, and the B-lives. The LOWLIF file contains the lowest 100 (1% of total simulated) crack growth failure lives for the EXHEX coil; these failure lives are plotted in Figure 2.4-5.

Input File - CRKDAT

```
2
2
675
0
1
10000
1
0
5
0.0001
0.0005
0.001
0.005
0.01
0.060    0.060    0.50    0.50    0.0    0.0
0.010    0.010    0.50    0.50    0.0    0.0
2.00      2.00     0.150    1.0
2.00      2.00     0.200    1.0
1.00    1.00
1.00    1.00
0.00    0.00
1.00    1.00
1.00    1.00
-0.69310  0.5570
-1.50    -2.50
2
0.00    0.00    5280.0    0.00    0.00    0.00
'NBSZ'  1  0.00      0.00    552.34    0.00     0.00       0.00
'SIN2'  2  0.00      0.00    495.86    0.00     0.00       0.00
2.30
1.00
50.
6001
'C10100 COPPER FROM NASA/JSC'
6100.0  100.0  1  3
2.2642  -2.6912  -0.55288
-2.000  0.00  0.00
8  0.20
5.017E-8  3.037
5.900E-8  3.191
9.798E-8  3.607
1.127E-7  3.649
2.397E-7  4.223
4.069E-7  4.864
5.334E-7  5.473
8.762E-7  6.109
```

Output File - CRKRES

P R O C R K

INPUT DATA

DRIVERS	PARAMETER DISTRIBUTIONS		
		RHO	THETA
CHANNEL WIDTH	Be(0.0600, 0.0600)	U(0.50000, 0.50000)	U(0.0, 0.0)
CRACK SIZE A	Be(0.0100, 0.0100)	U(0.50000, 0.50000)	U(0.0, 0.0)
LAMBDA RANDOM	k: U(2.00000, 2.00000) COEFFICIENT OF VARIATION: 0.150 STRAIN GAGE FACTOR: 1.0000000		
LAMBDA SINE	k: U(2.00000, 2.00000) COEFFICIENT OF VARIATION: 0.200 STRAIN GAGE FACTOR: 1.0000000		
STAT STR ANAL FAC	U(1.00000, 1.00000)		
DYN STR ANAL FAC	U(1.00000, 1.00000)		
LAMBDA Kth	U(0.00000, 0.00000)		
LAMBDA Kc	U(1.00000, 1.00000)		
K CALC FAC	U(1.00000, 1.00000)		
GROWTH CALC FAC	U(-0.69310, 0.55700)		
GROWTH COEFF m	U(-1.50000, -2.50000)		

STRESS INPUT

SX	SY	SZ	SXY	SXZ	SYZ
STATIC					
0.000000	0.000E+00	0.528E+04	0.000E+00	0.000E+00	0.000E+00
NBSZ					
0.000000	0.000E+00	0.552E+03	0.000E+00	0.000E+00	0.000E+00
SIN2					
0.000000	0.000E+00	0.496E+03	0.000E+00	0.000E+00	0.000E+00

MISCELLANEOUS INPUT

WILLENBORG OVERLOAD FACTOR	0.23000E+01
STRESS-TIME HISTORY PERIOD	1.00000
STRESS-TIME HISTORY NOISE FILTER	50.0
NUMBER OF TIME-VARYING LOADS	2
NUMBER OF POINTS IN HISTORIES	6001

MATERIAL INPUT

DESCRIPTION: C10100 COPPER FROM NASA/JSC

YIELD STRENGTH	6100.
CRITICAL S I F	100.
NUMBER OF DIVISIONS	1
REGRESSION OPTION	3

THRESHOLD MODEL DESCRIPTION

DKTHo = 0.22642E+01
Co = -0.26912E+01
d = -0.55288E+00

STRESS RATIO R = 0.20

da/dN	DELK
0.50170E-07	0.30370E+01
0.59000E-07	0.31910E+01
0.97980E-07	0.36070E+01
0.11270E-06	0.36490E+01
0.23970E-06	0.42230E+01
0.40690E-06	0.48640E+01
0.53340E-06	0.54730E+01
0.87620E-06	0.61090E+01

REGRESSION OUTCOME

c	n	m	p	q
0.32734E-09	0.41482E+01	-0.20000E+01	0.00000E+00	0.00000E+00

SIMULATION OUTPUT

SHORTEST 1% OF CRACK GROWTH LIVES

LIFE
0.17902E+05
0.19741E+05
0.20040E+05
0.20227E+05
0.20390E+05
0.21376E+05
0.22207E+05
0.22722E+05
0.22725E+05
0.22967E+05
0.23185E+05
0.23605E+05
0.23905E+05
0.24108E+05
0.24163E+05
0.24266E+05
0.24825E+05
0.24850E+05
0.25085E+05

0.25413E+05
0.25440E+05
0.25667E+05
0.25853E+05
0.25861E+05
0.25961E+05
0.26033E+05
0.26224E+05
0.26345E+05
0.26500E+05
0.26649E+05
0.26662E+05
0.26672E+05
0.26720E+05
0.26809E+05
0.26823E+05
0.26851E+05
0.27022E+05
0.27159E+05
0.27299E+05
0.27389E+05
0.27520E+05
0.27622E+05
0.27659E+05
0.27682E+05
0.27892E+05
0.27898E+05
0.28000E+05
0.28005E+05
0.28066E+05
0.28335E+05
0.28449E+05
0.28458E+05
0.28542E+05
0.28589E+05
0.28760E+05
0.28952E+05
0.28963E+05
0.28988E+05
0.29029E+05
0.29076E+05
0.29098E+05
0.29256E+05
0.29539E+05
0.29556E+05
0.29728E+05
0.29840E+05
0.29842E+05
0.29846E+05
0.29920E+05

0.29942E+05
0.30006E+05
0.30073E+05
0.30247E+05
0.30266E+05
0.30276E+05
0.30346E+05
0.30440E+05
0.30525E+05
0.30534E+05
0.30535E+05
0.30597E+05
0.30599E+05
0.30722E+05
0.30785E+05
0.30799E+05
0.30893E+05
0.30943E+05
0.30954E+05
0.30974E+05
0.30981E+05
0.31024E+05
0.31025E+05
0.31040E+05
0.31075E+05
0.31204E+05
0.31234E+05
0.31367E+05
0.31412E+05
0.31455E+05
0.31457E+05

B LIVES:	EMPIRICAL
0.00010	0.17902E+05
0.00050	0.20390E+05
0.00100	0.22967E+05
0.00500	0.28335E+05
0.01000	0.31457E+05

Output File - LOWLIF

1	0.100000E-03	17901.8
2	0.200000E-03	19741.3
3	0.300000E-03	20040.5
4	0.400000E-03	20227.0
5	0.500000E-03	20390.3

6	0.600000E-03	21375.8
7	0.700000E-03	22207.1
8	0.800000E-03	22722.3
9	0.900000E-03	22724.7
10	0.100000E-02	22967.1
11	0.110000E-02	23185.4
12	0.120000E-02	23605.3
13	0.130000E-02	23904.8
14	0.140000E-02	24107.7
15	0.150000E-02	24163.3
16	0.160000E-02	24265.5
17	0.170000E-02	24824.6
18	0.180000E-02	24850.0
19	0.190000E-02	25085.3
20	0.200000E-02	25413.0
21	0.210000E-02	25439.8
22	0.220000E-02	25667.3
23	0.230000E-02	25853.3
24	0.240000E-02	25861.1
25	0.250000E-02	25961.1
26	0.260000E-02	26032.6
27	0.270000E-02	26224.4
28	0.280000E-02	26344.8
29	0.290000E-02	26500.2
30	0.300000E-02	26649.0
31	0.310000E-02	26661.6
32	0.320000E-02	26672.3
33	0.330000E-02	26720.2
34	0.340000E-02	26808.7
35	0.350000E-02	26823.0
36	0.360000E-02	26850.5
37	0.370000E-02	27022.4
38	0.380000E-02	27159.1
39	0.390000E-02	27299.1
40	0.400000E-02	27389.2
41	0.410000E-02	27520.2
42	0.420000E-02	27621.5
43	0.430000E-02	27659.3
44	0.440000E-02	27681.7
45	0.450000E-02	27891.6
46	0.460000E-02	27897.7
47	0.470000E-02	28000.4
48	0.480000E-02	28005.3
49	0.490000E-02	28065.8
50	0.500000E-02	28335.3
51	0.510000E-02	28449.3
52	0.520000E-02	28458.3
53	0.530000E-02	28541.7
54	0.540000E-02	28588.5
55	0.550000E-02	28760.0

56	0.560000E-02	28952.0
57	0.570000E-02	28963.0
58	0.580000E-02	28988.1
59	0.590000E-02	29028.8
60	0.600000E-02	29075.6
61	0.610000E-02	29098.5
62	0.620000E-02	29256.1
63	0.630000E-02	29538.9
64	0.640000E-02	29555.9
65	0.650000E-02	29727.7
66	0.660000E-02	29840.5
67	0.670000E-02	29842.3
68	0.680000E-02	29846.2
69	0.690000E-02	29919.5
70	0.700000E-02	29942.2
71	0.710000E-02	30006.3
72	0.720000E-02	30073.4
73	0.730000E-02	30246.5
74	0.740000E-02	30265.8
75	0.750000E-02	30275.7
76	0.760000E-02	30345.5
77	0.770000E-02	30439.9
78	0.780000E-02	30524.5
79	0.790000E-02	30534.1
80	0.800000E-02	30535.1
81	0.810000E-02	30597.4
82	0.820000E-02	30598.6
83	0.830000E-02	30721.7
84	0.840000E-02	30784.5
85	0.850000E-02	30799.0
86	0.860000E-02	30893.1
87	0.870000E-02	30942.7
88	0.880000E-02	30954.0
89	0.890000E-02	30974.4
90	0.900000E-02	30980.9
91	0.910000E-02	31024.2
92	0.920000E-02	31025.3
93	0.930000E-02	31039.9
94	0.940000E-02	31074.9
95	0.950000E-02	31204.1
96	0.960000E-02	31233.6
97	0.970000E-02	31367.4
98	0.980000E-02	31412.4
99	0.990000E-02	31455.1
100	0.100000E-01	31457.0

Appendix 2.D
Stress Intensity Factor Expressions

2.D.1 HEX Coil Crack Configuration

The surface flaw in a finite width plate given as solution SC01 in NASA/FLAGRO [9] was used for the HEX coil problem and the SIF expressions are given below. The SIF is given by

$$K = [S_o F_o + S_2 F_2] \sqrt{\pi a}$$

in which S_o and S_2 are the applied tensile and bending stresses, respectively, and F_o and F_2 are their corresponding SIF coefficients given below. The SIF expressions are given for any point along the elliptic boundary of the surface flaw. Angle φ determines the point on the flaw boundary. The coefficients for SIF at the vertex in the depth or "a direction" and at the vertex in the length or "c direction" are derived by setting $\varphi = 0°$ and $\varphi = 90°$, respectively.

$$F_o = M_o\, g\, f_\varphi\, f_w\, f_x$$

$$F_2 = H_c\, F_o$$

in which

$$M_o = M_1 + M_2 v^2 + M_3 v^4$$

$$f_\varphi = \left[(x \cos\varphi)^2 + \sin^2\varphi\right]^{1/4} \text{ for } x \le 1$$

$$= \left[\cos^2\varphi + (x^{-1}\sin\varphi)^2\right]^{1/4} \text{ for } x > 1$$

$$f_w = \sqrt{\sec\left[(\pi c / w)\sqrt{v}\right]}$$

$$f_x = \left[1 + 1.464\, x^{1.65}\right]^{-1/2} \text{ for } x \le 1$$

$$= \left[1 + 1.464\, x^{-1.65}\right]^{-1/2} \text{ for } x > 1$$

$$H_c = H_1 + (H_2 - H_1)\sin^p\varphi$$

The variables in the above equations are given in terms of three non-dimensionalized geometry variables v, w, and x where

$$v = a / t$$

$$w = a / W$$

$$x = a / c$$

in which a is the crack depth, c is half the crack length, t is the plate thickness, and W is the plate width. The variables are given for two ranges of the crack aspect ratio as follows:

For $a / c \leq 1$:

$$M_1 = 1.13 - 0.09\,x$$

$$M_2 = -0.54 + 0.89 / (0.2 + x)$$

$$M_3 = 0.5 - 1 / (0.65 + x) + 14\,(1 - x)^{24}$$

$$g = 1 + \left(0.1 + 0.35\,v^2\right) f^2$$

$$p = 0.2 + x + 0.6\,v$$

$$H_1 = 1 - 0.34\,v - 0.11\,xv$$

$$H_2 = 1 - (1.22 + 0.12\,x)\,v + \left(0.55 - 1.05\,x^{0.75} + 0.47\,x^{1.5}\right) v^2$$

For $a / c > 1$:

$$M_1 = (1 + 0.04 / x)\,x^{-1/2}$$

$$M_2 = 0.2\,x^{-4}$$

$$M_3 = -0.11\,x^{-4}$$

$$g = 1 + \left(0.1 + 0.35\,v^2 / x\right) f^2$$

$$p = 0.2 + x^{-1} + 0.6\,v$$

$$H_1 = 1 + (- 0.04 - 0.41 / x) v + \left(0.55 - 1.93 x^{-0.75} + 1.38 x^{-1.5}\right) v^2$$

$$H_2 = 1 + (- 2.11 + 0.77 / x) v + \left(0.55 - 0.72 x^{-0.75} + 0.14 x^{-1.5}\right) v^2$$

2.D.2 EXHEX Crack Configuration

The crack configuration used for the EXHEX analysis was a crack in a finite width plate subject to tension [19]. The SIF is given by

$$K = S_o F_o \sqrt{\pi a}$$

in which S_o is the applied tensile stress, and F_o is the corresponding SIF coefficients as follows:

$$F_o = \left[\sec \frac{\pi a}{W}\right]^{1/2}$$

in which W is the width of the plate and a is half the crack length.

3.0 Probabilistic Modeling of Turbine Blade Low Cycle Fatigue Life

Section 3.1
Introduction

A Low Cycle Fatigue (LCF) failure model calculates the crack initiation life of a structure subjected to a small number of high amplitude load cycles. As shown in Figure 3.1-1, the information used in the LCF failure model presented here includes values of such drivers as environmental parameters, loads, material properties, and structural parameters and uncertainties about driver values and engineering model accuracy. The available information about drivers, including their uncertainties, is used to synthesize stress or strain histories. Individual cycles of the stress or strain histories are identified and characterized by a value of equivalent stress or strain range that accounts for the mean and extrema of each cycle. The materials characterization model establishes a value of fatigue life for the equivalent stress or strain range of each cycle. The fatigue life for a stress or strain history is computed from the accumulated damage due to a sequence of individual cycles.

The application of the Probabilistic Failure Assessment Methodology to LCF life prediction for the ATD-High Pressure Fuel Turbopump (HPFTP) first stage turbine blades is presented in the following. Figure 3.1-2 shows the low cycle fatigue life calculation procedure in more detail. The major elements of the life calculation procedure are driver selection, driver transformation, rainflow cycle counting for multi-

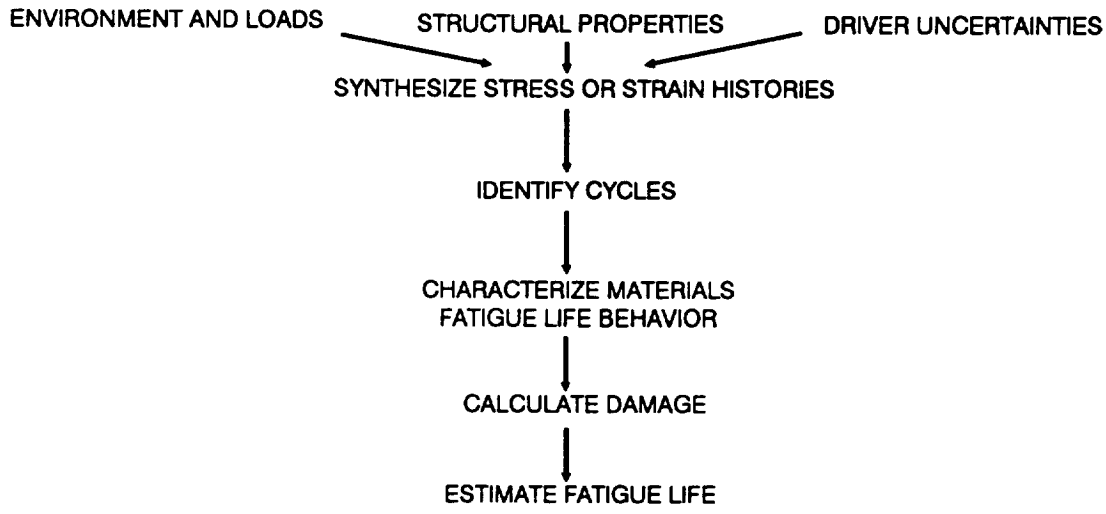

Figure 3.1-1 Low Cycle Fatigue Failure Modeling Approach

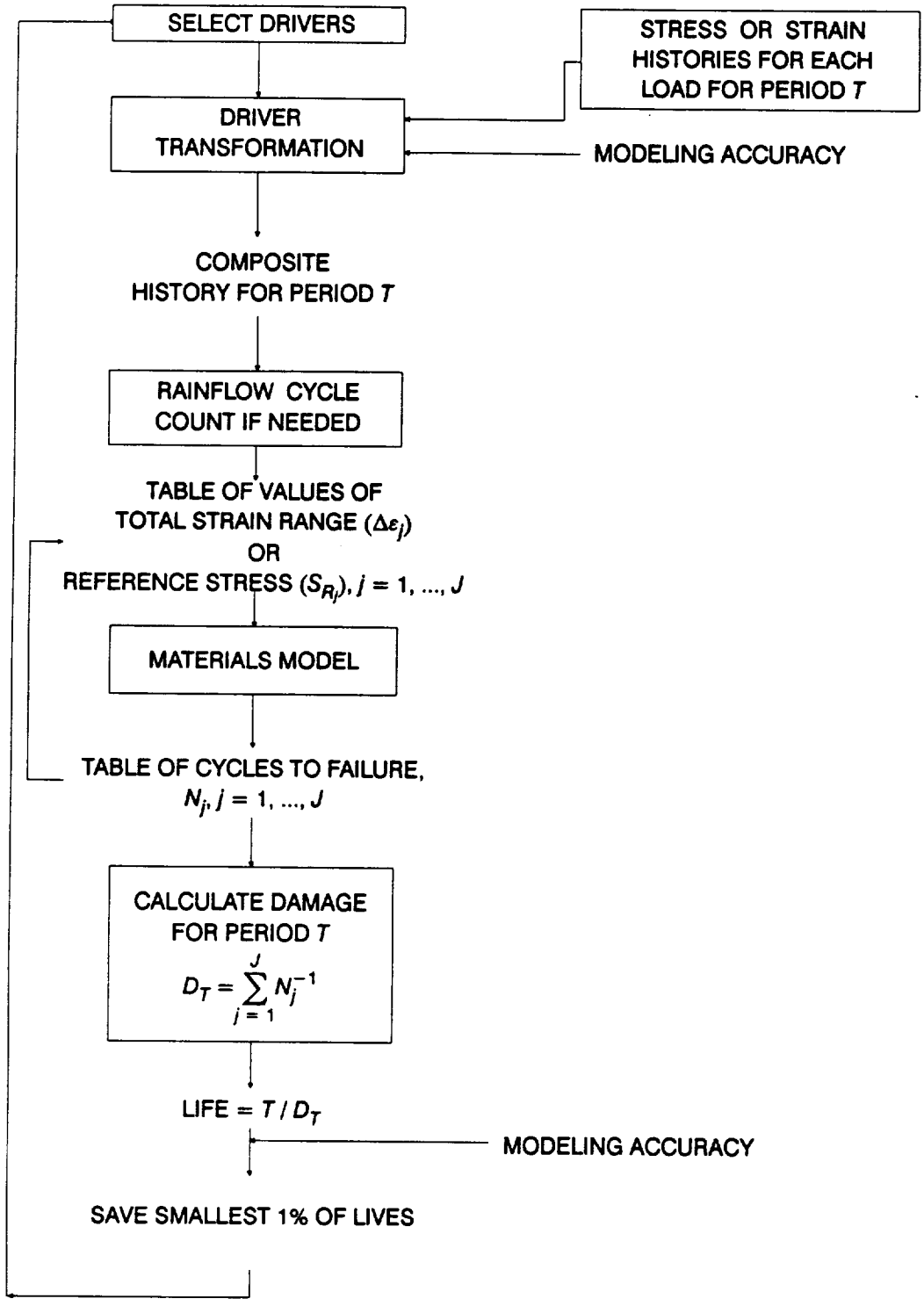

Figure 3.1-2 Calculation Procedure Used in the Low Cycle Fatigue Model

ple cycle histories, the materials model, and the damage accumulation algorithm which is used for multiple cycle histories. In the driver transformation, stress or strain is defined as a function of such drivers as rotational speed and gas temperature.

The driver transformation can be performed in two ways. A rigorous structural analysis can be incorporated within the low cycle fatigue model, or the driver transformation can be accomplished by a parametric representation of the rigorous structural analysis, i.e., by a response surface. The latter approach was chosen because response surface methods gave accurate answers and were computationally efficient. A parametric representation of the structural analysis is obtained by performing a sensitivity analysis using structural finite element models. The results of the sensitivity analysis are then represented by a response surface which characterizes stress or strain as a function of relevant drivers. Relevant drivers are those which engineering knowledge suggests ought to be important and which, by means of a measure of goodness-of-fit, are confirmed to be sufficient to explain observed variation. For our applications, quadratic response surfaces have been adequate to provide an accurate representation of the observed variation.

Factors to account for uncertainties about driver values and modeling accuracy are inserted as appropriate at the steps of the life calculation procedure of Figure 3.1-2. When multiple cycle histories are analyzed, rainflow cycle counting is used to identify individual cycles. The fatigue life corresponding to each cycle is provided by the materials model. The failure time for multiple cycles is obtained from the damage accumulation calculation by using Miner's Rule. Details on rainflow cycle counting, the materials characterization model, and the damage accumulation algorithm can be found in [1], Sections 2.2.1.4, 2.1.2, and 2.2.1.4, respectively.

The ATD-HPFTP Turbine Blade low cycle fatigue model is described below. The engineering analysis and driver transformation are presented, followed by a discussion of the implementation of the failure simulation. The development of this model and its application to the ATD-HPFTP first stage turbine blades was a collaborative effort between Pratt & Whitney and JPL.

Section 3.2
Turbine Blade LCF Analysis

3.2.1 Component Description

The ATD-HPFTP Turbine Blades are hollow single-crystal castings. Figure 3.2-1 shows the axial cross section of the ATD-HPFTP turbine with its monolithic disk and both stages of turbine blades. The first stage turbine has fifty blades. The turbine is driven by high temperature, high pressure steam (H_2O) and gaseous hydrogen (H_2).

3.2.2 Modeling Approach

The LCF analysis for the first stage turbine blades was performed at the location identified in Pratt & Whitney's design analysis as having the largest local total strain range and as the controlling location for LCF crack initiation life. This critical location is on the airfoil suction face just above the fillet where the blade airfoil attaches to the platform, and the fact that there are fifty such locations is taken into account in the failure simulation. The position of the critical location is shown in Figure 3.2-2.

The strains in the blade at the critical location are produced by mechanical and thermal strains. The mechanical strain is due to centrifugal effects caused by blade pull due to the mass of the blade itself. The thermal strain is primarily due to the thermal gradients in the foil attachment region during start-up and shutdown transients.

The test specimens of the blade material were subjected to stress controlled cyclic loading (frequency = 20 Hz) with a stress ratio R of –1.0 in fatigue testing at Pratt & Whitney. The fatigue tests were performed in 5000 psig hydrogen at room temperature. The test specimens were smooth and in the [001] or radial orientation. Details of the materials characterization model can be found in Section 2.1.2 of [1].

3.2.3 Mission Strain History for the Blade

A representative strain-time history for the blade is shown in Figure 3.2-3. The start-up and shutdown transients dominate the mission duty because, according to preliminary analysis, the minor throttle-down cycle contributes negligible damage. Since the history has multiple cycles, rainflow cycle counting and Miner's rule were used to calculate damage. The history typically reduces to two cycles: (t_2, t_6) and (t_3, t_4). In the failure simulation to be described in Section 3.2.9, the

3.6

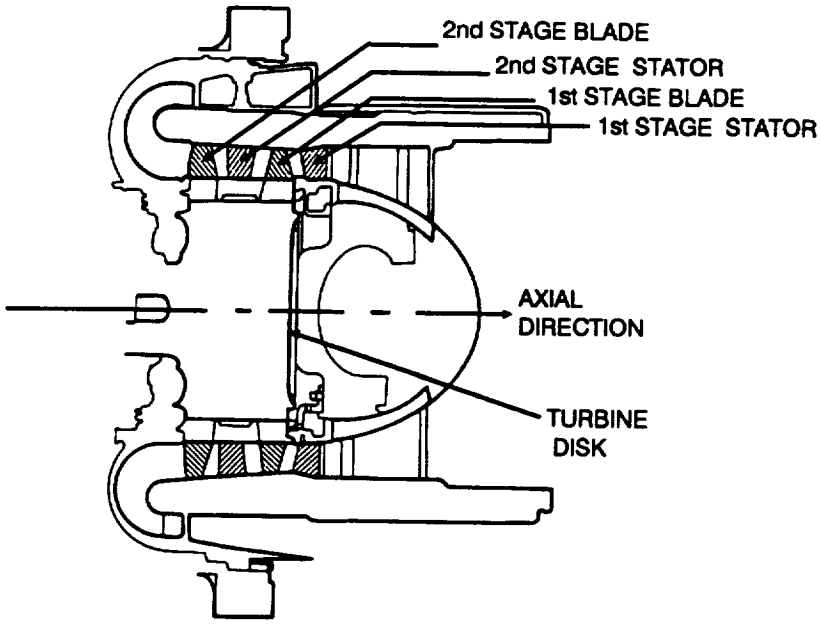

Figure 3.2-1 Axial Cross Section of the ATD-HPFTP Turbine Showing the Monolithic Disk and Both Stages of Blades

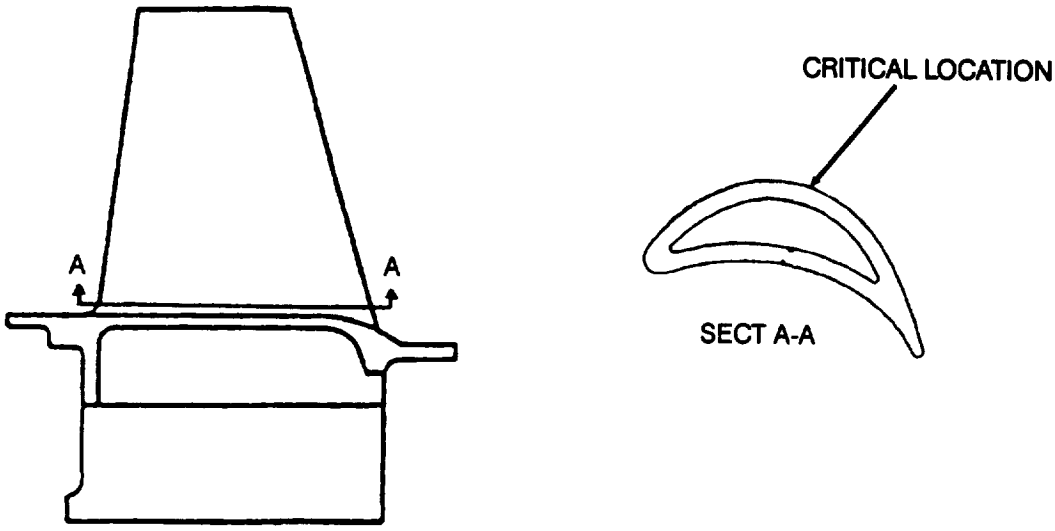

Figure 3.2-2 ATD-HPFTP First Stage Turbine Blade

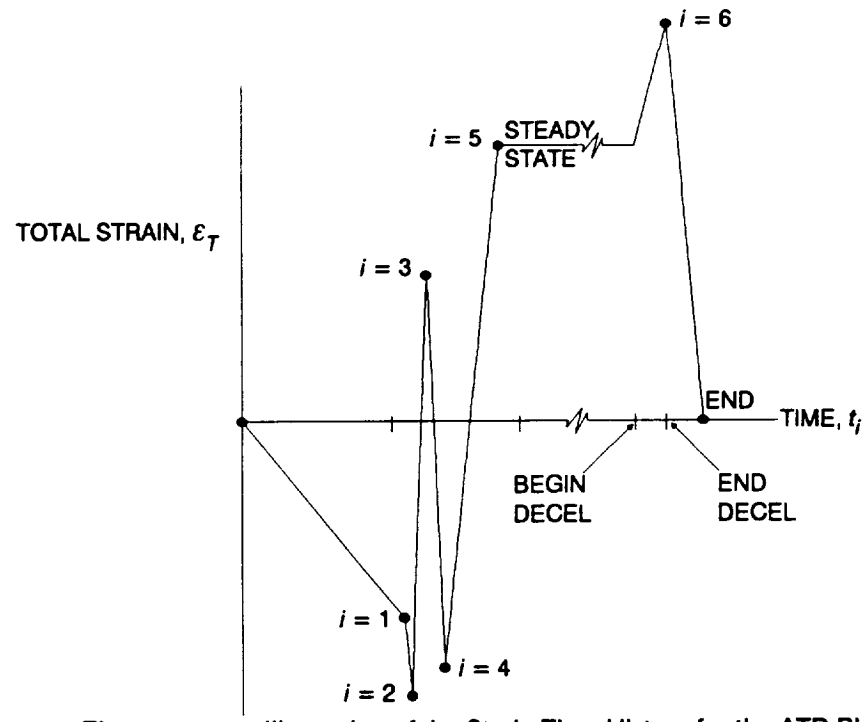

Figure 3.2-3 Illustration of the Strain-Time History for the ATD Blade

value of total strain corresponding to each t_i, $i = 1, ..., 6$ is treated as a random variable according to the calculation procedures given in the following.

3.2.4 Driver Transformation

Within the strain range predicted by preliminary deterministic analysis for the critical location, the single crystal material behaves with negligible inelasticity. The total elastic strain at the critical location can be written as the sum of mechanical, thermal, and bending components

$$\varepsilon_T(t_i) = \varepsilon_B(t_i) + \varepsilon_M(t_i) + \varepsilon_{TH}(t_i), \quad i = 1, ..., 6 \tag{3-1}$$

where $\varepsilon_T(t_i)$ is the total strain at t_i; $\varepsilon_M(t_i)$ is the mechanical strain at t_i due to blade pull; $\varepsilon_{TH}(t_i)$ is the thermal strain at t_i due to the thermal gradient; and $\varepsilon_B(t_i)$ is the strain due to gas bending and blade tilt at t_i. ε_B contributes negligibly to damage because the strain due to gas bending is negated by the strain due to tilt bending; consequently, $\varepsilon_B(t_i)$, $i = 1, ..., 6$ is zero in this analysis.

The thermal strain $\varepsilon_{TH}(t_i)$ due to thermal gradient was found to be primarily dependent on the gas flow conditions during the start and shutdown transients. During the start transient shown in Figure 3.2-3, the flow conditions can be

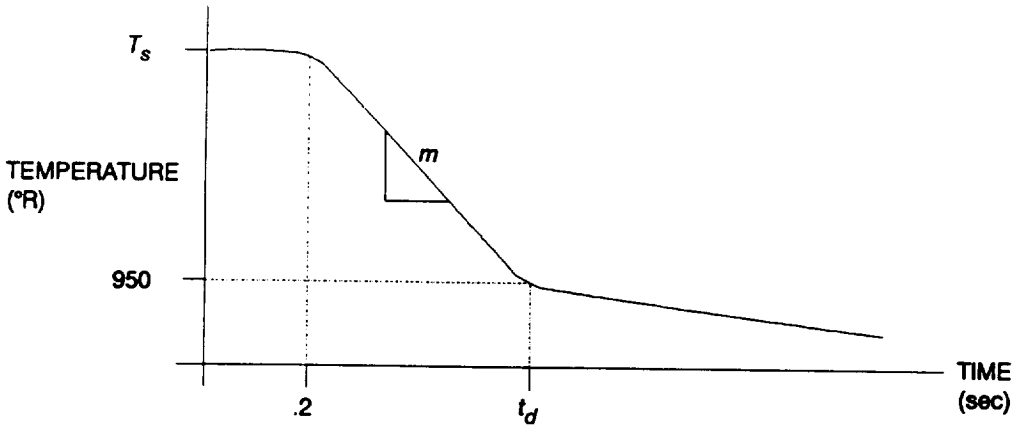

Figure 3.2-4 Schematic of Temperature Profile During Shutdown

described in terms of the gas temperature T_{gas} and gas film coefficient h_{gas}. Sensitivity analyses[1] were performed for nine different temperature and film coefficient combinations which covered their ranges of uncertainty. A flow model was used to establish boundary conditions for a MARC model to obtain the total strain for each flow condition, then the mechanical strain[2] was subtracted to obtain the values for the thermal strains. The nominal thermal strain $\varepsilon_{THnom}(t_1)$ was represented by the following quadratic response surface model [2-7]

$$\varepsilon_{THnom}(t_1) = f_A(T_{gas}, h_{gas}) + e_A = a_0 + a_1 T_{gas} + a_2 h_{gas} + a_3 T_{gas}^2 + a_4 h_{gas}^2 + a_5 T_{gas} h_{gas} + e_A \quad (3\text{-}2)$$

where the coefficients a_0 through a_5 were determined by the procedure given in Section 3.4.2, and e_A is an additive modeling uncertainty characterizing the goodness of fit for the response surface. The MARC finite element (FE) analysis was performed at a nominal rotor speed ω_o of 38,482 rpm for which the nominal mechanical strain ε_{Mnom} was 0.295%. The values obtained for the response surface coefficients are $a_0 = 7.27 \times 10^{-3}$, $a_1 = 6.74 \times 10^{-5}$, $a_2 = -5.91 \times 10^{-5}$, $a_3 = -3.53 \times 10^{-8}$, $a_4 = 1.08 \times 10^{-8}$, $a_5 = -2.74 \times 10^{-8}$, and e_A is a driver discussed in Section 3.3.1.

---

1 In the analyses performed at Pratt & Whitney, a 2-D model was used at nominal or base conditions and a 1-D model was used for the eight perturbation combinations. See Section 3.4.2 for more details.

2 The mechanical strain at t_1 is negligible because the rotor speed is only 225 rpm.

During the shutdown transient shown in Figure 3.2-4, the gas flow conditions can be described in terms of the slope m of the gas temperature versus time curve during deceleration and the gas temperature at the beginning of the shutdown transient T_s. The nominal thermal strain during shutdown was characterized by a 1-D analysis performed by Pratt & Whitney with a set of values of m and T_s which covered their ranges of uncertainty, then a quadratic response surface [2-7] was fit to the thermal strain results

$$\varepsilon_{THnom}(t_6) = f_{D1}(m, T_s) + e_D = d_{10} + d_{11}\, T_s + d_{12}\, m + d_{13}\, T_s^2 \qquad (3\text{-}3)$$

$$+ d_{14}\, m^2 + d_{15}\, T_s\, m + e_D$$

where e_D is an additive modeling uncertainty characterizing the goodness of fit for the response surface.[3] The values of the response surface coefficients obtained by the procedure given in Section 3.4.2 are $d_{10} = -0.13$, $d_{11} = 2.27 \times 10^{-4}$, $d_{12} = -5.93 \times 10^{-5}$, $d_{13} = 0$, $d_{14} = 0$, $d_{15} = 4.72 \times 10^{-8}$, and e_D is a driver discussed in Section 3.3.1.

The uncertainty factor for the coefficient of thermal expansion λ_α and the uncertainty factor for thermal strain analysis λ_{TH} may be combined with the response surface functions given by Equations 3-2 and 3-3 to obtain the total thermal strain at t_i, $i = 1, \ldots, 6$

$$\left.\begin{aligned} \varepsilon_{TH}(t_1) &= \lambda_\alpha\, \lambda_{TH} \left[f_A(h_{gas}, T_{gas}) + e_A \right] \\ \varepsilon_{TH}(t_i) &= \lambda_\alpha\, \lambda_{TH}\, \lambda_G\, \varepsilon_{THnom}(t_i), \quad i = 2, 3, 4 \end{aligned}\right\} \text{ (start transient)} \qquad (3\text{-}4)$$

$$\varepsilon_{TH}(t_5) = \lambda_\alpha\, \lambda_{TH}\, \varepsilon_{THnom}(t_5) \qquad \text{(steady state)}$$

$$\varepsilon_{TH}(t_6) = \lambda_\alpha\, \lambda_{TH} \left[f_{D1}(m, T_s) + e_D \right] \qquad \text{(shutdown transient)}$$

where

λ_α = coefficient of thermal expansion variation factor

λ_{TH} = thermal strain analysis accuracy factor

$f_A(\cdot)$ = response surface for the nominal thermal strain at t_1, $\varepsilon_{THnom}(t_1)$

---

[3] See Section 3.4.2 for more details.

h_{gas} = gas film coefficient at t_1

T_{gas} = gas temperature (°R) at t_1

e_A = response surface accuracy for t_1

λ_G = thermal strain uncertainty factor due to gas temperature variation during start

$\varepsilon_{THnom}(t_i)$ = nominal thermal strain at t_i, $i = 2, ..., 5$

$f_{D1}(\cdot)$ = response surface for the nominal thermal strain at t_6, $\varepsilon_{THnom}(t_6)$

m = deceleration slope at shutdown (°R/sec)

T_s = gas temperature at start of deceleration (°R)

e_D = response surface accuracy for t_6

The mechanical strain due to blade pull $\varepsilon_M(t_i)$ can be expressed analytically as a function of rotor speed and blade mass. This allows the strain ε_M for the start and shutdown transients and steady state to be adjusted for rotor speed and uncertainty in blade mass, as follows:

$$\varepsilon_M(t_i) = \lambda_P \lambda_{MA} C_{MS}(t_i) \varepsilon_{Mnom}, \; i = 1, ..., 6 \tag{3-5}$$

where $C_{MS}(t_i) = \left(\omega(t_i)/\omega_o\right)^2$, $i = 1, ..., 6$ is the speed variability correction factor at t_i and

λ_P = deviation in blade pull load due to uncertainty in blade mass

λ_{MA} = mechanical strain analysis accuracy factor

$\omega(t_i)$ = actual rotor speed at t_i, $i = 1, ..., 6$

ω_o = nominal rotor speed

ε_{Mnom} = nominal mechanical strain at rotor speed ω_o

Preliminary sensitivity analyses[4] showed that rotor speed during the start transient is not a significant driver. However, during the shutdown transient, the mechanical strain due to rotation contributes significantly to total strain $\varepsilon_T(t_6)$. Figure 3.2-4 illustrates how the time t_d was obtained in order to calculate $\omega(t_6)$. An analysis of available SSME test data by Pratt & Whitney indicated that the deceleration slope begins approximately 0.2 seconds after throttle-down and that blade thermal strain is not significantly affected after the gas temperature drops below 950°R. Consequently, t_d is taken as the time at which gas temperature drops below 950°R. In the blade LCF model, the deceleration slope m and gas tempera-

[4] See Section 3.4.2 for more details.

ture T_s are independently specified and can be either fixed parameters or random variables. Given values of m and T_s, t_d can be found from

$$t_d = f_{D2}(m, T_s) = 0.20 + (T_s - 950)/m \tag{3-6}$$

An analysis of engine test data indicated that the rotor speed at time t_6 may be expressed in terms of t_d by

$$\omega(t_6) = f_{D3}(t_d) = d_{31} + d_{32}\, t_d \tag{3-7}$$

where d_{31} = 30,523 and d_{32} = 21,846 are coefficients from the data analysis.

The nominal thermal strain history and the corresponding nominal rotor speed history for the turbine blade critical location are summarized in Table 3.2-1 for t_i, i = 1, ..., 6. The steady state rotor speed $\omega(t_5)$ is characterized by a Normal distribution and is discussed in Section 3.3.1.

3.2.5 Mean Strain Effects

This LCF analysis was conducted using the stress formulation of the stochastic fatigue life model which is based on an equivalent zero-mean strain. This materials fatigue life model is described in Section 2.1.2.1 of [1]. The strain cycles from rainflow counting were adjusted to the equivalent zero-mean strain amplitudes to be compatible with this fatigue life model. The equivalent zero-mean strain range given by the Walker relation [8] was used in this analysis and is

$$\Delta\varepsilon_{EQ} = \left(\frac{\Delta\varepsilon}{2\varepsilon_{max}}\right)^{w-1} \Delta\varepsilon \tag{3-8}$$

Table 3.2-1 Nominal History for the ATD-HPFTP First Stage Turbine Blade

i	$\varepsilon_{THnom}(t_i)$ (%)	$\omega(t_i)$ (rpm)
1	$f_A(h_{gas}, T_{gas}) + e_A$	225.8
2	-0.196921	3025.1
3	0.146025	6138.8
4	-0.200128	8309.0
5	0.007393	$\omega(t_5)$
6	$f_{D1}(m, T_s) + e_D$	$f_{D3}(t_d)$

where ε_{max} is the maximum or peak strain, $\Delta\varepsilon$ is the strain range, and w is the characteristic Walker exponent for the material. A value of .5 for w was used for the blade material PWA 1480.

3.2.6 Damage Calculations

The finite life approach employing a strain time was used. A key step in damage calculations is identification of the number of strain cycles in the strain time history and their extreme values. A cycle counting method called the *rainflow technique* has been implemented. Rainflow cycle counting is discussed in detail in [1], Section 2.2.1.4 and Appendix 2.A.

Failure is considered to be due to damage accumulation from a finite number of cycles. Damage accumulation is performed using Miner's rule, given by Equation 2-91 of [1]. Thermal-mechanical fatigue effects could be considered by the factor λ_{TMF}, which is a multiplier on the life L as given by Equation 2-91 of [1]. λ_{TMF} was not used in the analysis presented here.

3.2.7 Alternative Characterizations of the ATD Blade LCF Materials Model

The approach to modeling materials fatigue life probabilistically that was used in the LCF analysis presented here is described in detail in [1]. The *stress* formulation of the materials model described in [1] was used for the ATD turbine blade LCF analysis because the blade material exhibits elastic behavior in the strain range encountered in this application. In the following Sections 3.2.7.1 and 3.2.7.2, the procedure used in [1] to establish materials model parameters is reviewed, then an alternative procedure called "bootstrapping" is described. Both of these procedures were applied in the turbine blade LCF analysis and results for both procedures are given in Section 3.3.

3.2.7.1 Parameter Uncertainty

The ATD blade LCF analysis utilizes a simple multiplicative stress/life materials model of the form

$$N = A\,S^{-m}\varepsilon \tag{3-9}$$

Variation in material life is modeled by a multiplicative Weibull variate, ε, which has its distributional parameters constrained so that the median value of ε is 1.

What we require is to characterize the materials model used to compute fatigue failure by using operating environment materials data to impute possible values of A, m, and the parameters of the Weibull variate.

The current procedure for characterizing uncertainty in materials model parameters may require constraints due to some possible parameter values lying outside ranges of plausibility.

If we let $A = K^m$ and $\varepsilon = \varphi^m$, the regression equation

$$\ln S = \ln K - \frac{1}{m} \ln N + \ln \varphi \tag{3-10}$$

can be derived from Equation 3-9. The properties of the Weibull distribution are used to standardize the regression equation, i.e., adjust the constant term so that the disturbance term has expected value zero.

$$\ln S = (\ln K + \ln \eta_o - \gamma / \beta_o) - \frac{1}{m} \ln N + (\ln \varphi - \ln \eta_o + \gamma / \beta_o) \tag{3-11}$$

where γ = Euler's constant and $\varphi \sim W(\eta_o, \beta_o)$. This adjusted disturbance term has variance $\pi^2 / 6\beta_o^2$. The regression equation

$$\ln N = \ln A - m \ln S + \ln \varepsilon \tag{3-12}$$

derived from Equation 3-9 is equivalent to the standardized form

$$\ln N = (\ln A + m \ln \eta_o - m\gamma / \beta_o) - m \ln S + (\ln \varepsilon - m \ln \eta_o + m \gamma / \beta_o) \tag{3-13}$$

with $\varepsilon \sim W(\eta_o^m, \beta_o / m)$.

Equations 3-11 and 3-13 are used together to provide the point and interval estimates used to characterize the materials model.

The least squares residuals from Equation 3-11 can be used to construct an interval estimate of $\sqrt{Var(\ln S / N)}$ which is approximately C, the coefficient of variation of fatigue strength. Since values of C have been computed for many samples of a material, that calculation provides an intuitive basis for evaluating the reasonableness of the characterization of materials properties.

The most common form of exogenous information that can be used is an upper bound on the coefficient of variation of fatigue strength, which can be imputed from the aforementioned past experience. In our procedure, that constraint is translated algebraically into a constraint on m which modifies the interval estimate for m derived from least squares estimation of Equation 3-13.

In the foregoing characterization of material properties, the simulation procedure illustrated in Figure 3.2-5 is as follows:

- For each simulation iteration, draw from a distribution on m (e.g., continuous Uniform) assigned over the credibility range established by an interval estimate for m and any constraints.

- Conditional on the value of m selected, consider Equation 3-11 rewritten as

$$(\ln S + \frac{1}{m} \ln N) = (\ln K + \ln \eta_o - \gamma / \beta_o) + (\ln \varphi - \ln \eta_o + \gamma / \beta_o) \quad (3\text{-}14)$$

  β_o is then determined from the variance estimate based on least squares residuals from Equation 3-14; η_o is determined from β_o and the constraint that the median value of φ (equivalently, ε) is one; and, finally K is determined from the least squares estimate of the constant term in Equation 3-14, together with the values of β_o and η_o.

Recall that $A = K^m$ and $\varepsilon = \varphi^m$. Thus, within each iteration of the simulation, this procedure defines the materials model, $N = A\, S^{-m}\varepsilon$, which is used to compute fatigue failure. Across iterations it captures both intrinsic variation as well as uncertainty in the values of A, m, and the parameters of the Weibull variate.

A simpler, less conservative procedure is to use bootstrapping to represent uncertainty in A, m, and the Weibull variate parameters and use the least squares procedure, within each simulation iteration, as illustrated in Figure 3.2-6, to impute specific values for those parameters for each iteration.

Using Equation 3-13, least squares produces a unique m value; β_o is determined from m and the variance estimate based on least squares residuals; η_o is determined from β_o and the constraint that the median value of ε is one; and, finally, A is determined from the least squares estimate of the constant term in Equation 3-13, together with the values of m, β_o, and η_o.

Within each iteration of the simulation, this procedure defines the materials model, $N = A\, S^{-m}\varepsilon$, which is used to compute fatigue failure. Across iterations it captures both intrinsic variation as well as uncertainty in the values of A, m, and the parameters of the Weibull variate.

3.2.7.2 A Procedure for Bootstrapping the Impact of Limited Stress/Life Data

Under the operating environment, the materials characterization data set available for the ATD blade LCF failure mode is too small to permit bootstrapping as a

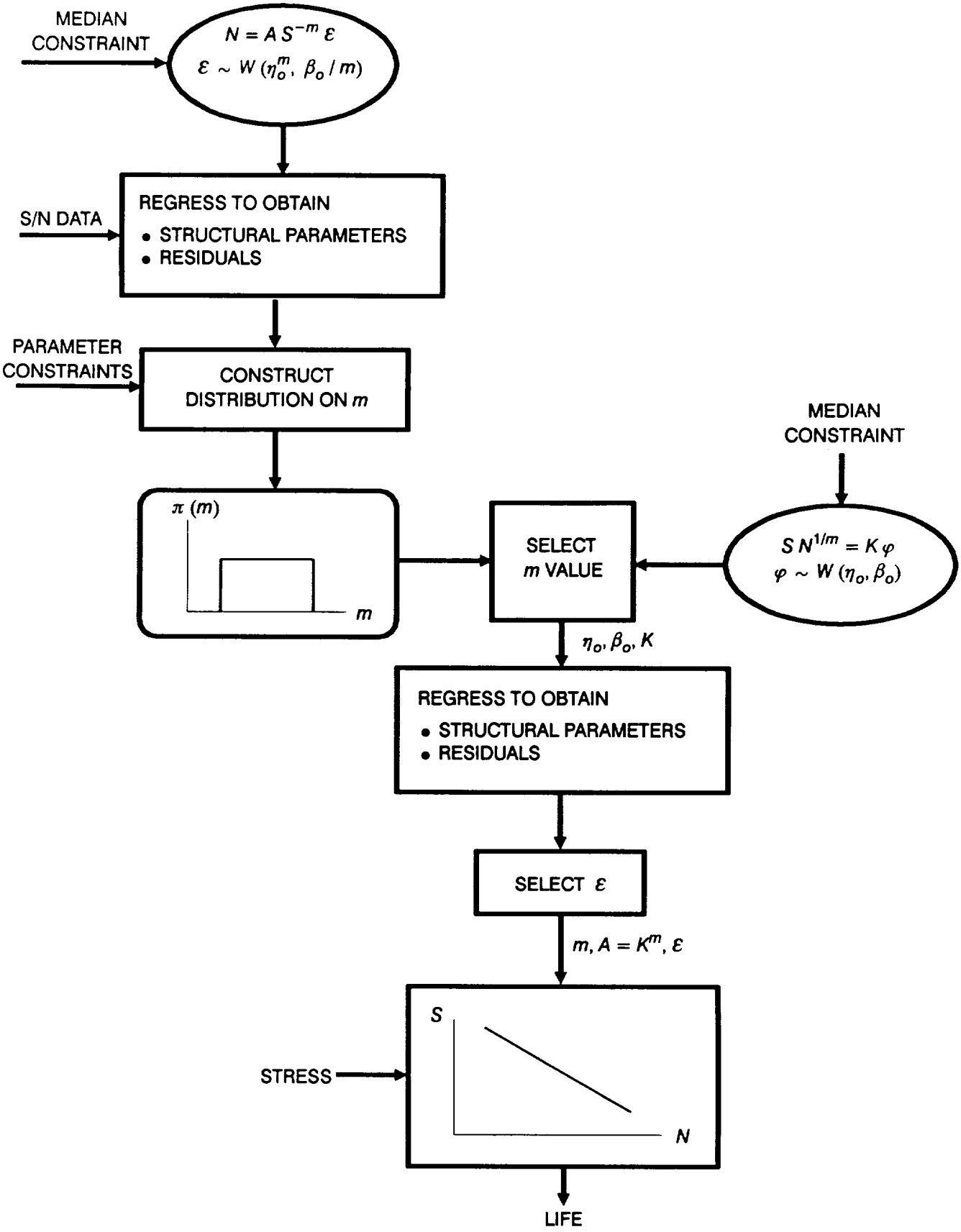

Figure 3.2-5 The Simulation Structure for the Parametric Representation of Parameter Uncertainty

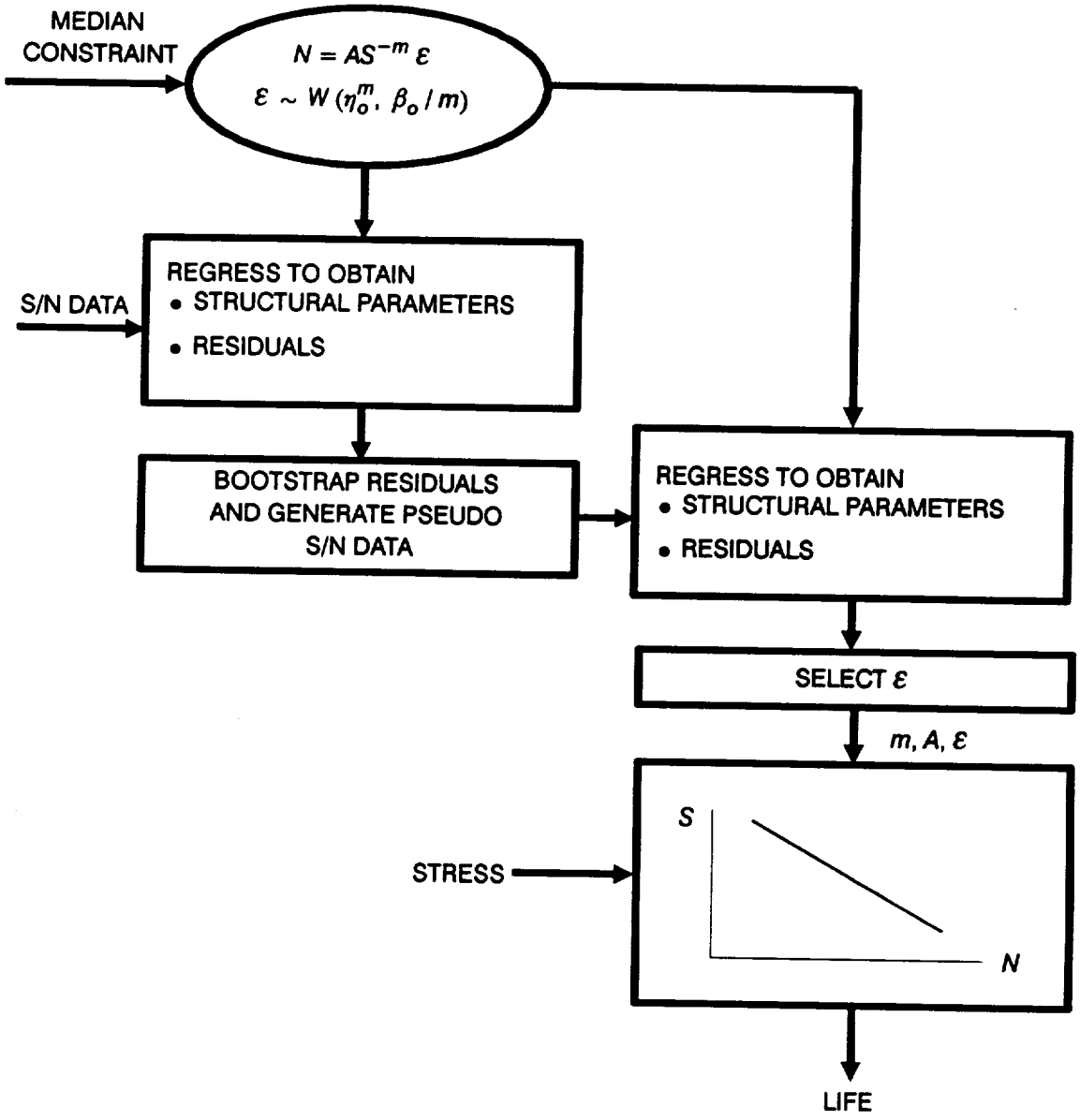

Figure 3.2-6 The Simulation Structure for the Bootstrapping Representation of Parameter Uncertainty

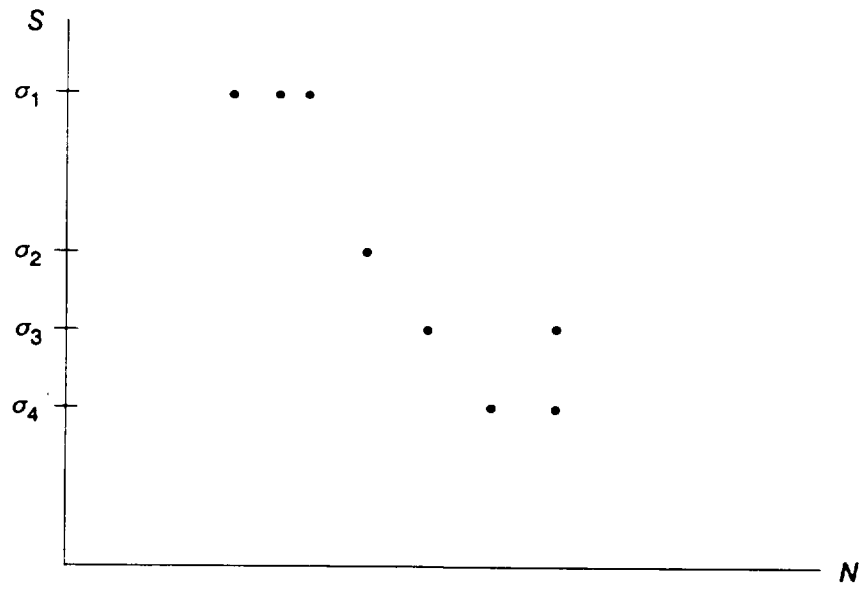

Figure 3.2-7 Plot of Eight Specimen Failure Points

useful substitute for a parametric stochastic characterization of intrinsic material failure uncertainty.

However, bootstrapping can be very useful for the purpose of characterizing parameter specification error in the materials model, which is a source of uncertainty that it is especially important to model when the relevant materials data base is small. Due to the algebraic properties of the materials model we use, Algorithm 3 in [9] is suggested.

For example, consider an ATD blade LCF stress/life materials model linear in log space and suppose we have 8 specimen failure points available, as illustrated in Figure 3.2-7.

Our model is of the form $N = A\, S^{-m} \varepsilon$ with $\text{MED}[\, \varepsilon \mid S \,] = 1$. The following bootstrap procedure can be used to characterize uncertainty in the values of A and m in the materials model.

Step 1: Construct the residual vector in log space $\underline{e} = (e_1, \ldots, e_8)$ corresponding to the estimated regression equation

$$\ln N_i = \hat{a} - \hat{m} \ln S_i + e_i$$

Step 2: For a given covariate (S) value, S_i^*, draw from $\underline{e}$, obtaining e^*, and find a pseudo-sample value of N_i, N_i^*, from

$$\ln N_i^* = \hat{a} - \hat{m} \ln S_i^* + e^* \sqrt{\frac{8}{8-2}}$$

Execute this for the covariate values in the original data set. Thus, 3 pseudo-values of N are generated at the highest value of S, etc. This procedure results in a pseudo-data set

$$\left[(N_1^*, \sigma_1), (N_2^*, \sigma_1), (N_3^*, \sigma_1), (N_4^*, \sigma_2), (N_5^*, \sigma_3), (N_6^*, \sigma_3), (N_7^*, \sigma_4), (N_8^*, \sigma_4)\right]$$

Step 3: For a simulation iteration, use the pseudo-data set to characterize intrinsic materials variation by estimating a materials model of the form $N = A\, S^{-m} \varepsilon$ with MED[ε | S] = 1 and use that estimate to compute component failure.

Step 4: For each additional simulation iteration, repeat Steps 2 and 3.

The effect of Steps 1–4 is to characterize uncertainty in A and m implied by the existing data under the model specification and homogeneity assumption implied by the materials model. Intrinsic materials variation is modeled in Step 3, where a realization of ε, derived from the estimated distribution on ε, is executed in order to compute component failure.

Suppose, instead of Weibull variation, that material life variation is modeled by a multiplicative Lognormal variate, ε, with its distributional parameters constrained so that the median value of ε is 1. The only impact on the analysis will be that Equations 3-10 and 3-12 do not need to be adjusted since the median constraint implies that ln φ and ln ε both have zero mean. VAR (ln φ) = σ^2 and VAR (ln ε) = $m^2 \sigma^2$ when $\varphi \sim \Lambda(0, \sigma^2)$ and $\varepsilon \sim \Lambda(0, m^2 \sigma^2)$.

3.2.7.3 Spatial Symmetry Effects

For the assumptions of either Weibull or Lognormal material variation, the effect of N-part symmetry of a component on failure can be derived. For the ATD blade LCF analysis, simulated failure will occur at the location having the smallest of N simulated disturbance terms corresponding to Equation 3-13 (Weibull) or 3-12 (Lognormal).

In the case of Weibull materials variation, the solution is analytical. From Equation 3-13 and the Weibull assumption, the distribution function of the disturbance term

$$V = \ln \varepsilon - m \ln \eta_o + m \gamma / \beta_o$$

can be shown to be

$$F_V(v) = 1 - \exp\left\{ -\exp\left[\left(\frac{\beta_o}{m} \right) v - \gamma \right] \right\}$$

Letting $X = \min_N (V)$,

$$F_x(x) = 1 - Pr\,(X > x)$$

$$= 1 - \prod_{i=1}^{N} Pr\,(V_i > x)$$

$$= 1 - \exp\left\{ - N \exp\left[\left(\frac{\beta_o}{m} \right) x - \gamma \right] \right\}$$

Given a simulated value of $F_x(x)$, the solution of this equation for x provides the desired smallest disturbance term, indicative of the worst materials curve.

In the case of Lognormal materials variation, the solution involves standard numerical approximations for inverting a Normal distribution function. From Equation 3-12 and the Lognormal assumption, the distribution function of the disturbance term $V = \ln \varepsilon$ is $N\,(0, \sigma^2)$. Thus,

$$F_x(x) = 1 - \left[Pr\,(V > x) \right]^N$$

$$= 1 - \left[Pr\,(Z > x / \sigma) \right]^N$$

where $Z \sim N\,(0, 1)$. The algorithm given in 26.2.23 of [10] has been used to provide the desired value of the smallest disturbance term, given a simulated value of $F_x(x)$.

3.2.8 Modeling Multiple Critical Locations

The fact that only one blade is modeled by the engineering analysis while there are fifty identical blades in the first stage must be considered. The procedure for modeling LCF failure in this case is discussed in [1], Section 2.1.6 and is used in the turbine blade LCF model.

3.2.9 Probabilistic Failure Model Implementation

The Probabilistic Failure Model (PFM) for turbine blade low cycle fatigue failure generates a distribution of failure times that results from the probabilistic characterization of drivers. As shown in Figure 3.2-8, the PFM for the blade consists of the materials model, the LCF failure simulation, the structure for selection of drivers, and the procedure for characterizing the simulated failures as a Bayesian prior failure distribution for the purpose of allowing the impact of any available blade success/failure data to be included in the characterization of the blade failure distribution. Since the current analysis is for a candidate blade, no test data is available to use Bayesian updating.

In the PFM shown in Figure 3.2-8, h_{gas}, T_{gas}, m, and λ_G are characterized by Beta distributions; $\omega(t_5)$, T_s, e_A, and e_D are characterized by Normal distributions; and ε_B, λ_P, λ_{MA}, λ_α, λ_{TH}, λ_{dam}, and λ_{TMF} are characterized by Uniform distributions. The materials model provides a family of stochastic curves relating fatigue life to strain. In the outer loop, to be executed N times, the Beta distributions are selected for h_{gas}, T_{gas}, m, and λ_G; the values of λ_{MA} and λ_{TH} are drawn; and the materials model parameters are established. Then, in the inner loop, to be carried out n times, values of ε_B, λ_P, $\omega(t_5)$, λ_α, h_{gas}, T_{gas}, m, λ_G, T_s, e_A, e_D, λ_{dam}, and λ_{TMF} are drawn from their respective distributions.

Since there are fifty blades on the disk, the appropriate realization of the stochastic strain-life curve to use in computing component life for each inner loop iteration will be that corresponding to the minimum of fifty selections of the materials model parameter, φ. See [1], Section 2.1.6 for further explanation. Since a blade LCF life is calculated for each inner loop iteration, a total of Nn simulated failure times will be calculated. The blade results presented in Section 3.3.4 were obtained using N = 20,000. Since the failure probabilities of interest are of the order 10^{-3}, only the smallest one percent of these failure times is saved and used to calculate the Bayesian Prior Distribution parameters α, β, θ. The procedure for calculating α, β, and θ is discussed in [1], Section 2.1.1.

The double-loop structure allows the user to improve computing efficiency for large sample sizes. The simulation may be run in a single loop rather than a double loop by specifying a value of 1 for n. It was found that for driver variation used in the blade analysis with N = 200 and n = 100, the left-hand tail distribution of simulated failures was essentially the same as for a single-loop simulation with N = 20,000 and n = 1. The blade results presented in Section 3.3.4 were obtained using N = 20,000 and n = 1.

The driver transformation and the fatigue life calculation used in the blade LCF failure simulation are shown in Figure 3.2-9. The driver transformation, shown in

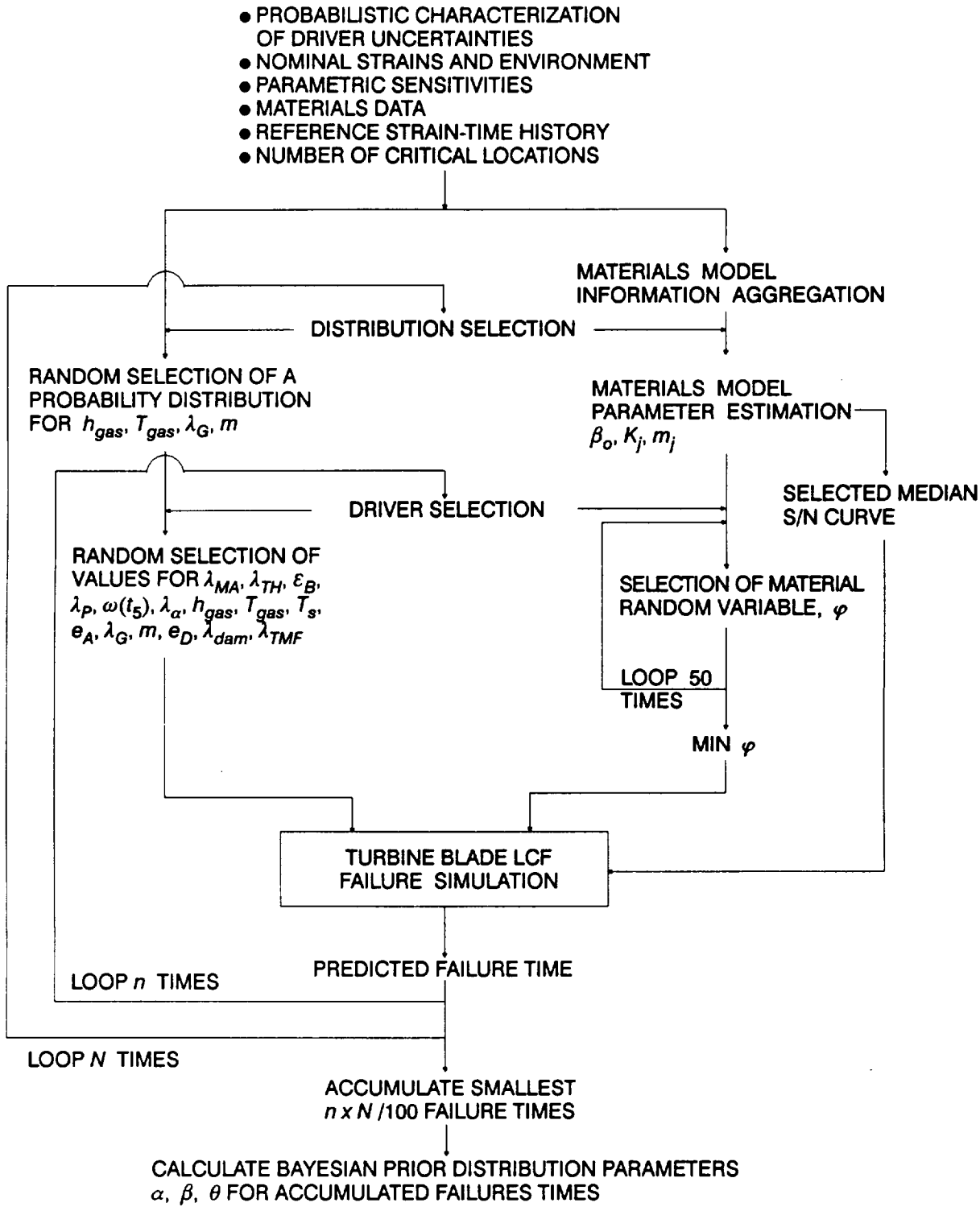

Figure 3-2.8 Structure of the Probabilistic Failure Model

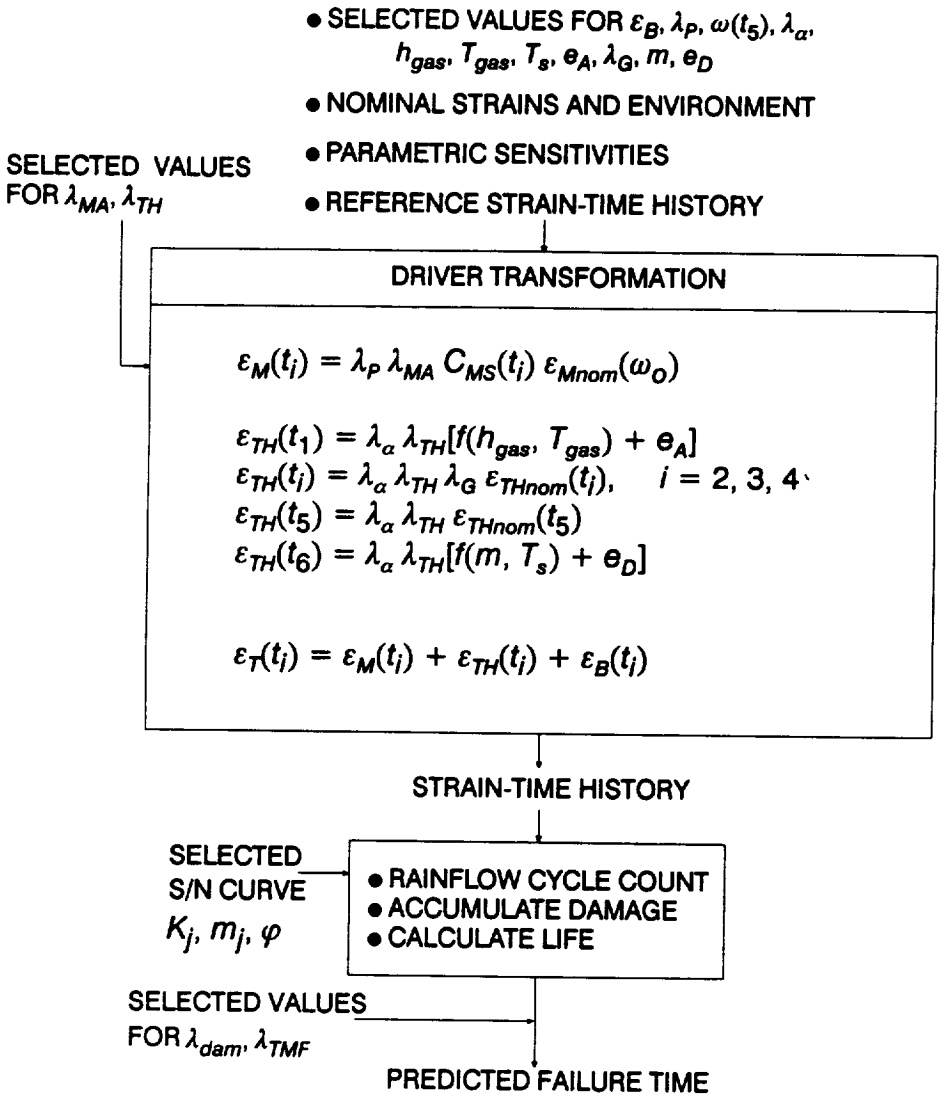

Figure 3.2-9 Structure of the Turbine Blade LCF Failure Simulation

Table 3.2-2 Driver Distributions and Influences for ATD-HPFTP First Stage Turbine Blade LCF

	t_1	t_2	t_3	t_4	t_5	t_6	LIFE	DISTRIBUTION
ε_B	X	X	X	X	X	X		Uniform
λ_P	X	X	X	X	X	X		Uniform
λ_{MA}	X	X	X	X	X	X		Uniform
$\omega(t_5)$					X			Normal
λ_α	X	X	X	X	X	X		Uniform
λ_{TH}	X	X	X	X	X	X		Uniform
h_{gas}	X							Beta
T_{gas}	X							Beta
m						X		Beta
λ_G		X	X	X				Beta
T_s						X		Normal
e_A	X							Normal
e_D						X		Normal
λ_{dam}							X	Uniform
λ_{TMF}							X	Uniform

Equation 3-1, is performed in several steps. First, the thermal stress during acceleration is calculated using the acceleration model of Equation 3-2. Next, the deceleration model calculations are performed, Equations 3-3, 3-6, and 3-7, the deceleration slope, thermal strain, and rotor speed are obtained. The total mechanical and total thermal strain-time histories are calculated using Equations 3-5 and 3-4, respectively. Then, the composite strain-time history is obtained by combining the thermal and mechanical strains according to Equation 3-1. Finally, the rainflow cycle counting and damage accumulation is performed. The predicted failure time is then obtained using the randomly selected S/N curve from the materials characterization model.

The probability distributions characterizing driver uncertainty in the blade PFM are summarized in Table 3.2-2. The values of h_{gas}, T_{gas}, m, and λ_G are characterized by Beta distributions with the capability for assigning Uniform distributions on the hyperparameters, ρ and θ. In the blade simulation, ρ and θ were fixed at specific values, so no hyperdistributions were used. Steady-state turbopump speed $\omega(t_5)$, deceleration starting temperature T_s, and the additive model accuracy

factors e_A and e_D are considered to be Normally distributed with fixed mean and variance. The bending strain ε_B and the factors λ_P, λ_{MA}, λ_α, λ_{TH}, λ_{dam}, and λ_{TMF} are represented by Uniform distributions with fixed end points. The specific distributions for all drivers are discussed in Section 3.3.1. Table 3.2-2 also gives the time t_i, $i = 1, ..., 6$ at which each driver influences the driver transformation.

Section 3.3
Turbine Blade Case Study

3.3.1 Driver Description

The list of drivers used in the blade LCF analysis, their distributions, and parameters are given in Table 3.3-1. This list includes six drivers which account for accuracy of the analysis.

Beta distributions were used to characterize the gas film coefficient during acceleration, h_{gas}, the gas temperature during acceleration, T_{gas}, λ_G, the uncertainty about start transient thermal strain extrema for time t_i, $i = 2, 3, 4$, and the deceleration slope, m. However, the parameters of the distribution were set such that m does not vary in the blade LCF analysis. A Beta distribution can be parameterized as Beta(a, b, ρ, θ) where a and b are the lower and upper bounds, respectively, of the range of the random variate, ρ is a location parameter, and θ is a shape parameter. See [1], Section 2.1.3.1, for a more detailed description of this parameterization of the Beta distribution. Choosing $\theta = 0$ in the Beta distribution is equivalent to assigning a Uniform distribution between a and b.

The gas film coefficient during acceleration is expected to vary over the range 676 Btu/ft^2·hr to 2730 Btu/ft^2·hr. The bounds are based on Pratt & Whitney's engineering analyses of the heat transfer phenomena during the start transient. The lower bound is the nonaugmented h_{gas} without turbulence. The upper bound is the augmented h_{gas} with turbulence during the start transient.

The gas temperature during acceleration T_{gas} is bounded by a scatter band of ±600° about the nominal value. The nominal value of 1382°R is based on test data. The uncertainty for the start transient thermal strain extrema λ_G for time t_i, $i = 2, 3, 4$ was assessed to be ±50%, based on the gas temperature sensitivity of the acceleration model response surface for thermal strain.

A meaningful measurement of the true deceleration slope must be based on data from fast response temperature probes. At the time this analysis was performed, only a limited amount of data from fast response temperature probes was available. This data consisted of temperature histories from six to ten functioning probes taken during two engine tests. The probes were arranged circumferentially in the preburner ahead of the turbine. The issue arises as to whether the probe-to-probe variation represents true circumferential variation or measurement error of the fast response probes. In the absence of information about the shutdown-to-

Table 3.3-1 Driver Distributions for ATD-HPFTP First Stage Turbine Blade LCF

DRIVER	DISTRIBUTION	NOMINAL
Hot gas film coefficient during acceleration, h_{gas}	Beta(676, 2730, 0.5, 0)	1703
Hot gas temperature during acceleration, T_{gas}	Beta(782, 1982, 0.5, 0)	1382
λ_G, the uncertainty for start transient thermal strain extrema for t_i, i = 2, 3, 4	Beta(0.5, 1.5, 0.5, 0)	1.0
Deceleration slope, m	Beta(2730, 2730, 0.5, 0)	2730
Rotor speed at steady state, $\omega(t_5)$	Normal $(37592, 507^2)$	37592
Acceleration response surface accuracy factor, e_A	Normal $(0, 0.02^2)$	0
Deceleration response surface accuracy factor, e_D	Normal $(0, 0.003^2)$	0
Gas temperature at start of deceleration, T_s	Normal $(1640, 40.67^2)$	1640
Bending strain, ε_B	Uniform(0, 0)	0
Variation in blade pull due to variation in blade mass, λ_P	Uniform(0.96, 1.04)	1.0
Mechanical strain analysis accuracy factor, λ_{MA}	Uniform(0.8, 1.2)	1.0
Variation in coefficient of thermal expansion, λ_α	Uniform(0.975, 1.025)	1.0
Thermal strain analysis accuracy factor, λ_{TH}	Uniform(0.7, 1.3)	1.0
Damage accumulation model accuracy factor, λ_{dam}	Uniform(ln 1, ln 1)	ln 1
Thermal-mechanical fatigue accuracy factor, λ_{TMF}	Uniform(ln 1, ln 1)	ln 1

shutdown and engine-to-engine variability of the deceleration slope, its value was fixed at 2730 °R/sec, which bounds the steepest slope observed in the available data.

The steady state rotor speed $\omega(t_5)$ is distributed according to a Normal distribution about the nominal rotor speed of 37,592 rpm with a standard deviation of 507 rpm. This characterization is based on an analytical turbopump performance model.

The acceleration response surface accuracy factor, e_A, and the deceleration response surface accuracy factor, e_D, are additive modeling uncertainties and are Normally distributed about a nominal value of 0. The standard deviation characterizes the goodness of fit of each function or response surface. The standard deviations for e_A and e_D are .02 and .003, respectively.

The gas temperature at the start of deceleration, T_s, is distributed according to a Normal distribution about the nominal temperature of 1640°R with a standard deviation of 40.67°R. This characterization is based on test data.

The bending strain, ε_B, accounts for strain due to gas bending and blade tilt bending. However, in the design being analyzed here, the tilt bending strain of the blade was adjusted to counteract the gas bending strain so that the net strain at full power is negligible. Hence, the nominal ε_B is zero and no variability was modeled.

The factor λ_P accounts for the variation in blade pull due to variation in blade mass resulting from the allowed manufacturing tolerance in blade mass. The tolerance in blade mass is ±4%. λ_P was characterized by a Uniform distribution over the range (.96, 1.04).

The mechanical strain analysis accuracy factor λ_{MA} accounts for uncertainty of the finite element (FE) analysis. A review of FE literature and discussions with stress analysts who have compared analysis and tests indicate that a correct FE strain analysis would calculate strains to within 20% of the true value. Thus λ_{MA} was represented as a Uniform distribution over the range (.80, 1.20).

The factor λ_α accounts for variability of the coefficient of thermal expansion. The measured variability in α for PWA 1480 is ±2.5%. λ_α was represented by a Uniform distribution over the range (.975, 1.025).

The thermal strain analysis accuracy factor λ_{TH} accounts for uncertainty of the blade thermal analysis, which includes modeling accuracy, and variabilities of blade wall thickness, thermal conductivity, and specific heat. Discussions with designers and analysts indicate that the thermal analysis predicts strains to within 30% of the true value. λ_{TH} was represented by a Uniform distribution over the range (.70, 1.30).

Damage accumulation inaccuracies are not significant in this analysis because damage is due to only two cycles, wherein the larger cycle causes virtually all the damage. The damage accumulation accuracy factor λ_{dam} is a multiplier on life. Since inaccuracy is not significant in this case, the value of the accuracy factor is 1

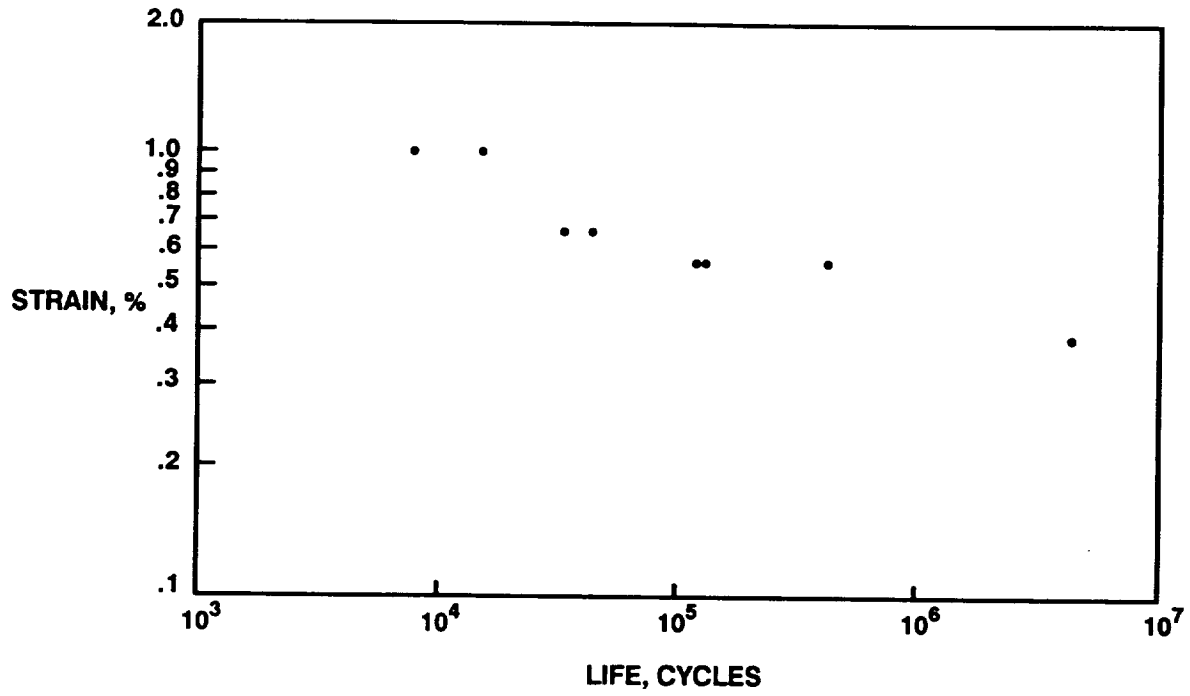

Figure 3.3-1 PWA 1480 Fatigue Data

in linear space. The life computation is performed in logarithmic space; hence, λ_{dam} was fixed at ln(1). This is accomplished by setting the upper and lower bounds of the Uniform distribution for λ_{dam} at zero.

The thermal-mechanical fatigue accuracy factor λ_{TMF} accounts for fatigue life prediction errors due to inadequate modeling of thermal-mechanical interactions. The thermal-mechanical fatigue accuracy factor is a multiplier on life. Since the S/N data used for the blade being analyzed was for a constant temperature, but believed to be a lower bound on life and therefore conservative, the value of the accuracy factor is 1 in linear space. The life computation is performed in logarithmic space; hence λ_{TMF} was fixed at ln(1). This is accomplished by setting the upper and lower bounds of the Uniform distribution for λ_{TMF} at zero.

3.3.2 Materials Characterization

The ATD-HPFTP turbine blades are made of the single crystal material PWA 1480. In tests performed by Pratt & Whitney, eight test specimens of this material were subjected to stress controlled cyclic loading at 20 Hz at a stress ratio of $R = -1.0$ in the [001] crystal orientation. The fatigue tests were performed in 5000 psig hydrogen at room temperature [11]. The eight fatigue life data points are shown in Figure 3.3-1. Since the blade material essentially behaves elastically in this application, stress values were linearly transformed to equivalent strain range values.

3.3.3 Analysis

The program BLDLCF implements the LCF failure model, the driver information, and the materials characterization models presented in the preceeding discussion, and it was used to perform the LCF analysis of the ATD-HPFTP first stage turbine blade. The blade materials variation was modeled using alternative Weibull and Lognormal distributions and with the parametric and bootstrapping materials models described in Section 3.2.7.

The overall description of program BLDLCF is given in Section 5.2. The user's manual for BLDLCF, including the description of the input variables, is given in Section 6.2. A source listing of BLDLCF is given in Section 7.2.

3.3.4 Results

The results of the failure simulations for the blade are given in Figure 3.3-2. The graph presents the left-hand tail of the failure distribution derived from the simulations. The ordinate of this graph is failure probability, and the abscissa is life of the blade to LCF failure. Life is taken as the worst of 50 blades and is given in missions. A mission is taken as one start transient and one shutdown transient as was shown in Figure 3.2-3.

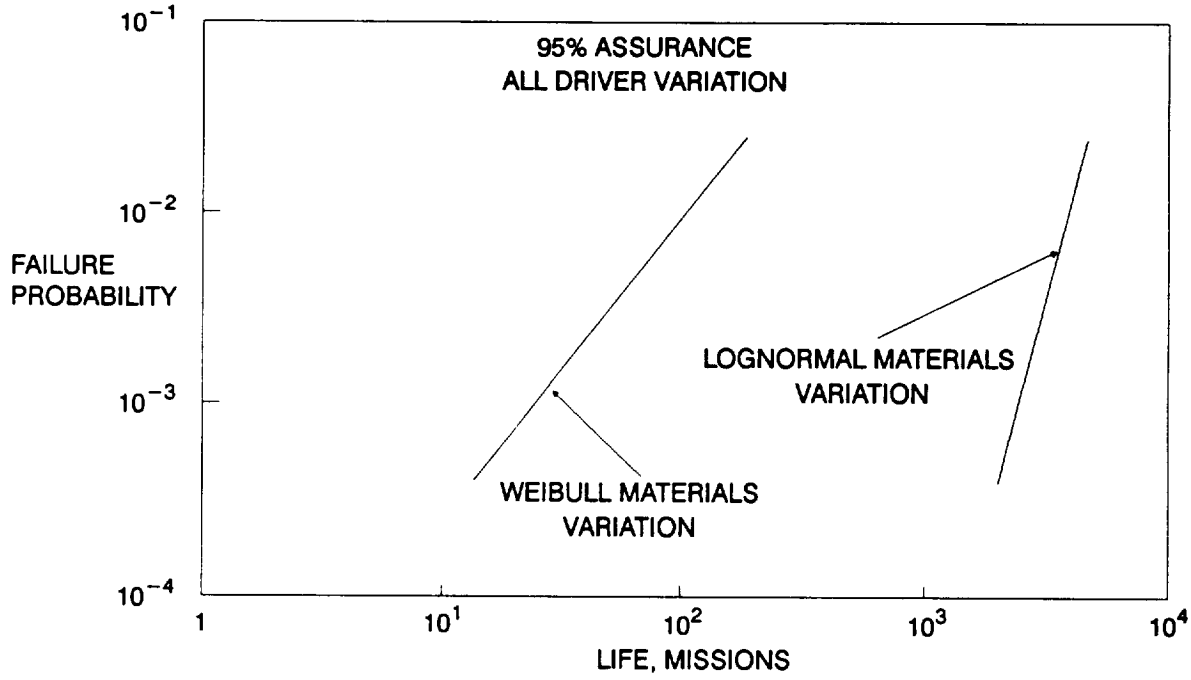

Figure 3.3-2 Impact of Materials Variation on Failure Life Distribution

Figure 3.3-2 shows blade LCF life at 95% assurance. The meaning of a 95% assurance curve is that the failure probability at a given failure life will lie with .95 probability below that curve. The left-hand curve is for Weibull materials variation. The B.1 life[5] at 95% assurance is 24 missions. The right-hand curve is for Lognormal materials variation and the B.1 life at 95% assurance is 2431 missions.

Figures 3.3-3 and 3.3-4 show the output of failure simulations conducted to assess the sensitivity of the turbine blade failure life distribution to the drivers. The curves of Figures 3.3-3 and 3.3-4 represent the direct output of the Monte Carlo simulation. Figure 3.3-3 is the failure simulation using Weibull materials variation and Figure 3.3-4 is the failure simulation using Lognormal materials variation. The right-most curve labeled "nominal" in both figures is for a simulation which included intrinsic materials variation only (see [1], Section 2.1.2.1); all the other drivers were fixed at their nominal or most likely values. The left-most curve in each figure is the "all driver variation" curve. The input and output files from the "all driver" analysis for Weibull materials variation are given in Section 3.B. A measure of the relative importance of individual drivers is given in the upper left corner in both figures. These were obtained by finding the marginal effects of driver uncertainties on B.1 lives by using several sensitivity runs, where one driver was allowed to vary while the rest were held at their nominal values. The S/N model parameters and thermal analysis accuracy λ_{TH} were the most significant drivers in this analysis with a combined 92% contribution to the decrease from nominal B.1 life for Weibull materials variation and a combined 93% contribution to the decrease from nominal B.1 life for Lognormal materials variation. The middle curve in both figures shows the shift to the left due to variation only in the S/N model parameters and thermal analysis accuracy. Variations in all other parameters are not important drivers.

Figure 3.3-5 can be used to demonstrate the effect of alternative materials models on estimated failure probability curves. Both curves are for "all driver variation," Weibull materials variation, and 95% assurance. The left-most curve is for a failure simulation using the parametric model of [1], Section 2.1.2, and the right-most curve is for a bootstrap model of materials variation. Table 3.3-2 summarizes the B.1 lives from Figure 3.3-5 for Weibull materials variation and gives the B.1 lives for Lognormal materials variation which are not plotted in Figure 3.3-5. It demonstrates the need for ascertaining the appropriate statistical model for materials variability.

---

[5] A B-life is the value of accumulated operating time to failure at a failure probability specified as a percent; e.g., B.1 is the failure time at a probability of 0.001 or 0.1%.

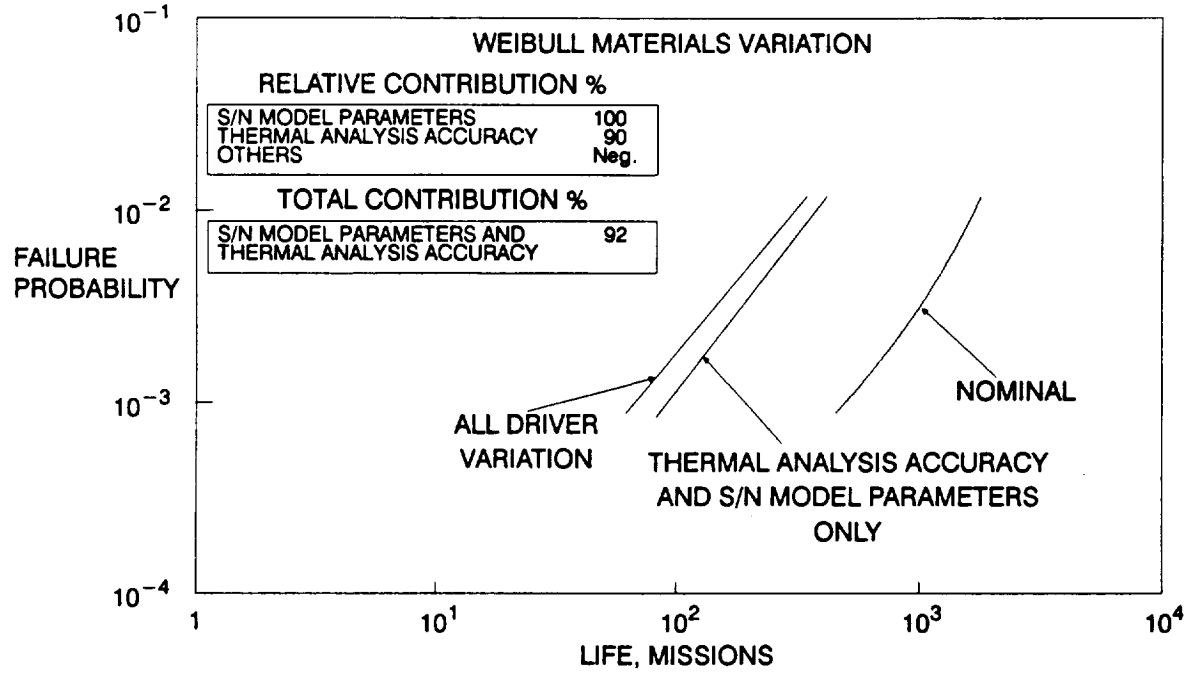

Figure 3.3-3 Driver Sensitivities for Weibull Materials Variation

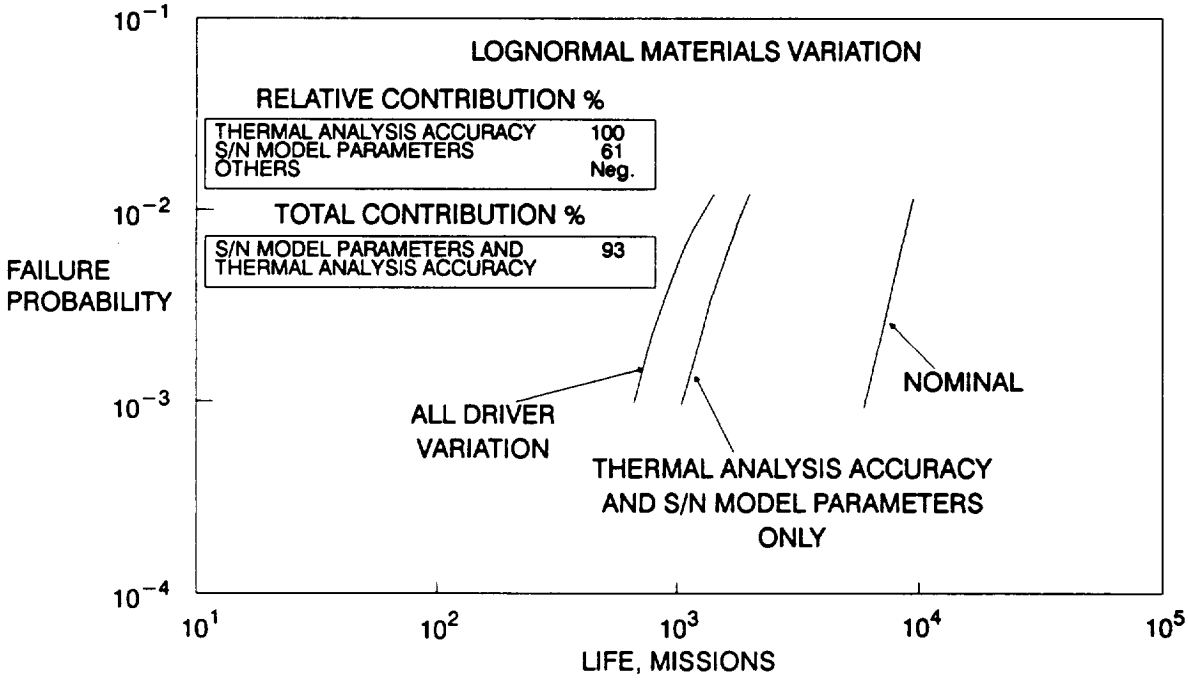

Figure 3.3-4 Driver Sensitivities for Lognormal Materials Variation

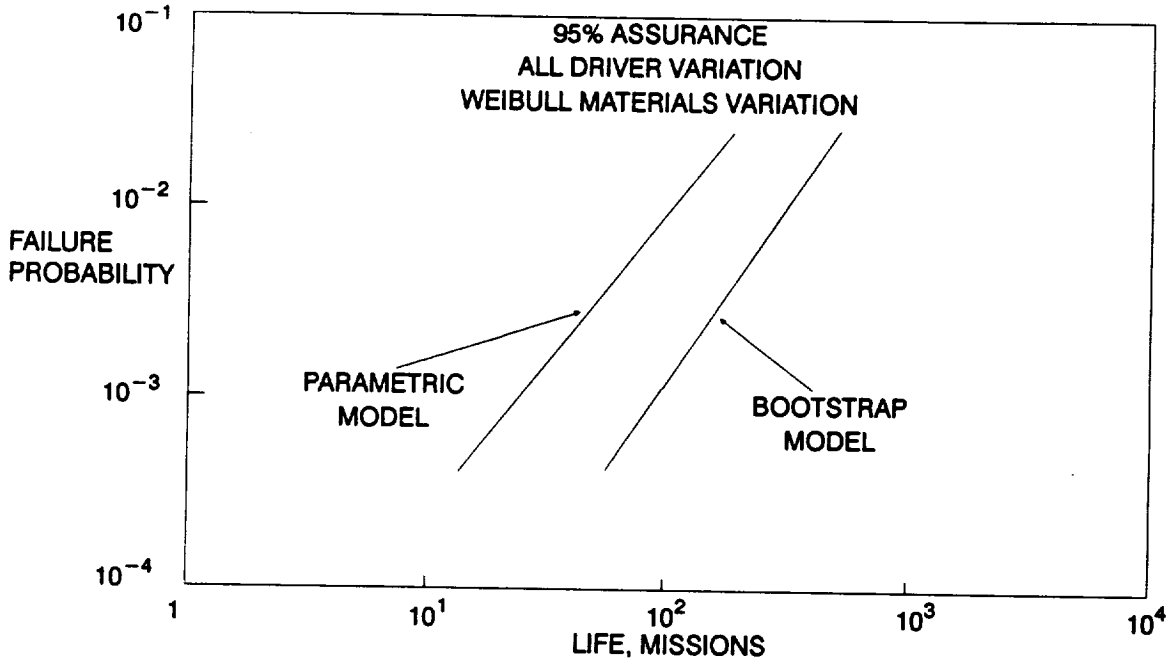

Figure 3.3-5 Impact of Materials Variation Parameterization on Failure Life Distribution

Table 3.3-2 B.1 Life (missions) at 95% Assurance for All Driver Variation

	Parametric	Bootstrapping
Weibull	24	91
Lognormal	2431	2543

Acquisition of additional materials data will reduce S/N model parameters uncertainty. A more accurate specification of the thermal analysis will reduce thermal analysis accuracy factor uncertainty. Additional materials data or exogenous evidence is required to choose between Weibull and Lognormal materials variation or discover some other appropriate statistical model for materials variability. Bootstrapping should be used to account for S/N model parameter uncertainty since it is less conservative than the parametric method and an adequate bootstrapping database is available.

Section 3.4
Analysis Procedure

The procedure used in carrying out the Probabilistic Failure Assessment (PFA) for low cycle fatigue failure of the ATD-HPFTP first stage turbine blade is given in detail in the following. Each step of the procedure, including intermediate calculations and results, is presented. The general procedure for applying the PFA methodology is given in Section 2.3 of [1].

3.4.1 Selecting the Component, Failure Mode, and Critical Location

The failure mode and critical location for the turbine blade were identified by deterministic analyses performed during the design process. Consistently conservative deterministic LCF analyses did not yield an acceptable service life estimate; consequently, it was deemed appropriate to apply the PFA methodology to evaluate LCF failure risk.

3.4.2 Preliminary Deterministic Analysis

The strain, thermal, and fluid flow analyses performed by Pratt & Whitney were used to identify drivers and in formulating the driver transformation for the PFA. These analyses included the following steps:

1. Establish thermal boundary conditions for the turbine blade during start and shutdown transients using thermal and fluid flow models.
2. Use "blade pull" model to obtain the mechanical strain due to rotor speed and blade mass.
3. Perform 2-D MARC FE analysis with nominal thermal boundary conditions during acceleration to obtain total strain due to thermal gradients and mechanical loads.
4. Perform eight 1-D MARC FE analyses perturbing the gas temperature and film coefficient to characterize sensitivity of blade thermal strain.
5. Subtract the mechanical strain of (2) from the 9 total strains of (3) and (4) to obtain a matrix of 9 thermal strains as a function of gas temperature and gas film coefficient. The matrix is shown in Table 3.4-1.
6. Fit the results of (5) to a response surface [2-7] using RSREG.[6] This response surface characterizes the thermal strain during acceleration and is given by Equation 3-2.

---

[6] Routine RSREG fits the parameters of a quadratic response surface, and is described in Chapter 37 of [12].

Table 3.4-1 Matrix of Thermal Strains as a Function of Gas Film Coefficient and Gas Temperature During Acceleration

ε_{TH}		h_{gas}		
		676	1703	2730
T_{gas} (R)	800	0	−.078	−.1039
	1382	−.0427	−.0954	−.1421
	2000	−.0673	−.1577	−.2381

Table 3.4-2 Values of Thermal Strain for Varying Values of Temperature and Slope During Deceleration

m (°R/sec)	ε_{TH} (%)	t_d (sec)	ω (rpm)
1368	.2039	.727	19,429
1700	.2345	.657	19,782
2730	.301	.504	21,345.1
3700	.3452	.423	23,146.3
4700	.3759	.377	23,957.3

7 Characterize the temperature profile during shutdown using SSME engine test data to obtain gas temperature prior to the shutdown transient and slope (°R/sec) of gas temperature versus time curve.

8 Perform 1-D analyses to obtain sensitivity of thermal strain to gas temperature and slope.

9 Fit the results of (8) to a response surface [2-7] using RSREG. This response surface characterizes the thermal strain during deceleration. The results of (8) are shown in Table 3.4-2 and characterized by Equations 3-3, 3-6, and 3-7.

3.4.3 Driver Characterization

The list of drivers for the turbine blades, their distributions, and ranges are given in Table 3.3-1. The rationale for assigning the distributions for these drivers was presented in Section 3.3.1.

3.4.4 Materials Characterization

As described in Section 3.3.2, PWA 1480 S/N material data was used for the turbine blades. The data is given in Table 3.4-3 and is shown in Figure 3.3-1. A

Table 3.4-3 PWA 1480 S/N Data

STRAIN S (psi)	LIFE N (cycles)
.89	6,800
.89	15,000
.67	27,000
.67	43,200
.56	139,300
.56	545,200
.56	147,000
.39	4,344,800

Table 3.4-4 Summary of Materials Characterization Study of PWA 1480 Data

	Coefficient of Variation C	Slope Parameter m
95% Confidence Interval	{0.054, 0.186}	{5.15, 9.56}
Point Estimates	0.084	7.36
Posterior Credibility Range Lower bound Upper bound	—	 5.15 9.56

single data region, see [1] Section 2.1.2.1, was used since a single, linear ln(S) versus ln(N) curve represents the fatigue life data in the life ranges of interest.

Program MATCHR, see [1] Section 4.1, was used to define statistical parameters of the fatigue life data shown in Figure 3.3-1. Table 3.4-4 shows the 95% confidence intervals for the coefficient of variation C and the slope m that were obtained from MATCHR for the PWA 1480 data.[7] Point estimates for C and m are also given in the table. These point and interval estimates of C and m are consistent with expectations for this material, so no exogenously defined constraints on C and m were applied.

[7] See Equations 2-24 and 2-26 of [1].

3.4.5 Time History Definition

The time history used for the turbine blades is described in Section 3.2.3 and shown in Figure 3.2-3.

3.4.6 Probability of Failure Curve Parameter Estimation

The steps required to carry out the probability of failure curve parameter estimation for this blade example are given in Figure 3.4-1 This procedure was used to obtain the results discussed in Section 3.3.4.

The parameters of the prior distribution are estimated by determining a value for β, then estimated α and θ for fixed β. The first step in the procedure is to plot the failure simulation results contained in file LOWLIF for the "all drivers" run. That plot is shown in Figure 3.3-3.

The β estimate is based on an approximate linear portion of the left-hand tail (.001 to .01 on the ordinate) for this example. This probability range corresponds to simulated lives with index numbers 20 through 200, inclusive, in file LOWLIF. A value for β is estimated by program BFIT. The pertinent methodology is discussed in [1], Section 2.1.1, the program description and flowcharts are presented in [1], Section 4.2.2, the user's guide for running this program is given in [1], Sections 6.4.1 through 6.4.6, and the code structure and listing are provided in [1], Section 7.4.1. Program BFIT has provided the estimate $\beta = 1.582$ for this example.

The α and θ estimate must be based on an extension of the data used to estimate β in order to fit a model which is nonlinear in log–log space. It is only necessary to consider points with probability in the range .001 to .01. α, θ are estimated by the program ABTFIT. The pertinent methodology is discussed in [1], Section 2.1.1, the program description and flowcharts are presented in [1], Section 4.2.3, the user's guide for running this program is given in [1], Sections 6.4.7 through 6.4.12, and the code structure and listing are provided in [1], Section 7.4.2.

1 Plot the failure simulation results contained in file LOWLIF in log–log space. That plot is shown in Figure 3.3-3.

2 Since the curve in Figure 3.3-3 from probability of .001 to .01, that is, point 20 to point 200 of file LOWLIF, is approximately linear, it can be used to estimate β.

3 Create file BFITD to indicate the indices of the LOWLIF data to be used in the β estimation. See [1], Section 6.4.3.1 for a detailed description of the contents of file BFITD.

4 Run program BFIT. The pertinent methodology is discussed in [1], Section 2.1.1; the program description and flowcharts are presented in [1], Section 4.2.2; the user's guide for running this program is given in [1], Sections 6.4.1–6.4.6; and the code structure and listing are provided in [1], Section 7.4.1. BFIT has two input files, LOWLIF and BFITD, and two output files, BFITO and IOUTPR.

5 Obtain β estimate from output files BFITO and IOUTPR. Program BFIT has provided the estimate of 1.582.

6 In order for α and θ to be uniquely determined, it is only necessary to consider the range .001 to .01, that is, point 20 to point 200 inclusive, of file LOWLIF, for the estimated curve to be nonlinear in log–log space. Create file PARAMS to indicate the indices of the LOWLIF data to be used in the α, θ estimation, the initial values for α and θ, and any scaling factors required. See [1], Section 6.4.9.1 for a detailed description of the contents of file PARAMS.

7 Run program ABTFIT. The pertinent methodology is discussed in [1], Section 2.1.1; the program description and flowcharts are presented in [1], Section 4.2.3; the user's guide for running this program is given in [1], Sections 6.4.7–6.4.12; and the code structure and listing are provided in [1], Section 7.4.2. ABTFIT has two input files, LOWLIF and PARAMS, and three output files, ABTOUT, BAYESD and IOUTPR.

8 Obtain α, θ estimates from output files ABTOUT and BAYESD. Program ABTFIT has provided the values 1.411×10^5 for θ and .1666 for α.

9 Calculate assurance based on estimates of α, β, θ. The assurance calculation is performed by program LZERO. The pertinent methodology is discussed in [1], Section 2.1.1; the program description and flowcharts are presented in [1], Section 4.2.4; the user's guide for running this program is given in [1], Sections 6.4.13–6.4.18; and the code structure and listing are provided in [1], Section 7.4.3.

Figure 3.4-1 Steps of the Probability of Failure Curve Parameter Estimation

PARAMS requires initial values[8] for α and θ that were obtained as follows:

B.1[9] = 69.3627

B1 = 314.683

LSCALE[10] = (1/314.683) ≈ .01

$\theta_o = N_{.001}^{\beta} = (69.3627)^{1.5816} = 816.4$

$\mathbf{XGUESS(1)}^{11} = \left(N_{.001} * \mathbf{LSCALE}\right)^{\beta} = \left(69.3627 \times 10^{-2}\right)^{1.5816} = .5607$

XGUESS(2) = α_o = − ln .999 / ln 2 = .0014434

Program ABTFIT has provided the estimates $\theta = 1.411 \times 10^5$ and $\alpha = .1666$.

3.4.7 Driver Sensitivity Analysis

As described in Section 2.3.10 of [1], a set of simulations was executed to obtain the driver sensitivities. The first simulation was the nominal run, which included intrinsic materials variation only (see [1], Section 2.1.2.1); all the other drivers were fixed at their nominal or most likely values. Figure 3.3-3 shows the output of the nominal simulation for the turbine blades. The next analysis was the "all driver" variation analysis, which was performed allowing all the drivers to vary. Figure 3.3-3 shows the output of the all-driver run for the turbine blades.

Finally, the driver sensitivities were derived using simulations for which each driver (together with intrinsic material variation) was allowed to vary one at time while all the other drivers were held at their nominal values. The output from these simulations along with the results from the aforementioned all-driver variation and nominal runs allow the drivers to be rank ordered and allow their relative importance to be characterized. The impact of the drivers was calculated based on the failure lives at the .01 probability level, given in Table 3.4-5, for the all-driver, nominal, and driver sensitivity runs for Weibull materials variation.

---

[8] The calculation of initial values is illustrated in [1], Section 6.4.11.

[9] B-lives were obtained from file LOWLIF. A B-life is the value of the failure parameter (e.g., failure time) at a failure probability specified as a percent: e.g., B.1 is the failure time at a probability of .001 or .1%.

[10] Life scaling factor is described in [1], Section 6.4.9.

[11] Calculation of initial guesses is described in [1], Section 6.4.11.

Table 3.4-5 Driver Sensitivity Analysis for the Turbine Blade for Weibull Materials Variation

Driver Variation In Analysis	B.1 Life (missions)	Shift From Nominal Curve	% Shift From All Drivers Curve	Relative Importance
Nominal	514			
All Drivers	69	445		
S/N Model Parameters	229	285	64	100
λ_{TH}	258	256	58	90
λ_G	453	62	13.9	21.8
T_s	456	58	13.0	20.4
λ_{MA}	492	22	4.9	7.7
e_D	503	11	2.5	3.9
λ_α	508	6	1.3	2.1
λ_P	511	3	.7	1.1
$\omega(t_5)$	514	0	0	0
h_{gas}	514	0	0	0
T_{gas}	514	0	0	0
e_A	514	0	0	0

To calculate the relative importance of a driver, the change in life from the nominal analysis due to driver variation was first calculated as a percentage of the shift due to the all driver variation, for each driver. The largest shift was caused by variation in S/N model parameters, which is therefore the most important driver. The relative importance was derived by normalizing the percentage shifts due to variation of each driver with the percentage shift due to variation of the most important driver, in this case S/N model parameters. Table 3.4-5 gives the percentage shift in lives and relative importance for each driver.

3.4.8 Probability of Failure Curve Standardization

In order to standardize the results, the probability of failure vs. life curves were generated for a given assurance level of 95% using the program LZERO. The pertinent methodology is discussed in [1], Section 2.1.1, the program description and flowcharts are presented in [1], Section 4.2.4, the user's guide for running this program is given in [1], Sections 6.4.13 through 6.4.18, and the code structure and listing are provided in [1], Section 7.4.3. The value of λ_o for the turbine blades for Weibull materials variation was 6.359×10^{-6}. Given λ_o and the bounding value of β, the assurance curve may be defined as described in Section 2.3.12 of [1]. The 95% assurance curve for the turbine blades is given in Figure 3.3-2.

References

[1] Moore, N., et al., An Improved Approach for Flight Readiness Certification – Methodology for Failure Risk Assessment and Application Examples, JPL Publication 92-15, Jet Propulsion Laboratory, California Institute of Technology, Pasadena, California, June 1, 1992.

[2] Box, George E. P., Hunter, William G., and Hunter, J. Stuart, Statistics for Experimenters, John Wiley & Sons, New York, New York, 1978.

[3] Cornell, John A., "How to Apply Response Surface Methodology," The ASQC Basic References in Quality Control: Statistical Techniques, Vol. 8, American Society for Quality Control, Milwaukee, Wisconsin, 1990.

[4] Hicks, Charles R., Fundamental Concepts in the Design of Experiments, Third Edition, Saunders College Publishing, Fort Worth, Texas, 1982.

[5] Khuri, Andre I., and Cornell, John A., Response Surfaces, Marcel Dekker, Inc., New York, New York, 1987.

[6] Montgomery, Douglas C., Design and Analysis of Experiments, Third Edition, John Wiley & Sons, New York, New York, 1991.

[7] Snee, Ronald D., Hare, Lynne B., and Trout, J. Richard, Experiments in Industry, American Society for Quality Control, Milwaukee, Wisconsin, 1985.

[8] Doner, M., Bain, K. R., and Adams, J. H., "Evaluation of Methods for the Treatment of Mean Stress Effects on Low-Cycle Fatigue," Journal of Engineering for Power, Vol. 104, April 1982.

[9] Aleong, J., and Howard, D., "Bootstrapping Regression Equations," 1986 American Statistical Association Statistical Computing Section Proceedings.

[10] Abramowitz, M., and Stegun, I. A., editors, Handbook of Mathematical Functions, National Bureau of Standards, Applied Mathematics Series 55, Issued June 1964, Ninth Printing, November 1970 with corrections.

[11] Stinson, H., Personal Communication, Marshall Space Flight Center, January 20, 1989.

[12] "SAS/STAT User's Guide," Version 6, Fourth Edition, Volume 2, SAS Institute, Cary, NC, 1990.

Appendix 3.A
List of Symbols

a	Beta distribution range parameter
a	Uniform distribution range parameter
$\hat{a}$	estimated S/N curve location parameter
A	statistical assurance that reliability is at least as large as stated
A_j	S/N curve location parameter
b	Beta distribution range parameter
b	Uniform distribution range parameter
$Be(\cdot)$	Beta distribution function
C, C_o	coefficient of variation of fatigue strength
C_{MS}	speed variability correction factor
e	residual; $\underline{e}$ = residual vector in log space; e^* = bootstrapped residual
e_A	response surface accuracy for t_1
e_D	response surface accuracy for t_6
E	Young's modulus
f_A	response surface for the nominal thermal strain at t_1
f_{D1}	response surface for the nominal thermal strain at t_6
f_{D2}	response surface for the deceleration duration time
f_{D3}	response surface for the rotor speed at t_6
$F(\cdot)$	cumulative probability distribution function
h_{gas}	hot gas film coefficient at start-up
I_o	credibility range for coefficient of variation of fatigue strength
J_o	credibility range for an S/N curve shape parameter
K_j	S/N curve location parameter

m	deceleration slope at shutdown
m_j	S/N curve shape parameter
$MED(\cdot)$	median value
n	inner loop simulation trials
N	degrees of freedom parameter
N	outer loop simulation trials
N	fatigue life
N_i^*	fatigue life value for generated pseudo S/N data
N_j	size of the jth materials fatigue test data set
$N_{i,\,i+1}^*$	S/N curve life boundaries
$N(\cdot)$	Normal distribution function
R, R_o	component reliability
R	number of life regions used to represent an S/N curve
R	stress ratio = $\sigma_{min} / \sigma_{max}$; strain ratio = $\epsilon_{min} / \epsilon_{max}$
S	stress or total strain range
S_x^2, S_y^2	sample variance
S_{xy}	sample covariance
S/N	stress/life or strain/life
S_i^*	stress or strain value for generated pseudo S/N data
t_i	time
t_d	deceleration duration time
T	length of reference time history in missions
T_{gas}	hot gas temperature at start-up
T_s	hot gas temperature at start of deceleration
$U(\cdot)$	Uniform distribution function
$VAR(\cdot)$	Variance value
w	characteristic Walker exponent for a given material

$W(\cdot)$	Weibull distribution function
x	ln (*stress*) or ln (*strain*)
y	ln (*life*)
α	Gamma distribution parameter
α	thermal coefficient of expansion
β, β_o	Weibull distribution shape parameter
γ	Euler's constant, .577 . . .
$\Delta\varepsilon$	strain range; $\Delta\varepsilon_{EQ}$ = equivalent strain range
ε	strain; ε_B = strain due to gas bending and blade tilt; ε_M = mechanical strain due to blade pull; ε_{max} = maximum strain; ε_{Mnom} = nominal mechanical strain at rotor speed ω_o; ε_T = total strain; ε_{TH} = thermal strain due to thermal gradient; ε_{THnom} = nominal thermal strain
ε	materials intrinsic variability
η_o	Weibull distribution scale parameter
θ	Gamma distribution parameter
θ	Beta distribution parameter
λ	accuracy or uncertainty factor; λ_{dam} = damage accumulation accuracy factor; λ_G = thermal strain uncertainty factor due to gas temperature variation during start-up; λ_{MA} = mechanical strain analysis accuracy factor; λ_P = deviation in blade pull load due to uncertainty in blade mass; λ_{TMF} = thermal-mechanical fatigue accuracy factor; λ_{TH} = thermal strain analysis accuracy factor; λ_α = coefficient of thermal expansion variation factor
λ, λ_o	Weibull distribution parameter
$\Lambda(\cdot)$	Lognormal distribution function
μ	Lognormal distribution parameter
μ	Normal distribution parameter
π	3.14159265 . . .
ρ	Beta distribution parameter
σ	stress
σ^2	Lognormal distribution parameter

σ^2	Normal distribution parameter
φ	materials intrinsic variability
$\chi^2(\cdot)$	Chi-square distribution function
ω	rotor speed; ω_o = nominal rotor speed

Appendix 3.B
Input And Output Files

Selected input and output files for the ATD-HPFTP first stage turbine blade "all driver" analysis for Weibull materials variation are given here. The analysis program BLDLCF requires two input files BLDLCD and RELATD. Annotated examples of the data file format for BLDLCD and RELATD input files are given in Figures 6.2-1 and 6.2-2. Related material data was not used for this component and hence the RELATD file was empty. The input file BLDLCD is given below. Section 6.2.3 contains a description of the input variables and a user's guide for running BLDLCF.

The output files from a BLDLCF run are BLDLCO, LOWLIF, DUMP, RELATO, and IOUTPR. The BLDLCO, LOWLIF, and DUMP files are given below for the Weibull materials variation failure simulation. The BLDLCO file contains an echo of the input data, output from the S/N material model, and the B-lives. The LOWLIF file contains the lowest 200 (1% of total simulated) fatigue failure lives for the blade; the failure lives are plotted in Figure 3.3-3. The DUMP file contains the results of the materials characterization calculations, including estimated values of the S/N curve parameters.

Input File - BLDLCD

```
675
0
1
20000
50
2
0
0
1
10
0.001  0.002  0.003  0.004  0.005  0.006  0.007  0.008  0.009  0.010
 676.   2730.   0.50   0.50   0.00   0.00
 782.   1982.   0.50   0.50   0.00   0.00
2730.   2730.   0.50   0.50   0.00   0.00
  0.5     1.5   0.50   0.50   0.00   0.00
5   37592.   507.
   0.0     0.020
1640.0    40.67
   0.0     0.003
0.00     0.00
0.96     1.04
0.80     1.20
```

```
 0.975     1.025
 0.70      1.30
 0.00      0.00
 0.00      0.00
 0.295
 38482.
 1.0
 0.0
 6
 0.50
 0.00727362    0.000067442    -0.000059109
      -3.52929E-08    1.07611E-08    -2.74419E-08
-0.132623     0.000227427    -0.000059290     0.00     0.00     4.71714E-08
 0.20         950.0
 30523.07   -21846.15
   225.8      0.0
  3025.1    -0.196921
  6138.8     0.146025
  8309.0    -0.200128
     0.0     0.007393
'RT, PWA 1480, 001 DIRECTION'
1.54     1.57     1    8
8    -1.0    1
0.89       6800.
0.89      15000.
0.67      27000.
0.67      43200.
0.56     139300.
0.56     545200.
0.56     147000.
0.39    4344800.
0.00
1  0
1.0E+36
0.00
0    0.000   0.000
```

Output File - BLDLCO

```
Copyright (C) 1990, California Institute of Technology.  U.S. Government
Sponsorship under NASA Contract NAS7-918 is acknowledged.


                                INPUT DATA

          DRIVERS                              PARAMETER DISTRIBUTIONS
```

		RHO	THETA
Hgas	Be(676., 2730.)	U(0.50000, 0.50000)	U(0.0, 0.0)
Tgas (deg R)	Be(782., 1982.)	U(0.50000, 0.50000)	U(0.0, 0.0)
DECEL SLOPE	Be(2730., 2730.)	U(0.50000, 0.50000)	U(0.0, 0.0)
Tgas UNCERT.	Be(0.50, 1.50)	U(0.50000, 0.50000)	U(0.0, 0.0)

	N(MEAN, STD. DEV.)
ROTOR SPEED VARIATION (rpm) AT TIME T5	N(37592.0, 507.0)
Faccel MODELING ERROR	N(0.0, 0.2000E-01)
STARTING DECEL TEMPERATURE (deg R)	N(1640.00, 40.67)
Fdecel MODELING ERROR	N(0.0, 0.3000E-02)

STRAIN DUE TO GAS BENDING (%)	U(0.00000, 0.00000)
LAMBDA BLADE PULL	U(0.96000, 1.04000)
MECHANICAL ANALYSIS FACTOR	U(0.80000, 1.20000)
COEFFICIENT OF THERMAL EXPANSION FACTOR	U(0.97500, 1.02500)
THERMAL ANALYSIS FACTOR	U(0.70000, 1.30000)

DAMAGE MODEL ACCURACY	U(ln 1.00000, ln 1.00000)
TMF MODEL ACCURACY	U(ln 1.00000, ln 1.00000)

OTHER STRAIN HISTORY INPUT

NOMINAL MECHANICAL STRAIN (%)	0.2950
NOMINAL ROTOR SPEED (rpm)	38482.
STRAIN-TIME HISTORY PERIOD (missions)	1.00
STRAIN-TIME HISTORY NOISE FILTER (%)	0.00000

NUMBER OF POINTS IN HISTORIES 6

WALKER EXPONENT 0.50

COEFFICIENTS OF ACCELERATION AND DECELERATION FUNCTIONS

THERMAL STRAIN AT STARTUP (%):

```
Faccel(Tgas, Hgas) =  0.727362E-02 +  0.674420E-04 * Tgas +
          -0.591090E-04 * Hgas + -0.352929E-07 * Tgas ** 2 +
           0.107611E-07 * Hgas**2 + -0.274419E-07 * Tgas * Hgas
```

THERMAL STRAIN AT SHUTDOWN (%):

```
Fdecel1(m, Tstart) = -0.132623E+00 +  0.227427E-03 * Tstart +
          -0.592900E-04 * m +  0.000000E+00 * Tstart ** 2 +
           0.000000E+00 * m ** 2 +  0.471714E-07 * Tstart * m
```

TIME AT SHUTDOWN (sec):

```
Fdecel2(m, Tstart) =  0.200000E+00 + (Tstart -  0.950000E+03 ) / m
```

ROTOR SPEED AT SHUTDOWN (rpm):

```
Fdecel3(t) =  0.305231E+05 + -0.218462E+05 * t
```

STRAIN HISTORY INFORMATION

ROTOR SPEED rpm	THERMAL STRAIN (%)
225.8	0.000000
3025.1	-0.196921
6138.8	0.146025
8309.0	-0.200128
0.0	0.007393

MATERIAL INPUT

DESCRIPTION: RT, PWA 1480, 001 DIRECTION

YIELD STRENGTH 0.15400E+01

ULTIMATE STRENGTH 0.15700E+01

NUMBER OF POINTS 8

ORIGINAL S/N STRESS	ORIGINAL S/N LIFE	STRESS RATIO	REGION	TRANSFORMED S/N STRESS	TRANSFORMED S/N LIFE
0.89000E+00	6800.	-1.00	1	0.89000E+00	6800.
0.89000E+00	15000.	-1.00	1	0.89000E+00	15000.
0.67000E+00	27000.	-1.00	1	0.67000E+00	27000.
0.67000E+00	43200.	-1.00	1	0.67000E+00	43200.
0.56000E+00	139300.	-1.00	1	0.56000E+00	139300.
0.56000E+00	545200.	-1.00	1	0.56000E+00	545200.
0.56000E+00	147000.	-1.00	1	0.56000E+00	147000.
0.39000E+00	4344800.	-1.00	1	0.39000E+00	4344800.

THERE IS 1 REGION(S) WITH DATA
AND 0 REGION(S) TO THE RIGHT WITHOUT DATA
THE UPPER BOUND(S) OF THE REGION(S) ARE (CYCLES):

0.100E+37

EXOGENOUS INFORMATION

CONSTRAINT ON COEFFICIENT OF VARIATION, C: 0.0000

EXPLICIT CONSTRAINT ON m FOR EACH REGION:

REGION	# OF POINTS	LOWER BOUND	UPPER BOUND
1	0	0.0000	0.0000

WEIBULL VARIATION

B LIVES:	EMPIRICAL
0.00100	0.693627E+02
0.00200	0.104496E+03
0.00300	0.141498E+03
0.00400	0.171753E+03
0.00500	0.203323E+03

0.00600	0.223266E+03
0.00700	0.244718E+03
0.00800	0.266518E+03
0.00900	0.286573E+03
0.01000	0.314683E+03
0.50000	0.900345E+04

Output File - LOWLIF

1	0.500000E-04	11.4674
2	0.100000E-03	20.5764
3	0.150000E-03	20.9020
4	0.200000E-03	23.3439
5	0.250000E-03	28.7136
6	0.300000E-03	33.3230
7	0.350000E-03	35.4286
8	0.400000E-03	37.5925
9	0.450000E-03	45.9977
10	0.500000E-03	50.0363
11	0.550000E-03	50.1602
12	0.600000E-03	50.6590
13	0.650000E-03	54.5432
14	0.700000E-03	54.9887
15	0.750000E-03	56.3990
16	0.800000E-03	57.8591
17	0.850000E-03	62.6331
18	0.900000E-03	65.5875
19	0.950000E-03	68.4943
20	0.100000E-02	69.3627
21	0.105000E-02	73.8416
22	0.110000E-02	74.9508
23	0.115000E-02	75.4585
24	0.120000E-02	78.1945
25	0.125000E-02	82.3033
26	0.130000E-02	84.9180
27	0.135000E-02	85.5436
28	0.140000E-02	87.7353
29	0.145000E-02	88.8890
30	0.150000E-02	93.2934
31	0.155000E-02	93.3853
32	0.160000E-02	96.0268
33	0.165000E-02	96.0511
34	0.170000E-02	96.3106
35	0.175000E-02	98.0476
36	0.180000E-02	99.5991
37	0.185000E-02	101.824
38	0.190000E-02	102.286
39	0.195000E-02	103.012
40	0.200000E-02	104.496

41	0.205000E-02	104.946
42	0.210000E-02	106.325
43	0.215000E-02	110.003
44	0.220000E-02	111.212
45	0.225000E-02	111.670
46	0.230000E-02	113.510
47	0.235000E-02	113.610
48	0.240000E-02	114.501
49	0.245000E-02	116.168
50	0.250000E-02	119.642
51	0.255000E-02	121.653
52	0.260000E-02	126.945
53	0.265000E-02	129.652
54	0.270000E-02	132.441
55	0.275000E-02	132.713
56	0.280000E-02	132.853
57	0.285000E-02	134.850
58	0.290000E-02	136.655
59	0.295000E-02	136.710
60	0.300000E-02	141.498
61	0.305000E-02	146.554
62	0.310000E-02	146.987
63	0.315000E-02	147.589
64	0.320000E-02	154.347
65	0.325000E-02	156.143
66	0.330000E-02	158.882
67	0.335000E-02	159.672
68	0.340000E-02	160.197
69	0.345000E-02	161.686
70	0.350000E-02	164.602
71	0.355000E-02	165.648
72	0.360000E-02	165.831
73	0.365000E-02	165.867
74	0.370000E-02	167.298
75	0.375000E-02	167.348
76	0.380000E-02	169.175
77	0.385000E-02	169.208
78	0.390000E-02	169.766
79	0.395000E-02	169.787
80	0.400000E-02	171.753
81	0.405000E-02	175.717
82	0.410000E-02	176.525
83	0.415000E-02	180.021
84	0.420000E-02	180.784
85	0.425000E-02	181.151
86	0.430000E-02	182.652
87	0.435000E-02	182.757
88	0.440000E-02	183.970
89	0.445000E-02	184.185
90	0.450000E-02	185.089

91	0.455000E-02	186.951
92	0.460000E-02	187.950
93	0.465000E-02	188.068
94	0.470000E-02	191.095
95	0.475000E-02	193.211
96	0.480000E-02	199.758
97	0.485000E-02	200.120
98	0.490000E-02	200.299
99	0.495000E-02	200.820
100	0.500000E-02	203.323
101	0.505000E-02	204.715
102	0.510000E-02	206.620
103	0.515000E-02	208.139
104	0.520000E-02	208.957
105	0.525000E-02	209.029
106	0.530000E-02	209.388
107	0.535000E-02	209.562
108	0.540000E-02	211.436
109	0.545000E-02	212.186
110	0.550000E-02	213.019
111	0.555000E-02	213.384
112	0.560000E-02	215.517
113	0.565000E-02	216.541
114	0.570000E-02	217.368
115	0.575000E-02	219.029
116	0.580000E-02	219.229
117	0.585000E-02	220.573
118	0.590000E-02	221.352
119	0.595000E-02	223.254
120	0.600000E-02	223.266
121	0.605000E-02	224.214
122	0.610000E-02	224.821
123	0.615000E-02	224.941
124	0.620000E-02	225.630
125	0.625000E-02	230.432
126	0.630000E-02	230.894
127	0.635000E-02	232.867
128	0.640000E-02	233.193
129	0.645000E-02	235.233
130	0.650000E-02	235.455
131	0.655000E-02	235.684
132	0.660000E-02	237.135
133	0.665000E-02	239.252
134	0.670000E-02	240.345
135	0.675000E-02	241.842
136	0.680000E-02	242.162
137	0.685000E-02	242.815
138	0.690000E-02	244.131
139	0.695000E-02	244.176
140	0.700000E-02	244.718

141	0.705000E-02	245.149
142	0.710000E-02	248.546
143	0.715000E-02	251.099
144	0.720000E-02	251.607
145	0.725000E-02	251.614
146	0.730000E-02	252.298
147	0.735000E-02	253.937
148	0.740000E-02	255.248
149	0.745000E-02	259.308
150	0.750000E-02	259.677
151	0.755000E-02	260.639
152	0.760000E-02	261.692
153	0.765000E-02	262.321
154	0.770000E-02	263.077
155	0.775000E-02	263.105
156	0.780000E-02	263.857
157	0.785000E-02	265.718
158	0.790000E-02	265.802
159	0.795000E-02	266.451
160	0.800000E-02	266.518
161	0.805000E-02	266.648
162	0.810000E-02	268.302
163	0.815000E-02	268.492
164	0.820000E-02	268.948
165	0.825000E-02	268.991
166	0.830000E-02	269.684
167	0.835000E-02	272.396
168	0.840000E-02	272.490
169	0.845000E-02	273.289
170	0.850000E-02	273.440
171	0.855000E-02	273.690
172	0.860000E-02	275.113
173	0.865000E-02	277.709
174	0.870000E-02	278.107
175	0.875000E-02	279.670
176	0.880000E-02	283.247
177	0.885000E-02	283.595
178	0.890000E-02	284.003
179	0.895000E-02	285.168
180	0.900000E-02	286.573
181	0.905000E-02	289.375
182	0.910000E-02	294.471
183	0.915000E-02	294.922
184	0.920000E-02	296.875
185	0.925000E-02	297.684
186	0.930000E-02	299.328
187	0.935000E-02	299.942
188	0.940000E-02	301.087
189	0.945000E-02	303.201
190	0.950000E-02	303.504

191	0.955000E-02	304.032
192	0.960000E-02	305.626
193	0.965000E-02	306.731
194	0.970000E-02	308.299
195	0.975000E-02	308.348
196	0.980000E-02	309.762
197	0.985000E-02	312.676
198	0.990000E-02	314.043
199	0.995000E-02	314.101
200	0.100000E-01	314.683

Output File - DUMP

RESULTS OF INFORMATION AGGREGATION CALCULATIONS

95% CONFIDENCE INTERVALS ON C AND m FOR EACH REGION

REGION: 1 Io = (0.054422790, 0.185977300)
Jo = (5.152009000, 9.564463000)

POINT ESTIMATES OF C AND m FOR EACH REGION

REGION	E(C)	E(m)
1	0.084455910	7.358236

POSTERIOR CREDIBILITY RANGE ON m FOR EACH REGION

REGION	LOWER BOUND	UPPER BOUND
1	5.1520	9.5645

PARAMETER VALUES FOR MEDIAN S/N CURVE

NUMBER OF REGIONS: 1 E(BETAo) = 15.7104 E(k) = 1.0909

REGION	m	K	LIFE BOUND	STRESS BOUND
1	7.35824	0.30172E+01	0.100E+37	0.00000E+00

4.0 Probabilistic Modeling of Turbine Blade High Cycle Fatigue Failure

Section 4.1
Introduction

A High Cycle Fatigue (HCF) failure model calculates the crack initiation life of a structure subjected to a large number of low amplitude load cycles. As shown in Figure 4.1-1, the information used in the HCF failure model presented here includes values of such drivers as environmental parameters, loads, material properties, structural parameters, and uncertainties about driver values and engineering model accuracy. The available information about drivers, including their uncertainties, is used to synthesize stress histories. Individual cycles of stress histories are characterized by a value of equivalent stress that accounts for the mean and extrema of each cycle. The materials characterization model establishes a value of fatigue life for the equivalent stress of each cycle. The fatigue life for a stress history is computed from the accumulated damage due to a sequence of individual cycles.

The application of the Probabilistic Failure Assessment methodology to HCF failure of the first and third stage turbine blades of the ATD-High Pressure Oxidizer Turbo Pump (HPOTP) is described in the following. The turbine blade fatigue analysis and implementation of the failure simulation model are discussed in detail. In this model, the stress history consists of constant amplitude stress cycles; con-

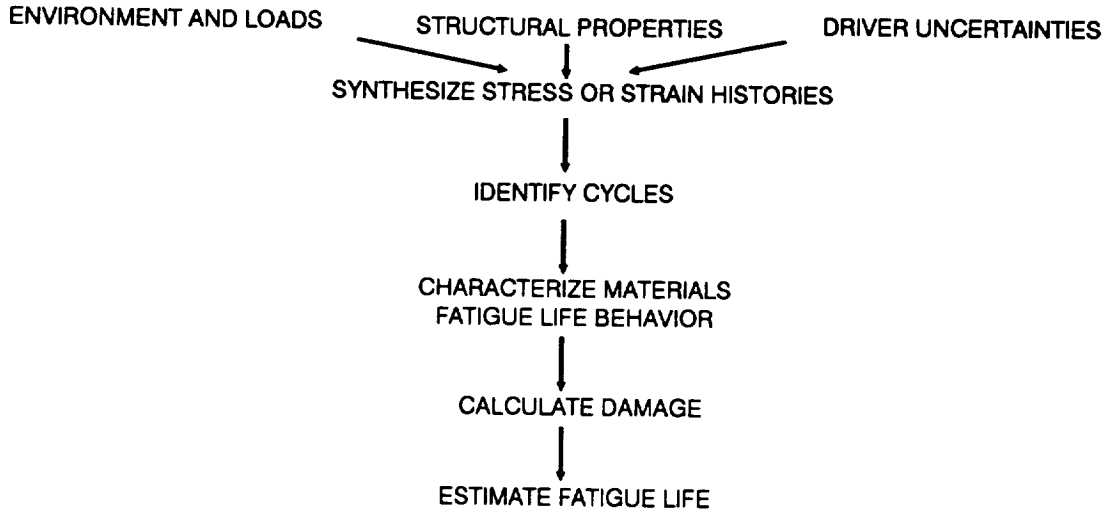

Figure 4.1-1 High Cycle Fatigue Failure Modeling Approach

sequently, a cycle counting procedure, such as that given in Section 2.2.1.4 of [1] is not needed.

The development of the turbine blade HCF model was a collaborative effort between Pratt & Whitney and JPL. The Pratt & Whitney portion of this effort was funded as a part of the Alternate Turbopump Development Program. This collaborative effort to develop the turbine blade HCF model was stopped short of completion due to unavailability of required funding for Pratt & Whitney. The status of the model at the time work was suspended is presented in the following. A major portion of the unfinished work was to develop a nonparametric statistical procedure to be used in characterizing turbine blade vibratory stress. This procedure was to have been used in the vibratory stress model discussed in Section 4.2.3 of the following. Since uncertainty of blade vibratory stress was not represented in the HCF model, no results are presented.

Section 4.2
Turbine Blade HCF Methodology

4.2.1 Component Description

The ATD-HPOTP Turbine Blades are hollow single-crystal castings. The first and third stages each have fifty-four blades. The turbine is driven by high temperature, high pressure steam (H_2O) and gaseous hydrogen (H_2).

HCF analysis of a turbine blade was performed at the location identified in design analysis performed by Pratt & Whitney as having the highest local stress. The stress at this location controls HCF crack initiation life. For both the first and third stage turbine blades, this critical location is on the blade airfoil pressure face near the fillet where the blade airfoil attaches to the platform. The fact that there are fifty-four such locations is taken into account in the failure simulation.

The stresses in the blade which produce high cycle fatigue damage at the critical location are due to time-varying aerodynamic forces. The aerodynamic forces on the blade result from work being extracted from the fluid stream by the blade. The average aerodynamic force on the blades produces the turbine output torque, while the time-varying component of the aerodynamic force causes HCF damage.

4.2.2 Modeling Approach

Figure 4.2-1, shows the life calculation procedure used in the turbine blade HCF model. The major elements of the life calculation procedure are driver selection, driver transformation, zero mean stress transformation, the materials model, and the transformation of the number of cycles to failure N_f to the life L in seconds. In the driver transformation, stress is defined as a function of the drivers. The driver transformation consists of a mean stress model and a vibratory stress model, as described in Section 4.2.3. In the driver transformation algorithm the variation of stress with respect to the drivers over appropriate ranges of driver values is represented. Uncertainties about driver values and modeling accuracy are considered at the step of the life calculation procedure where they are relevant. The fatigue life corresponding to the equivalent stress amplitude is provided by the materials model.

The high cycle fatigue life of the turbine blade material was stochastically characterized using the materials fatigue life model discussed in detail in Section 2.1.2.1 of [1]. The data used in the materials fatigue life model consisted of tests to failure of eight specimens. The test specimens of the blade material were subjected to stress controlled cyclic loading (frequency = 20 Hz) with a stress ratio R of –1.0 in fatigue testing at Pratt

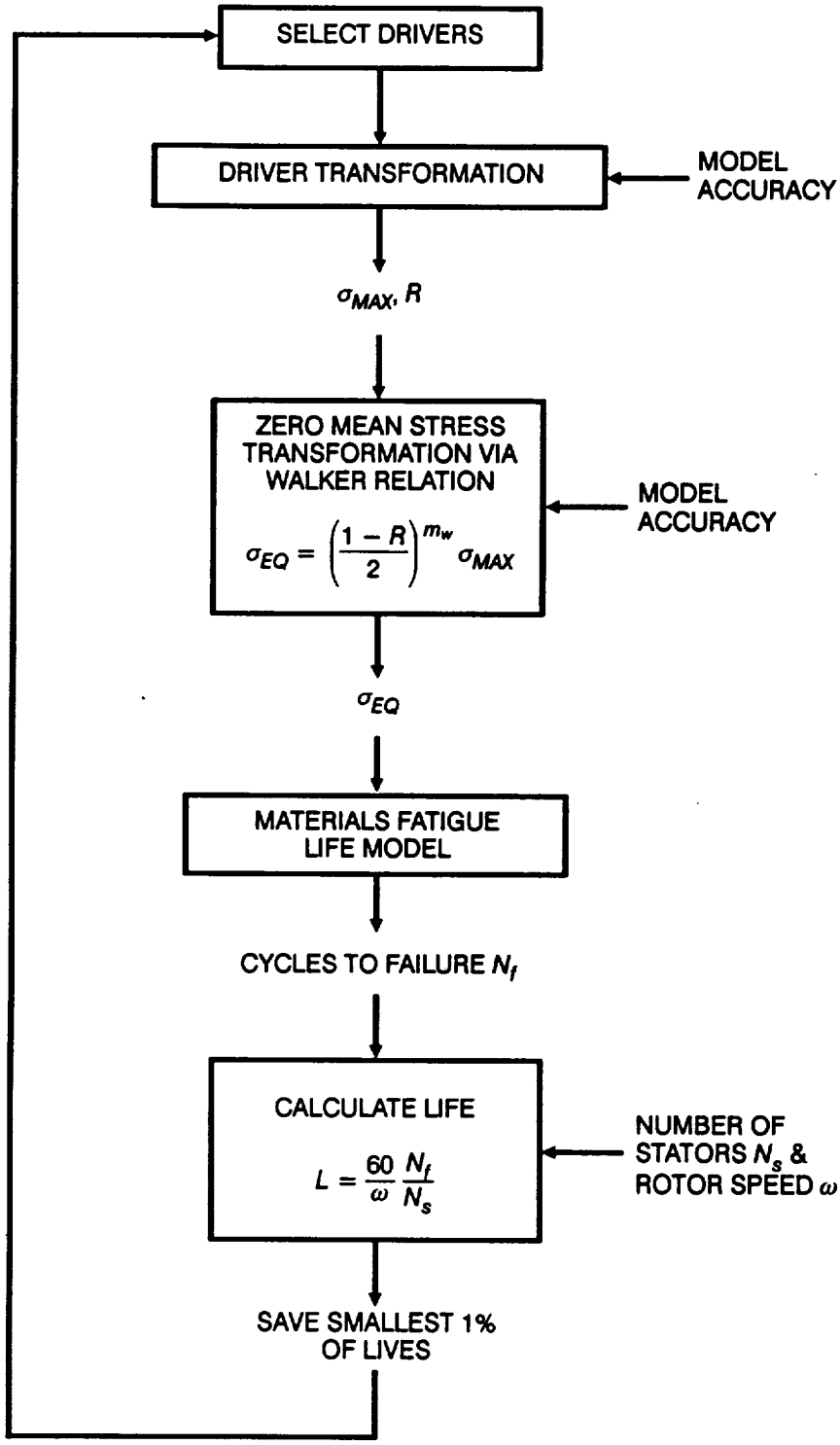

Figure 4.2-1 Calculation Procedure for the Turbine Blade HCF Model

& Whitney. The fatigue tests were performed in 5000 psig hydrogen at room temperature. The test specimens were smooth and in the [001] or radial orientation. Details on the materials characterization model can be found in Section 2.1.2 of [1].

4.2.3 Driver Transformation

The driver transformation step of the calculation procedure of Figure 4.2-1 is shown in detail in Figure 4.2-2. In the driver transformation, the parameters that affect HCF life, i.e., the drivers, are used to compute the blade vibratory stress. The driver transformation procedure mirrors the engineering design analysis performed by Pratt & Whitney. In this approach the time-varying, or vibratory, stress in the turbine blade is expressed as a function of the mean stress at the blade root $\overline{\sigma_{BR}}$ due to the torque produced by the turbine.

As shown in Figure 4.2-2, the parameters $\dot{m}$ and Δh used in the blade root mean stress model are characterized as a function of the turbopump speed ω. These characterizations are based on results of Pratt & Whitney's turbopump performance balance computer code.

From a consideration of the mechanical work that the turbine extracts from the gas stream, it may be shown that the average force on a blade that produces the turbine output torque is

$$\bar{F} \propto \frac{\dot{m}\,\Delta h}{\omega\, R_{avg}\, N_b}$$

Noting that the bending moment at the blade root is $M_r = F(R_{avg} - R_{root})$ and that the stress at the blade root due to bending is $\sigma_r = M_r\, C \,/\, I_{min}$, we see that

$$\overline{\sigma_{BR}} \propto \frac{\dot{m}\,\Delta h\, C}{\omega\, N_b\, I_{min}} \left(1 - \frac{R_{root}}{R_{avg}}\right) \tag{4-1}$$

where

$\dot{m}$	= fluid mass flow rate
Δh	= enthalpy change across a turbine stage
R_{avg}	= average turbine blade radius relative to shaft center
N_b	= number of turbine blades
R_{root}	= turbine blade root radius relative to shaft center
I_{min}	= minimum moment of inertia of turbine blade cross section
C	= distance from turbine blade neutral axis

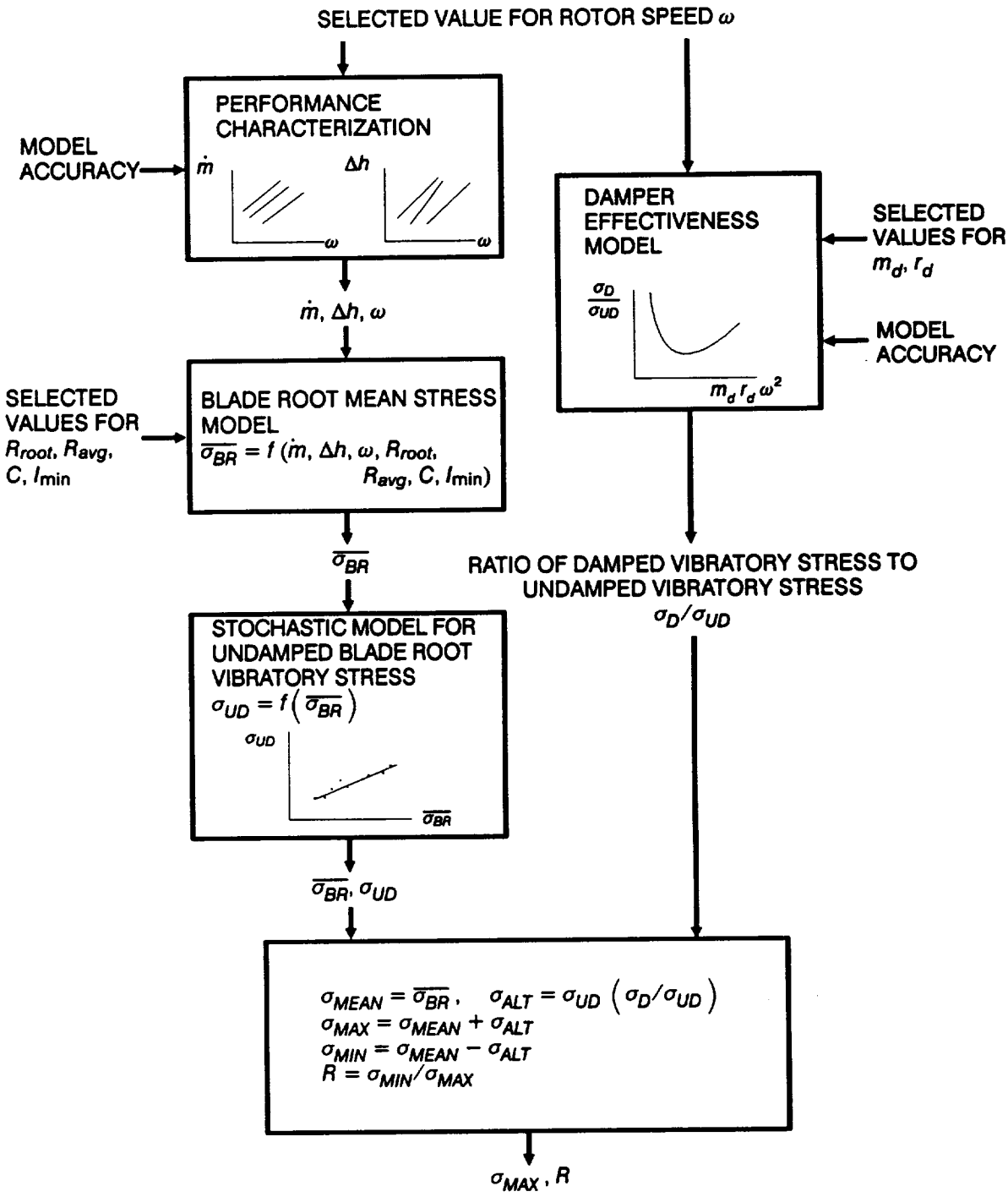

Figure 4.2-2 Structure of the Driver Transformation for the Turbine Blade HCF Model

Equation 4-1 is the basis of the blade root mean stress model shown in Figure 4.2-2.

In the engineering design analysis procedure used by Pratt & Whitney, the alternating stress at the blade root is empirically characterized as a function of $\overline{\sigma_{BR}}$. This empirical characterization has been developed from tests of turbines with instrumented blades. In these tests, measurements of the peak undamped vibratory stress σ_{UD} were taken on several turbines which operate with different values of $\overline{\sigma_{BR}}$ due to their differing designs. In some cases, operating conditions for a specific turbine were changed to produce a change in $\overline{\sigma_{BR}}$.

A correlation between σ_{UD} and $\overline{\sigma_{BR}}$ was established by regression analysis. Had development of the blade HCF model continued, nonparametric statistical methods would have been applied to represent uncertainty in σ_{UD} warranted by the test data. The undamped vibratory stress model shown in Figure 4.2-2 would have incorporated the nonparametric statistical analysis. As an alternative to the use of nonparametric statistical methods, procedures similar to those used in the characterization of materials fatigue life as given in Section 2.1.2 of [1] could be applied. The uncertainty of σ_{UD} would have been treated in the stochastic vibratory stress model.

In the damper effectiveness model shown in Figure 4.2-2, the ratio of damped blade vibratory stress to undamped blade vibratory stress σ_D / σ_{UD} is expressed as a function of the centrifugal force produced by the blade damper. This damping ratio characterization is based on the results of finite element model analysis in which damper stiffness is simulated as a spring and a sinusoidal forcing function is used. Damper effectiveness predictions have been verified by measurements on damped blades.

Damper effectiveness predictions are uncertain due to inaccuracies in modeling the damping phenomenon and because the parameters which govern damper effectiveness are uncertain. Such parameters include coefficient of friction and blade dimensions. When work on the blade HCF model was suspended, nominal damper effectiveness predictions were available, and limited studies of the sensitivities of damper effectiveness to governing parameters had been initiated. These sensitivity studies and other information regarding damper model accuracy would have been the basis for characterizing the accuracy of the damper effectiveness model represented by the factor λ_D.

Time-varying fluid dynamic forces on a blade are assumed to be of constant amplitude with a mean stress equal to the blade root mean stress

$$\sigma_{MEAN} = \overline{\sigma_{BR}} \tag{4-2}$$

and an alternating stress given by the damped vibratory stress

$$\sigma_{ALT} = \sigma_{UD} \left(\frac{\sigma_D}{\sigma_{UD}} \right). \tag{4-3}$$

The maximum and minimum of the cycle are then

$$\sigma_{MAX} = \sigma_{MEAN} + \sigma_{ALT} \tag{4-4}$$

$$\sigma_{MIN} = \sigma_{MEAN} - \sigma_{ALT}. \tag{4-5}$$

Finally, the stress ratio is defined as

$$R = \sigma_{MIN} / \sigma_{MAX}. \tag{4-6}$$

4.2.4 Mean Stress Effects

The blade HCF model incorporates the stress formulation of the stochastic materials fatigue life model, which is based on an equivalent zero-mean stress and which is described in Section 2.1.2.1 of [1]. The stress amplitude from the driver transformation must be adjusted to the equivalent zero-mean stress amplitude to be compatible with this fatigue life model. The equivalent zero-mean stress amplitude given by the Walker relation [2] is

$$\sigma_{EQ} = \left(\frac{1 - R}{2} \right)^{m_w} \sigma_{MAX} \tag{4-7}$$

in which m_w is the characteristic Walker exponent for the material.

4.2.5 Modeling Multiple Critical Locations

The fact that only one blade is modeled by engineering analysis while there are fifty-four identical blades in each of the first and third stages must be considered. The procedure for modeling HCF failure in this case is discussed in Section 2.1.6 of [1] and is used in the turbine blade HCF model.

4.2.6 Probabilistic Failure Model Implementation

The Probabilistic Failure Model (PFM) for turbine blade HCF failure generates a distribution of failure times that results from the probabilistic characterization of drivers. As shown in Figure 4.2-3, the PFM model for the blade consists of the

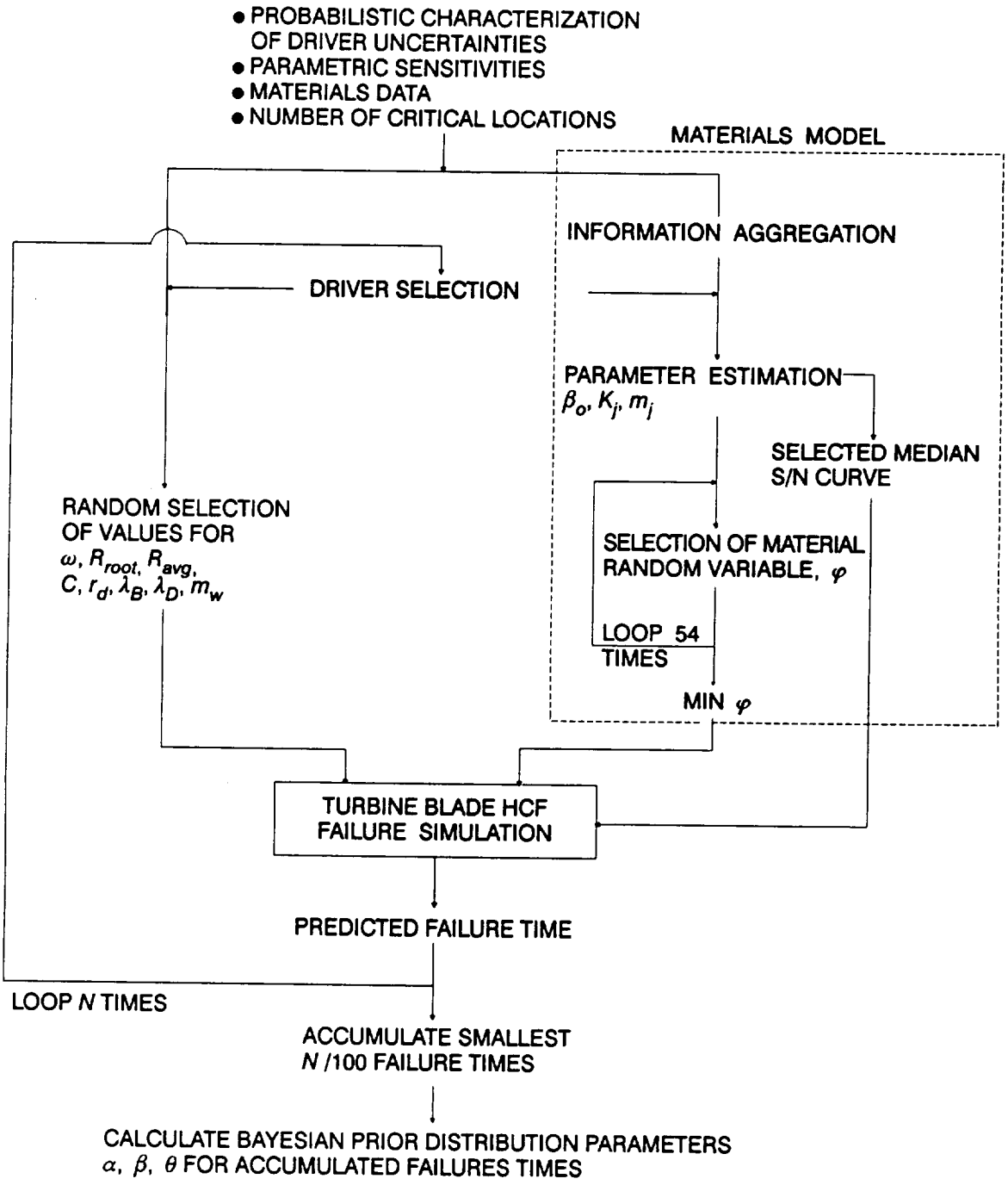

Figure 4.2-3 Structure of the Turbine Blade HCF Probabilistic Failure Model

materials model, the HCF failure simulation, the structure for selection of drivers, and the procedure for characterizing the simulated failures as a Bayesian prior failure distribution for the purpose of allowing the impact of any available blade success/failure data to be included in the characterization of the blade failure distribution. Since the current analysis is for a candidate blade, no test data is available to use Bayesian updating.

In the PFM model shown in Figure 4.2-3, ω, R_{root}, R_{avg}, C, and r_d are characterized by Normal distributions, and λ_B, λ_D, and m_w are characterized by Uniform distributions. The materials model provides a family of stochastic curves relating fatigue life to stress. In the iteration loop, to be executed N times, the materials model parameters are established. Then, values of ω, R_{root}, R_{avg}, C, r_d, λ_B, λ_D, and m_w are drawn from their respective distributions.

Since there are fifty-four blades on the disk, the appropriate realization of the stochastic stress-life curve to use in computing component life for each iteration will be that corresponding to the minimum of fifty-four selections of the materials model parameter, φ. See [1], Section 2.1.6 for further explanation. Since a blade HCF life is calculated for each iteration, a total of N simulated failure times will be calculated. If model development had continued, the blade results would have been obtained using N = 20,000. Since the failure probabilities of interest are of the order .001, only the smallest one percent of failure times needs to be saved and used to calculate the Bayesian Prior Distribution parameters α, β, θ. The procedure for calculating α, β, and θ is discussed in [1], Section 2.1.1.

The HCF failure simulation used in the blade PFM is shown in Figure 4.2-4. The failure simulation is performed in several steps. First, the driver transformation is performed. The driver transformation provides the maximum of the constant amplitude stress cycle σ_{MAX} and the stress ratio R. Next, the Walker relation of Equation 4-7 is used to transform σ_{MAX} and R to an equivalent zero mean stress amplitude σ_{EQ}. The predicted failure time N_f in cycles is then obtained using the randomly selected S/N curve from the materials characterization model. Finally, the life L in seconds is calculated.

The driver transformation used in the blade HCF failure simulation is shown in Figure 4.2-2. The driver transformation is performed in several steps. First, the flow rate $\dot{m}$ and enthalpy change Δh are calculated based on the performance characterization model. Next, the blade root mean stress $\overline{\sigma_{BR}}$ calculation is performed, using Equation 4-1. The undamped blade vibratory stress σ_{UD} is found as a function of $\overline{\sigma_{BR}}$. Then, the damper effectiveness model is used to obtain the ratio of damped vibratory stress to undamped vibratory stress σ_D/σ_{UD}. Finally, the mean

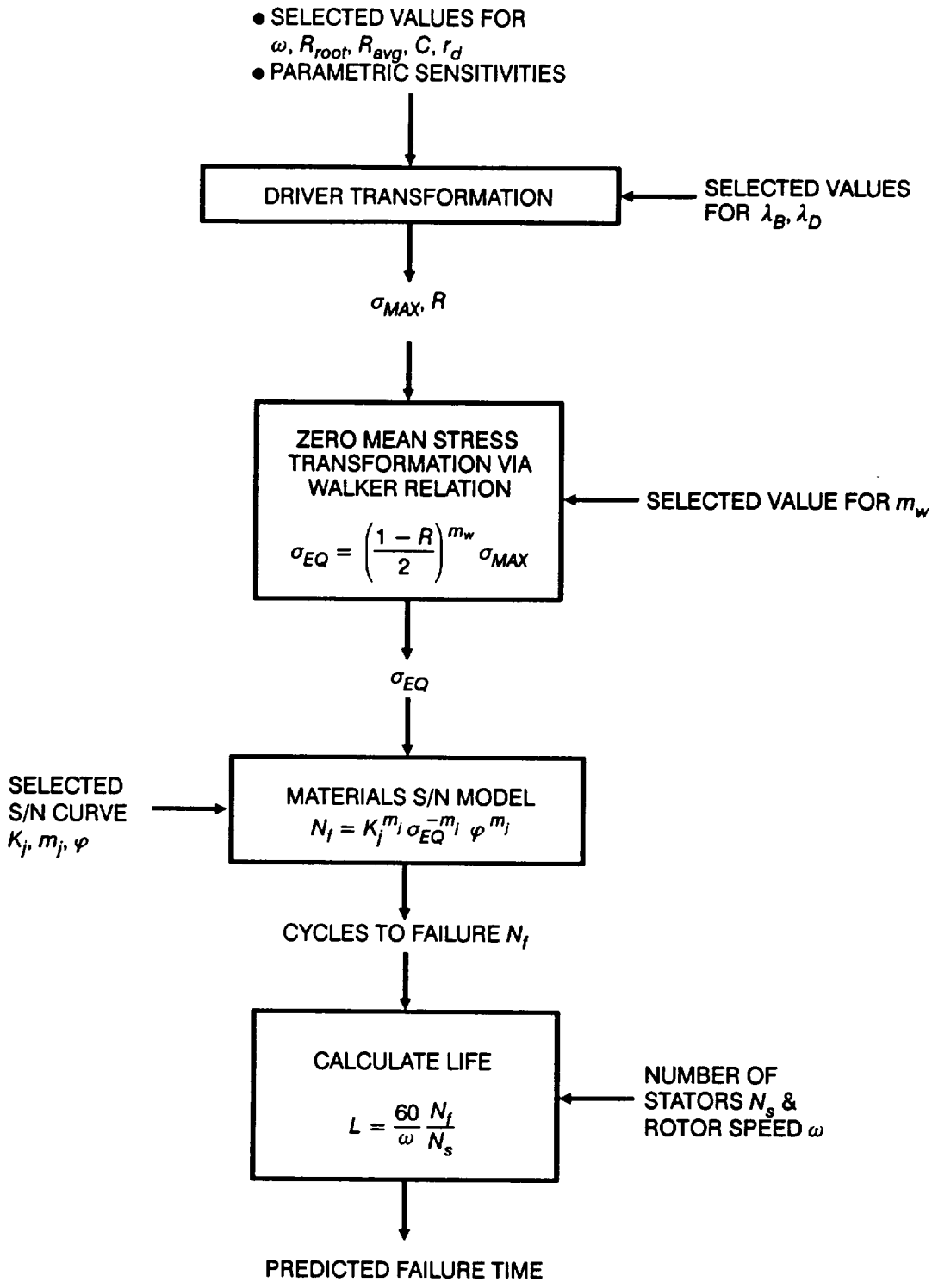

Figure 4.2-4 Turbine Blade HCF Failure Simulation Used in the Probabilistic Failure Model

and alternating stresses are calculated and used to find the maximum and minimum stresses and the stress ratio.

References

[1] Moore, N., et al., An Improved Approach for Flight Readiness Certification – Methodology for Failure Risk Assessment and Application Examples, JPL Publication 92-15, Jet Propulsion Laboratory, California Institute of Technology, Pasadena, California, June 1, 1992.

[2] Doner, M., Bain, K. R., and Adams, J. H., "Evaluation of Methods for the Treatment of Mean Stress Effects on Low-Cycle Fatigue," Journal of Engineering for Power, Vol. 104, April 1982.

Appendix 4.A
List of Symbols

a	Beta distribution range parameter
a	Uniform distribution range parameter
A	statistical assurance that reliability is at least as large as stated
A_j	S/N curve location parameter
b	Beta distribution range parameter
b	Uniform distribution range parameter
$Be(\cdot)$	Beta distribution function
C, C_o	coefficient of variation of fatigue strength
C	distance from turbine blade neutral axis
E	Young's modulus
$F(\cdot)$	cumulative probability distribution function
$\bar{F}$	average force on a blade that produces the turbine outlet torque
I_{min}	minimum moment of inertia of turbine blade cross section
I_o	credibility range for coefficient of variation of fatigue strength
J_o	credibility range for an S/N curve shape parameter
K_j	S/N curve location parameter
L	fatigue life in seconds
$\dot{m}$	fluid mass flow rate
m_d	damper mass
m_j	S/N curve shape parameter
M_r	bending moment at the blade root
m_w	characteristic Walker exponent for a given material
$MED(\cdot)$	median value

n	inner loop simulation trials
N	degrees of freedom parameter
N	outer loop simulation trials
N_b	number of turbine blades
N_f	fatigue life in cycles
N_j	size of the jth materials fatigue test data set
N_s	number of stators
$N^*_{i,\,i+1}$	S/N curve life boundaries
$N(\cdot)$	Normal distribution function
r_d	damper radius
R, R_o	component reliability
R	number of life regions used to represent an S/N curve
R	stress ratio = $\sigma_{MIN} / \sigma_{MAX}$
R_{avg}	average turbine blade radius relative to shaft center
R_{root}	turbine blade root radius relative to shaft center
S	stress
S_x^2, S_y^2	sample variance
S_{xy}	sample covariance
S/N	stress/life
$U(\cdot)$	Uniform distribution function
$VAR(\cdot)$	Variance value
$W(\cdot)$	Weibull distribution function
x	ln (*stress*)
y	ln (*life*)
α	Gamma distribution parameter
β, β_o	Weibull distribution shape parameter
γ	Euler's constant, .577 . . .

Δh	enthalpy change across a turbine stage
ε	materials intrinsic variability
η_o	Weibull distribution scale parameter
θ	Gamma distribution parameter
θ	Beta distribution parameter
λ	accuracy or uncertainty factor; λ_B = turbopump performance balance model accuracy factor; λ_D = damper effectiveness model accuracy factor
λ, λ_o	Weibull distribution parameter
μ	Normal distribution parameter
π	3.14159265 . . .
ρ	Beta distribution parameter
σ	stress; σ_{ALT} = alternating stress; $\overline{\sigma_{BR}}$ = blade root mean stress; σ_D = damped blade vibratory stress; σ_{EQ} = equivalent zero mean stress; σ_{MAX} = maximum stress; σ_{MEAN} = mean stress; σ_{MIN} = minimum stress; σ_r = stress at the blade root due to bending; σ_{UD} = undamped blade root vibratory stress
σ^2	Normal distribution parameter
φ	materials intrinsic variability
$\chi^2(\cdot)$	Chi-square distribution function
ω	rotor speed